Title

Probabilistic Characterization and Response Prediction of Micro-Electro-Mechanical Systems

Authors

Mirfendereski, Dariush
Der Kiureghian, Armen
Ferrari, Mauro
et al.

Publication Date

1996-06-01

Report No.
UCB/SEMM-96/04

STRUCTURAL ENGINEERING, MECHANICS AND MATERIALS

PROBABILISTIC CHARACTERIZATION AND RESPONSE PREDICTION OF MICRO-ELECTRO-MECHANICAL SYSTEMS

Dariush Mirfendereski
Armen Der Kiureghian
Mauro Ferrari
George Johnson

Report to the Sponsor:
The National Science Foundation

June 1996

DEPARTMENT OF CIVIL AND ENVIRONMENTAL ENGINEERING
UNIVERSITY OF CALIFORNIA AT BERKELEY
BERKELEY, CALIFORNIA

PROBABILISTIC CHARACTERIZATION AND RESPONSE PREDICTION OF MICRO -ELECTRO-MECHANICAL SYSTEMS

Dariush Mirfendereski
Armen Der Kiureghian
Department of Civil and Environmental Engineering

Mauro Ferrari
Department of Civil and Environmental Engineering and
Department of Materials Science and Mineral Engineering

George Johnson
Department of Mechanical Engineering

A report on research supported by
the National Science Foundation under
Grant No. ECS-9023714

Report No. UCB/SEMM-96/04
Structural Engineering, Mechanics and Materials
Department of Civil and Environmental Engineering
University of California at Berkeley
Berkeley, CA 94720

June 1996

ABSTRACT

Micro-Electro-Mechanical Systems (MEMS) are micro devices used as sensors and actuators with structural dimensions of the order of a micron. The focus in this dissertation is on MEMS made of planar, polycrystalline silicon and fabricated through integrated circuit-based processes. The process conditions often result in texture in the material that manifests as anisotropy in the mechanical properties. Due to the random orientations and shapes of the crystal grains, the constituent materials also exhibit inhomogeneity at the microscopic level. These material characteristics can have significant influences on the mechanical response of MEMS devices. With the increasing push towards miniaturization in MEMS, the potential for uncertainties in the mechanical response of nominally identical devices has increased. Without knowledge of these uncertainties, the successful implementation of production scale manufacturing is hampered.

Homogenization techniques such as the first order Voigt and Reuss bounds are shown to be sufficiently close for MEMS made of polysilicon (containing large number of crystals within smallest structural dimensions) and their derivation for {100} and {110} textures are outlined. To account for the effects of random crystal shape and orientation, detailed approaches to the probabilistic modelling and analysis of the mechanical response of multicrystalline structural elements and devices are presented using simulation, random fields and stochastic finite element techniques. A mathematical model—the Voronoi Tesselation—is used to simulate random multicrystalline geometries which are then analyzed using finite elements. A more efficient continuous-parameter random field characterization of the crystalline micro-structure is also employed. Equivalent random field properties are defined and used in conjunction with stochastic finite element methods to probabilistically compute the response of MEMS components and devices. These analysis techniques enable a quantitative estimation of response uncertainties for multicrystalline structural elements and devices.

Typical results show coefficients of variation (C.O.V.) of approximately 3% in the response of micro beams with grain sizes of the same order as their depths. For a folded beam lateral micro resonator, the natural frequency is found to have C.O.V.s that are lower than the C.O.V.s of the lateral stiffness of the constituent beams. The uncertainty in the natural frequency, however, is dependent on the length of the consituent beams and can reach as high as 6% for beams greater than 40 μm in length.

This dissertation represnts a first attempt to analytically and numerically characterize the uncertainty inherent in the properties and response of MEMS that arises from the natural randomness in the contituent materials.

ACKNOWLEDGMENT

The work reported herein was supported by Grant No. ECS-9023714 of the National Science Foundation, which is gratefully acknowledged. The authors express special thanks to Professor Jerome Sackman, who was a key participant in formulating the initial ideas of the project.

TABLE OF CONTENTS

Chapter 1

INTRODUCTION & SUMMARY

1.1 MOTIVATION

This report investigates the inherent uncertainties in the mechanical response of Micro-Electro-Mechanical Systems (MEMS). These uncertainties generally arise as a result of the combined effects of the material microstructure and the small length scales associated with MEMS structural components. The material microstructural characteristics, e.g sizes, shapes, orientations, or arrangements of crystal grains in polycrystals, are generally uncertain. For length scales of the same order of magnitude as the microstructural variations, these uncertainties are reflected in the mechanical responses of MEMS devices. As MEMS technology pushes the frontiers of miniaturization, these microstructural effects on the performance of devices become increasingly important. Thus knowledge about and control of these effects become essential to the successful design and development of the next generation of MEMS devices.

The field of MEMS encompasses devices—generally sensors or actuators—that are fabricated on a micro scale, with structural dimensions as small as a micron [1.4, 1.5]. Having first been developed as an offshoot of the integrated circuit (IC) fabrication technology, MEMS devices are primarily made out of silicon. Other materials, however, are increasingly being employed. The field of MEMS has grown exponentially in recent years, with applications in areas as diverse as the automotive industry, the aerospace industry, and signal processing. Biomedical applications and devices such as biofiltration [1.9] and oncological microdevices [1.10], respectively have already been established. New areas of application are being added at an increasing pace. Following the developments of the IC and the microprocessor, MEMS promises to be the next technological milestone in electronics.

Successful design of MEMS requires a knowledge about their mechanical response in addition to their electrical performance. Just as this new field has spurred basic studies of the physics and chemistry of materials and structures in the micro-scale, it has also resulted in efforts to achieve an improved understanding and control of the mechanical behavior of materials and structural components at these scales [1.3, 1.7].

The majority of studies on the mechanical response of MEMS have been experimental. Most of these have relied on basic linear elastic structural theories and strength of materials principles to relate responses to excitations. More recent studies have employed improved structural theories and finite element methods to better capture the behavior of MEMS structures and components [1.2, 1.8]. Various phenomena such as geometric non-linearities, irregular boundary conditions, and residual stresses have been modeled. Most of these studies, however, assume that the materials are isotropic, and they all implicitly assume material homogeneity.

Contrary to many elasticity problems encountered by structural engineers, homogeneity and isotropy may not be valid assumptions for the materials of MEMS structures. A homogeneity assumption for structural materials such as steel holds true so long as the geometric dimensions of a structrural component under consideration are large in comparison with the dimensions of a single crystal (e.g. there are millions of crystals grains in one cubic inch of steel). Isotropy only holds true if there are no preferred crystal or other microstructural orientations. The polycrystalline structure of many of the materials employed in the manufacture of MEMS, e.g. polycrystalline silicon, and the associated fabrication processes often result in materials that neither posses isotropy nor homogeneity at the length scales associated with these microscopic devices. These microstructural effects preclude direct application of classical theories for structural elements, thus necessitating the development of novel analytical and numerical techniques for modelling the material behavior and evaluating the structural responses of MEMS. Furthermore, the variability inherent in the microstructure may require a probabilistic description of the material behavior and structural response evaluation aimed at assessing the performance reliability of MEMS, even if the applied excitations are deterministic.

This study addresses the above needs using a combined deterministic-probabilistic approach based on the principles of engineering mechanics and employing both analytical and numerical techniques. The solution strategy is based on a detailed stochastic idealization of material microstructure and its incorporation in suitable structural component and device models. Real-world applications of the models are proposed which can readily be incorporated into existing analysis and design tools used by MEMS researchers and developers. Sensitivity of response uncertainties to various design parameters are easily computed, allowing the models to be used as tools for achieving improved designs.

1.2 SCOPE

The design, analysis, and manufacture of MEMS involves a very broad multi-disciplinary field encompassing the areas of electrical, mechanical, structural, chemical, and biomedical engineering, amongst others. That which can be termed a "MEMS" device is very loosely defined, since several distinct manufacturing techniques are used to produce a variety of different classes of devices made from numerous different materials. This study does not claim to be applicable to all areas of MEMS, and focuses instead on an important body of MEMS, one that has evolved based on the advances in the integrated circuit (IC) fabrication technology. This branch of MEMS represents the leading-edge of MEMS development and future promise, producing the majority of commercial devices in use today. The experimental expertise in this area at the Berkeley Sensor and Actuator Center (BSAC) made this the natural area of focus for this study.

Areas requiring further theoretical research in the field have been identified as (i) homogenization, (ii) incorporation of microstructural uncertainties in material models, (iii) development of structural elements for analysis of multi-component MEMS, and (iv) residual stresses. In this study, research is concentrated on the following three areas: material modelling, principally microstructural uncertainties related to texture; geometric uncertainties (limited to beam width variation); and development of appropriate stochastic finite element models for the analysis of MEMS structural components and devices. This research is confined to the linear elastic range of response, and excludes residual stress effects and local phenomena. The study represents a first attempt at incorporating the material and geometric uncertainties of MEMS in the assessment of their behavior and response.

Models developed here are applicable to a variety of structural components when incorporated in finite element analyses. Specific structural elements developed are the probabilistic beam element and the uncertain beam super-element. The examples considered are planar structures made of polysilicon using deposition processes.

1.3 SUMMARY

The report is divided into three parts. Part I describes the motivation for and the scope of the subject, outlines the contents of the report (Chapter 1), and introduces the field of MEMS (Chapter 2). It then reviews current research in the field, evaluating the merits and limitations of existing approaches, and points to possible modelling developments and innovations (Chapter 3). Readers familiar with the field of MEMS may wish to proceed directly to Chapter 3. Part II (Chapters 4–6) focuses on material microstructural modelling appropriate to MEMS, while Part III (Chapters 7 & 8) applies these models to MEMS structural components and complete devices and concludes the study.

1.3.1 Introduction and Background

The review of MEMS in Chapter 2 focuses on integrated circuit (IC) process-based MEMS, or more specifically: integrated, microfabricated, surface-micromachined, thin-film based, sub-millimeter sized MEMS. Figure 1.1 shows the

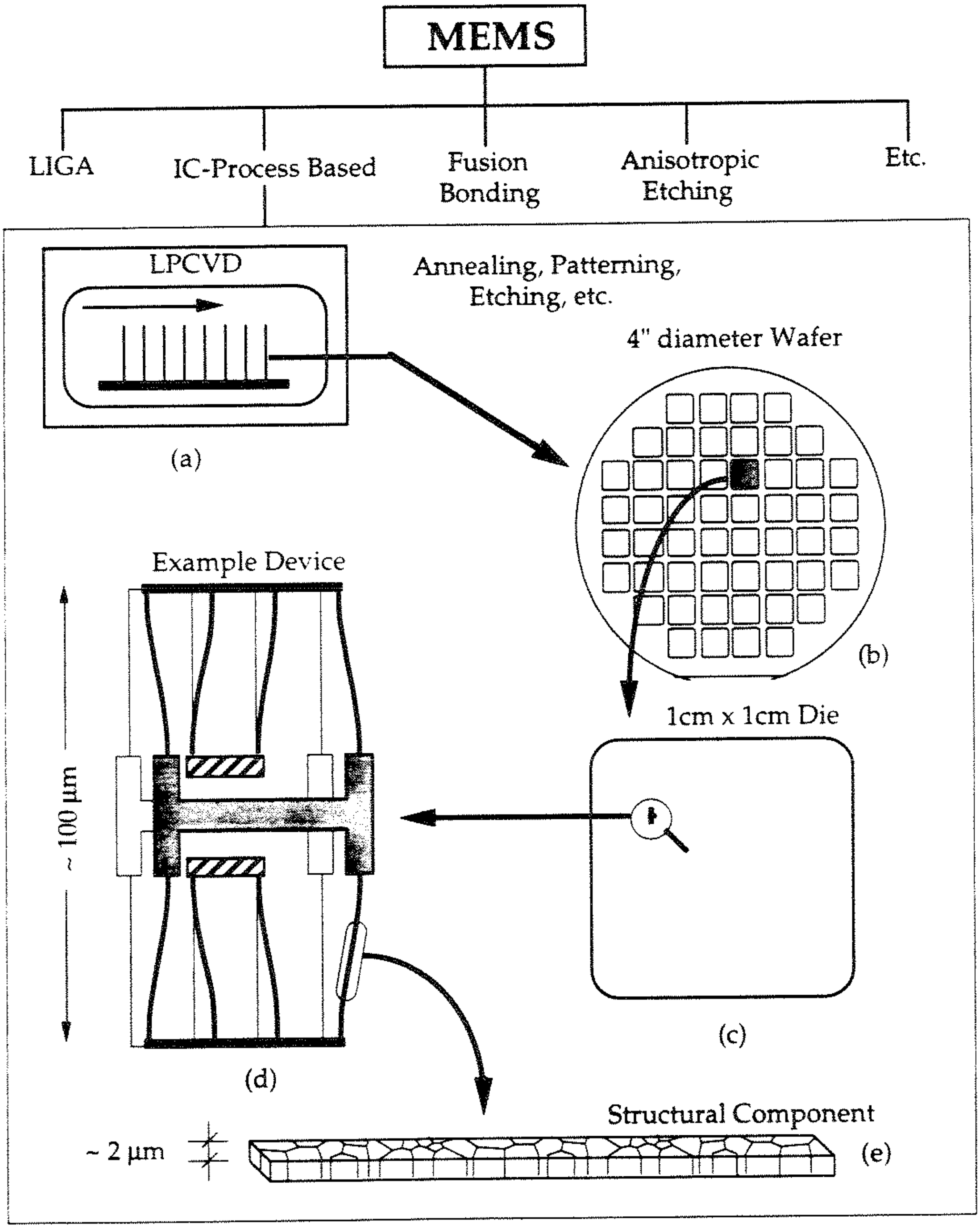

Fig. 1.1 Categorization of MEMS According to Process Type: Focus on IC-Process Based MEMS—Note Range of Dimensions

main categories of MEMS and expands on IC process-based MEMS which is one of the most advanced categories.

The IC-based process involves the deposition of thin films of materials using deposition processes, e.g. low pressure chemical vapor deposition (LPCVD) (Fig. 1.1(a)), combined with patterning, etching, and releasing (surface micromachining) in order to produce the desired "structures" and devices. Typically, as in IC manufacturing, silicon wafers are used as a substrate on which the films are deposited (Fig. 1.1(b)). The wafers are also patterned in a series of 1 cm square dies (Fig. 1.1(c)). Hundreds of MEMS devices can be fitted onto one die.

A portion of an example device—a folded-beam lateral micro-resonator (FBLMR)—with typical overall dimensions is shown in Fig 1.1(d). The eight supporting "beams" in this device act as the resonator's "springs," therefore knowledge regarding the force-deformation behavior of the beams is required in order to predict the behavior of the device. A portion of the beam is shown schematically in Fig. 1.1(e) in which the polycrystalline microstructure is clearly visible. The material is typically polycrystalline silicon and the size of the crystal grains is related to the process conditions (anneal time, temperature, dopant concentration, etc.). The polycrystalline material is typically textured, i.e. with a preferred orientation of the constituent grains. This texture is typically oriented out of plane, resulting in transvesely isotropic properties within the plane.

The determination of the force-deformation relationships of MEMS structural components such as beams therefore involves the development of appropriate models for the constituent materials. The main focus and contribution of this study is the development of special probabilistic material response models appropriate for polycrystalline MEMS structural components and devices. The structural analysis is, for the main part, based on existing highly developed techniques used in various structural engineering and engineering mechanics applications.

After a thorough study of the elastic response of polycrystalline materials, a broad overview of the different possible modelling approaches is presented in Chapter 3. These approaches are reviewed and evaluated in the context of applicability to the MEMS mechanical response prediction.

The elastic response of polycrystalline silicon is closely dependent on that of single-crystal silicon since the polycrystalline state is an aggregate of individual crystal grains. Single-crystal silicon exhibits anisotropic elastic properties due to its diamond cubic crystal structure (Fig. 1.2(a)). The material stiffness matrix, **C**, in a global reference frame is therefore a function of the orientation of the crystal with respect to that fixed frame. This concept is illustrated schematically in Figs. 1.2 (d) and (e), where a pure tensile test on a sample of single-crystal silicon results in a response from which the value for the Young's modulus in the direction of the applied forces can be deduced. The plot shows this variation as a function of the in-plane orientation angle, ψ, for {100} and {110} textures (see §3.2.2 and §4.3).

For a MEMS structural component made up of a relatively small number of crystal grains (e.g. as shown in Fig. 1.1(e)), the problem may be neither isotropic nor homogeneous. Each crystal grain is distinguished from its neighbors by its distinct orientation angle. The shapes and crystallographic orientations of these constituent crystal grains are, in general, random. This results in a random variation of elastic properties within the structural member: $\mathbf{C}(\mathbf{x})$.

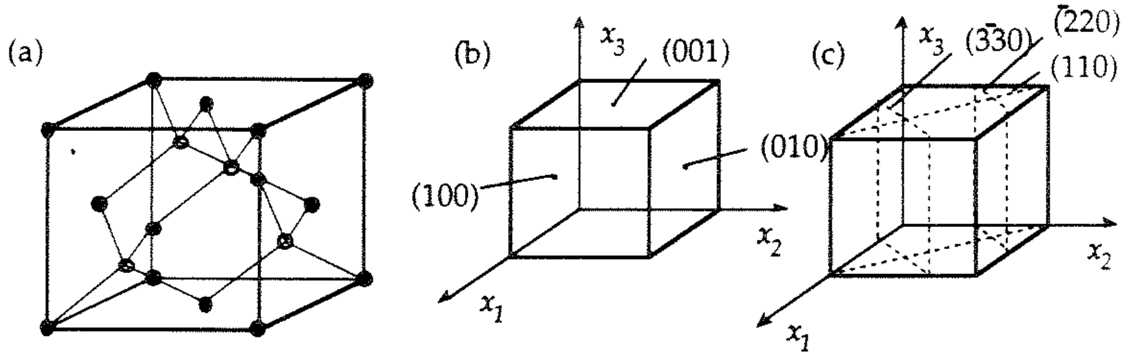

Diamond Cubic
Structure of Silicon
Crystals

Miller Indices of Lattice Planes

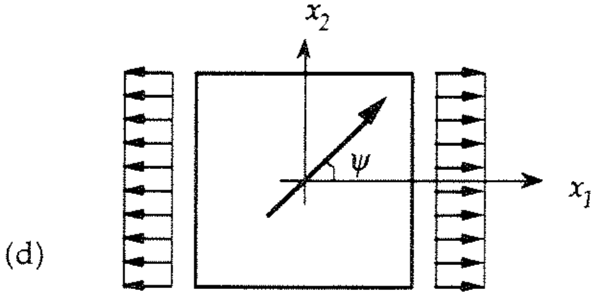

Single-Crystal with
Orientation, ψ, in Uniform Tensio

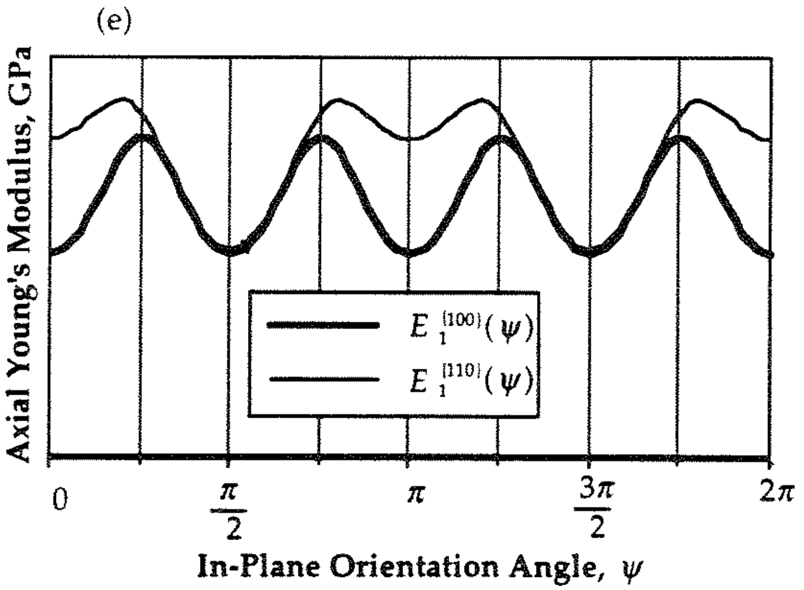

Fig. 1.2 Structure of Single Crystal Silicon and the Variation of Young's Modulus, E_1, with Orientation Angle for {100} and {110} Textures

The uncertain spatial variation of elastic properties translates into an uncertain response of the structural component. The degree of uncertainty in the response depends on a number of factors, including the sensitivity of that response to the microstructural variations. The chief factors, however, are the relative grain size and the degree of anisotropy of the material.

The level of uncertainty in the response of a structural material diminishes with decreasing anisotropy of the material (lower values of α), and with a decreasing grain size relative to the global (structural) dimensions. This concept is illustrated in Fig. 1.3, where the probability density function (PDF) of the response, R, of a structural component, in this case the lateral stiffness of a beam, is shown for different grain sizes, and for materials of varying anisotropy. The schematic beam microstructures represent columnar grains commonly found in phosphorous doped, annealed thin film polycrystalline silicon. The width of the beams are each given by w, while the parameter λ defines the number of crystal grains per unit area of the beam surface.

A clear distinction exists between the isotropic case ($\alpha = 1$) and anisotropic cases ($\alpha \neq 1$). There is also a distinction between homogeneous samples ($w^2\lambda \rightarrow \infty$) and inhomogeneous samples ($w^2\lambda$ finite). For samples with relatively large grain sizes (i.e. $w^2\lambda < 3$), the response is random with a finite standard deviation about the mean. The level of uncertainty increases with increased anisotropy for a given grain geometry.

For isotropic cases, "grain size" is a misnomer for anisotropic grains since grains are only defineable when they can be distinguished from one another based on their orientation differences. All responses are deterministic for

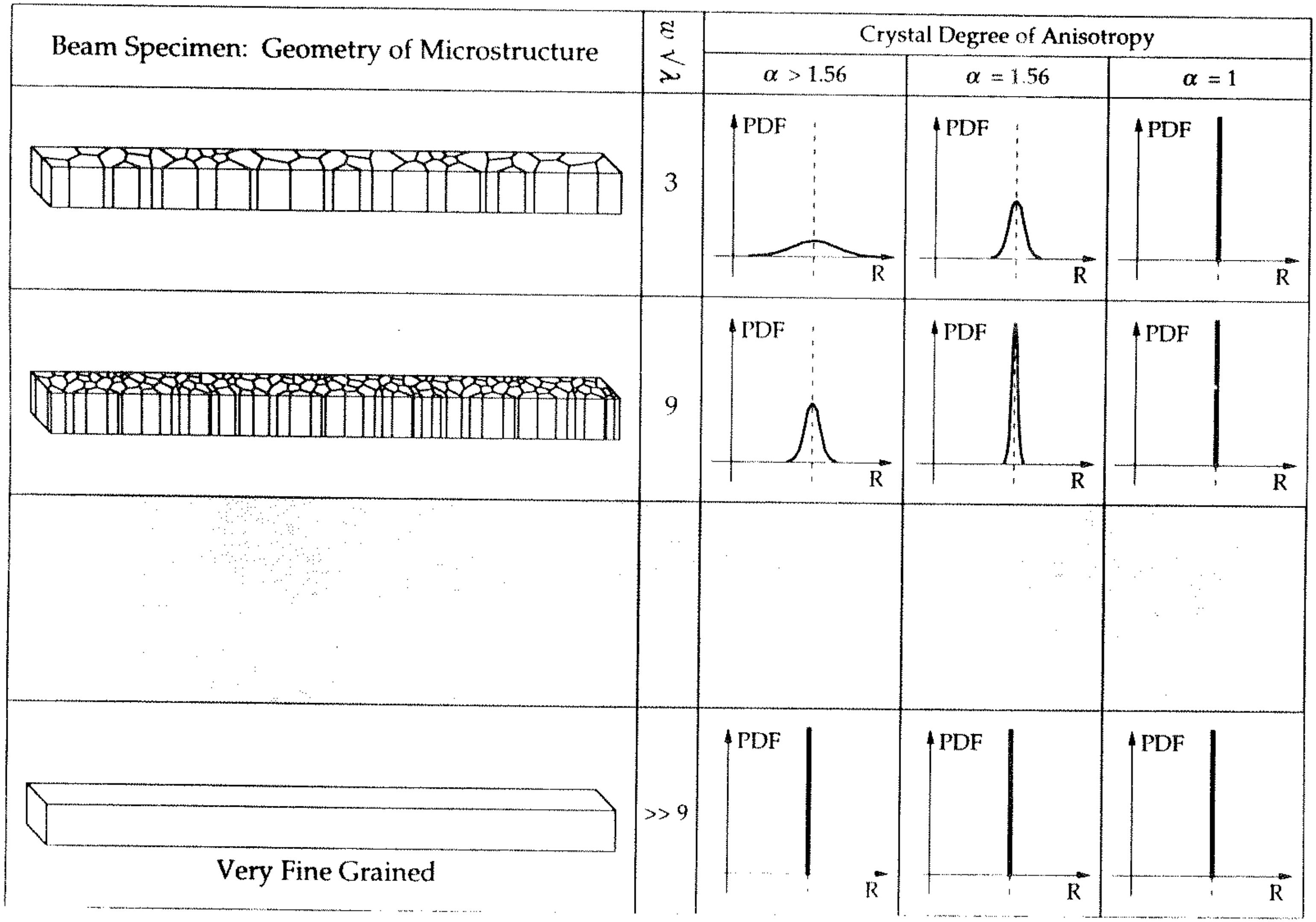

Fig. 1.3 PDF of Global Response, *R*, for Beams with Different Grain Sizes and with Constituent Materials with Varying Degrees of Anisotropy

consistently processed materials and therefore a deterministic isotropic elastic model suffices.

Cases in which the response of interest shows a significant spread require probabilistic approaches to the response estimation. These approaches necessitate models that characterize the uncertainties associated with the material microstructure in relation to the structural dimensions and thatpredict statistical measures of response, e.g. mean, standard deviation, or more generally, the PDF of response.

The remainder of Chapter 3 outlines current approaches to modelling MEMS materials and structures, and points out improved approaches. Reviewing previous work in the field of mechanical modelling of MEMS response indicates that the area of material modelling has received little or no attention. Material homogeneity is universally assumed, while a few studies have recently looked at issues concerning texture and the resultant anisotropy of the material.

1.3.2 Model Development

Part II (Chapters 4–6) concentrates on three specific modelling approaches that address the shortcomings in this field. In Chapter 4, the method of homogenization is reviewed, the limits within which this approach is applicable are delineated, and specific methods applicable in the area of MEMS are explored. Chapter 5 introduces a probabilistic approach using Monte Carlo simulation of random crystal arrangements. Chapter 6 improves upon the simulation model by approximating the mechanical properties of the crystalline arrangements using random fields and employing structural reliability concepts in deriving probabilistic estimates of structural response.

Due to the columnar grains and out of plane texure of many MEMS, fine-grained structural components tend to posess transverse isotropy in their mechanical properties. The in-plane properties can easily be deduced both theoretically and experimentally. Out of plane properties, however, are generally anisotropic and are more difficult to assess experimentally. For a rigorous way of finding or predicting these properties, an analytic/theoretical technique for establishing elastic properties is required. For polycrystalline structures in which the response of interest can be approximated adequately as a deterministic phenomenon, the methods of material homogenization can be employed in modelling the material behavior.

The methodology for homogenization is based on a statistical averaging of material properties that takes into account varying levels of detail of the microstructure. All homogenization models are based on variational principles which establish bounds on the property of interest. "Exact" homogenized properties are only obtained with complete statistical information on the material microstructure.

Employing first-moment information, such as the volume fraction of grains of different orientations (commonly refered to as the orientation distribution function, or ODF), the resulting bounds on the elastic properties are referred to as the Voigt and Reuss bounds. These bounds are generally too wide for many materials, however, for silicon (with the degree of anisotropy, $\alpha = 1.56$) these bounds are deemed adequate for homogenizing the material properties.

As shown in Fig. 1.3, certain problems require a probabilistic approach. The statistical characteristics of the excitation-response relationship can be established by deriving responses for an ensemble of observed or simulated

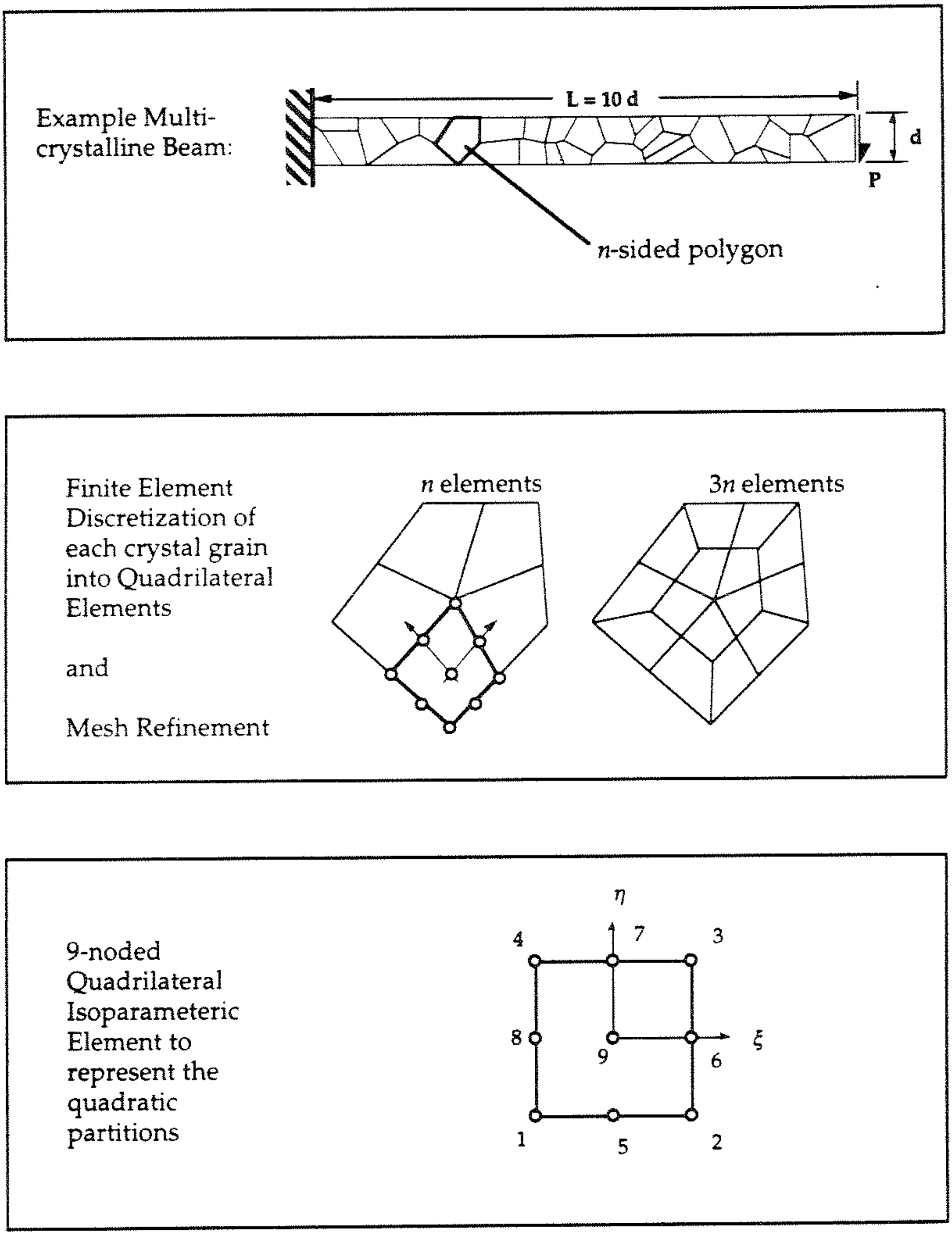

Fig. 1.4 Simulation Model—Finite Elements for Matching Crystal Geometries

sample structures. The response variation, e.g. measured by the C.O.V., is directly related to the inherent material uncertainties. The simulation model presented in Chapter 5 establishes a relationship between the significant microstructural characteristics and the response uncertainty of a structure or device.

The proposed simulation model uses random crystal shapes and sizes that are based on the Voronoï diagram—a mathematically derived geometric construct [1.1, 1.6]. The methodology for the analysis, however, is such that observed random crystal shapes and arrangements can be substituted for the Voronoï polygons. The multicrystalline structure is shown in Fig. 1.4 with the idealized convex polygons representing the individual crystal grains, each with a distinct crystallographic orientation. The beam is therefore inhomogeneous and each crystal grain needs to be discretized separately and assigned different material properties associated with its particular orientation angle ψ. For finite element analysis, a simple and consistent discretization scheme is developed and is shown in Fig. 1.4 with a mesh refinement step. Any convex n-sided polygon is thus discretized into n or $3n$ quadrilateral elements. 9-noded isoparametric quadrilateral elements are used for the finite-element modelling of beam flexural behavior.

By simulating random multicrystalline structures and assigning orientations based on the specified material ODF, each structure can be modelled and analyzed to evaluate the desired response. By simulating a sufficiently large number of stuctures, an artificial sample of responses is generated from which the desired statistics are computed.

One significant drawback of the simulation method is its inefficiency. For example, hundereds of simulations may be required for even the simplest

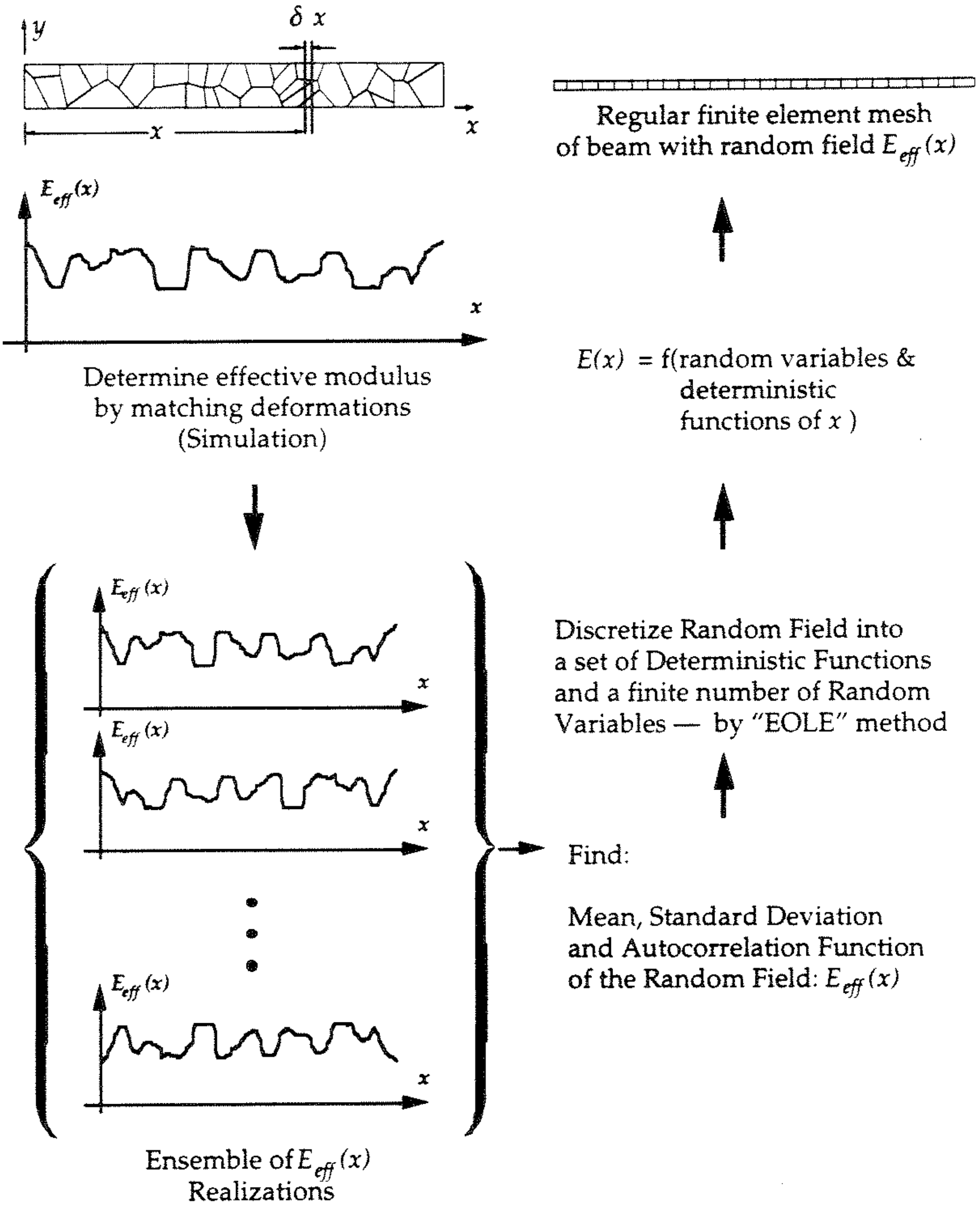

Regular finite element mesh of beam with random field $E_{eff}(x)$

$E(x)$ = f(random variables & deterministic functions of x)

Determine effective modulus by matching deformations (Simulation)

Discretize Random Field into a set of Deterministic Functions and a finite number of Random Variables — by "EOLE" method

Find:

Mean, Standard Deviation and Autocorrelation Function of the Random Field: $E_{eff}(x)$

Ensemble of $E_{eff}(x)$ Realizations

Fig. 1.5 Random Field Model

example structures. The same structure with a slightly different set of force or displacement boundary conditions would require a new set of simulations in order to find the response statistics. In Chapter 6, a random field model is developed (based on the simulation model) that overcomes these problems. A summary of the procedure is shown in Fig. 1.5.

The random field approach incorporates randomness (using random variables) in one equation and also includes the length-scale effects (through the autocorrelation function and correlation length) for fixed $w^2\lambda$. For any displacement or force boundary condition or for any beam length, the same random field model can be re-used with a regular finite element mesh to obtain the response statistics, e.g. mean and standard deviation.

The "smoothed" random field cannot adequately describe certain localized phenomena that are directly associated with the detailed microstructure, e.g. maximum stresses. However, global effects are of most interest, e.g. lateral stiffness of beams, and for those purposes the random field model is shown to be accurate.

The beam random field model can be generalized to other structural members. The significant material parameter for beams is the effective Young's modulus. Additional parameters are needed for other structural members, e.g. Poisson's ratio, v, or shear modulus, G, for plane strain behavior. Due to the presence of anisotropies, however, additional material parameters may be necessary to capture the behavior of structural elements such as plates or shells. The proposed solution to such problems would be a general model describing the material stiffness matrix **C** as a function of the location, i.e. $\mathbf{C}(\mathbf{x})$. This is acheived through a random field modelling of $\mathbf{C}(\mathbf{x})$. The finite-element method can then be employed to model the particular structural member—plate elements, solid elements, etc.—and for each element type, the desired material parameters can be derived from the random field model of **C**(**x**). This approach enables a regular finite element mesh to be used (with the necessary fineness to model the correlations related to crystal sizes), as was the case for the beam problem, with a discretized random field representing the material property variations, **C**(**x**).

1.3.3 Applications

The third and final part of the report is devoted to the application of the models developed in Part II to MEMS structural components and complete devices (Chapter 7) and a concluding Chapter, including recomendations for further developments (Chapter 8).

The importance of employing appropriate models for the analysis of MEMS structural members is established through the application of deterministic and probabilistic models to an example problem. Rules are developed for determining whether a given problem requires probabilistic analysis. Applications of probabilistic models to MEMS devices (folded-beam lateral micro resonator and in-situ micro strain gauge) are shown to be practicable. The analysis points to parameters that govern the level of uncertainty in device responses. Control of device response uncertainties can therefore be achieved through appropriate adjustments in these parameters when the underlying cause of the uncertainty—large grain size and texture—cannot be further reduced. The analysis tools developed allow alternative designs to be studied in order to reduce uncertainties in device responses. This procedure would allow numerous design "tests" at a fraction of the cost of actual fabrication of each design idea.

Many of the ideas developed in this dissertation have clear extensions which would enable their application to additional classes of MEMS structures. Microstructural characteristics such as defects, residual stresses, and stress concentrations may be captured using extensions of the existing models. Additionally, some of the modelling ideas developed in Chapter 3 can be used as the basis for new classes of models that may prove useful in areas other than mechanical response prediction. The future extensions of this research are discussed at the end of Chapter 8 and, together with section §3.4, should prove a useful resource for further research in this field.

CHAPTER 1 REFERENCES

[1.1] Aurenhammer, F., "Voronoï Diagrams—A Survey of a Fundamental Geometric Data Structure," *ACM Computing Surveys*, Vol. 23, No. 3, pp. 345-405, 1991.

[1.2] Brennen, R. A., M. G. Lim, A. P. Pisano, and A. T. Chou, "Large Displacement Linear Actuator," *ASME Winter Annual Meeting*, New Orleans, LA, November 1993.

[1.3] Howe, R. T., R. S. Muller, K.J. Gabriel, and W.S.N. Trimmer, "Silicon Micromechanics: Sensors and Actuators on a Chip," *IEEE Spectrum*, pp. 29–35, July 1983.

[1.4] Muller, Richard S., "Microdynamics," *Sensors and Actuators*, A21-A23, pp. 1-8, 1990.

[1.5] O'Connor, L., "MEMS: Microelectromechanical Systems," *Mechanical Engineer*, February, 1992.

[1.6] Okabe, A., B. Boots, and K. Sugihara, *Spatial Tessellations—Concepts and Applications of Voronoï Diagrams*, John Wiley & Sons, Chichester, England, 1992.

[1.7] Petersen, Kurt (1982). "Silicon as a Mechanical Material," *Proceedings of the IEEE*, Vol. 70, No. 5, pp. 420-457.

[1.8] Pratt, R. I., G. C. Johnson, R. T. Howe, and J. C. Chang, "Micromechanical Structures for Thin Film Characterization," *IEEE Transducers '91*, pp. 205–208.

[1.9] Ferrari, M., W. Chu, T. Desai, D. Hansford, G. Mazzoni, T. Huen, and M. Zhang (1995). "Silicon Nanotechnology for Biofiltration and Immunoisolated Cell Xenografts," *MRS '95*.

[1.10] Ferrari, M. (1994). OncoMEMS patent application.

Chapter 2

MEMS—A REVIEW

2.1 INTRODUCTION

Micro-Electro-Mechanical Systems (MEMS) [2.15] combine electronic and mechanical components to make miniature devices such as sensors which deploy automobile air bags in collisions, or monitor blood pressure inside the human heart during operations, as well as valves and actuators, all with structural dimensions as small as a micron (μm). Based on processing techniques borrowed from the semiconductor industry, these tiny devices are inexpensively mass-produced, adding the benefit of low cost to their size and weight advantages over conventional devices. In biomedical applications (BioMEMS), the nanofilter and biocapsule have seen successfully implementation [2.26], while the newly developing area of Oncological microdevices (OncoMEMS™) [2.27], intended for cancer therapeutics and diagnostics, shows tremendous promise. Additionally, microdevices promise new capabilities by taking advantage of the scaled physical laws in the micro domain. Following the developments of the transistor, the integrated circuit (IC), and the microprocessor, the development of MEMS promises to be the next major milestone in electronics.

This chapter presents a review of MEMS intended for readers unfamiliar with the field. It aims to establish the knowledge-base necessary for an understanding and appreciation of the modeling and analyses presented in later chapters for predicting MEMS' mechanical response. The vast breadth and multidisciplinary nature of this field naturally limit the depth of coverage possible in this introductory chapter. The approaches taken in later Chapters (4–6) mainly concentrate on planar polycrystalline silicon structures, an important body of MEMS with a plethora of applications and inherent advantages over other classes of MEMS that are invaluable for future developments in this field. Accordingly, the focus of this chapter also takes such a slant. Nevertheless, other important areas of MEMS are briefly covered for completeness. Readers interested in a more detailed coverage are guided to pursue the subject through the selective list of references provided at the end of the chapter.

The development of MEMS is an extension of the trend towards miniaturization that has accelerated over the last two to three decades. To begin with, some background to the developments of this trend is presented. Next, it is shown how, through the use and adaptation of IC fabrication techniques, this trend has led to the development of what we know today as MEMS. A description of MEMS, the requirements which have led to their development, the reasons they have achieved such prominence, and an overview of some future trends are then presented. A representative set of typical MEMS components and devices are then introduced with a description of how they function. This is followed by a description of the materials and fabrication techniques employed in the manufacture of MEMS. These have an important bearing on the material modeling assumptions necessary for an accurate prediction of MEMS' mechanical response. The chapter concludes with a summary of the main points.

2.2 EVOLUTION OF MEMS

2.2.1 Background

Miniaturization has brought high performance coupled with low cost in many fields. Taking microprocessors as an example, higher processing speeds have been achieved through the reduced distances that signals travel in ICs, while reduced costs are attained through the incorporation of larger numbers of elements onto one chip. It seems that every year, advances are pushing the boundaries of miniaturization lower and lower. How far can this trend go? What, if any, are the boundaries?

As early as 1959, Richard P. Feynman, the Nobel Prize winning physicist, discussed the concepts of manipulating and controlling things on a small scale [2.2]. By relying on physical laws and principles, he defined the boundaries of miniaturization through the micro (μm) and nano (nm) scales, and down to the level of atoms and molecules. By drawing on examples from nature, he also demonstrated the feasability of reaching these boundaries, e.g. in data storage and in mechanical devices.

In the last decade alone desk-top computer data storage has increased capacity over 500-fold. From single-sided 5¼″ floppy disks, able to hold approximately 200KB of data, the storage capacity available on the desk-top has today reached 120MB on the 3½″ removable optical disk drives[†] . The advent of the CD ROM (Compact Disc Read-Only Memory), with a capacity of

---

[†] A byte is the amount of storage space necessary to hold one alphanumeric character. This is equal to eight bits, the smallest unit of data recognizable by the computer. A kilobyte (KB) equals 1,024 or 2^{10} bytes; a megabyte (MB) equals 1,048,576 or 2^{20} bytes; and a gigabyte (GB) equals 1,073,741,824 or 2^{30} bytes.

approximately 700MB, has pushed data access to even higher levels, thus openning new possibilities in areas such as the much-hyped world of interactive multimedia. Has the lower limit of miniaturization been reached yet? Observing nature provides some clues. For instance, biologists have long known that enormous amounts of information can be carried in an exremely small space, e.g. in the double-helixed DNA molecule (100,000 genes, 6 billion "letters" of code) in which roughly 50 atoms are used for one bit of information [2.2]. All of the information that man has accumulated in all the books in the world (approx. 10^{15} bits, or over 100,000 GB) can be written in this form in a cube of material merely 0.1 mm on each side [2.2]. Clearly there is still a *lot* of room for advancement.

As for mechanical devices, miniaturization again has a long way to go. Watch gears, and jeweler's lathes were once regarded as marvels of miniaturization. These, however, do not even come close to their biological equivalents. Living cells can be regarded as an organized system of various kinds of molecular "machines" (of the order of 10 nm in size and composed mainly of protein molecules) [2.16]. These "machines" function as parts of the whole system, e.g. enabling bacterial cells to swim in water by rotating helical shaped flagella by a motor connected to the base of each flagellum and buried in the membrane [2.7]. Clearly, achieving greater miniaturization is physically possible. The question is how does one get there?

Although exotic ideas are ever-present in the realm of science fiction, e.g. the miniaturized submarine injected into the human bloodstream in the 1966 movie "Fantastic Voyage", they only generate real interest when their feasability is proven through actual developments that are of practical value. For actual realization of such advances, the development of basic technology through research, and of commercial applications are of paramount importance. A major technical breakthrough in a relevant technology often provides the spur for new advancements. In other instances, a successful transfer of technology from an already advanced field provides the necessary impetus. Most importantly, however, there needs to be a pressing need for such advances. The developments in miniaturization therefore take an unpredictable path, one of least resistance, and not necessarily along clear projected lines. The recent development of the biocapsule [2.26] and the new area of OncoMEMS^{TM} [2.27] are examples of practical application.

Less than a decade ago in the early 1980s, after the completion of two decades of IC development, electronics had reached a high level of sophistication. Microprocessors such as the Intel 80286 (introduced in 1984) packed more than 134,000 transistors onto one chip. The advanced photolithographic, thin-film deposition, and chemical and plasma etching techniques of IC microfabrication had achieved a high degree of miniaturization. The interface of these circuits with the non-electrical world was becoming the point of focus for engineering design [2.14]. The higher performance and lower cost of the new generation of microprocessors created a situation where devices such as sensors and their interfaces with circuitry would often cost many times more than the microprocessor itself. There was a pressing need for lower cost in both sensors and in their interface with the microprocessors.

Miniaturization can also satisfy some of the needs in the fields of medicine and space exploration. In medicine, for example, the size of a surgeon's incision is often more a function of the dimensions of the human hand and of the cutting instruments than of what the ailment requires.

Today, many medical procedures are handled without surgery, e.g. through ultrasound treatment; however, there are limitations to such procedures and actual physical intervention is often necessary. With miniaturized (and possibly self-propelled) cutting machines, some of these procedures could conceivably be achieved through a simple injection into the bloodstream [2.26]. In space exploration, payload limitations are of paramount importance. The weight reductions offered by miniaturization can therefore be very beneficial.

The breakthrough in sub-millimeter sized miniaturization of mechanical devices was achieved through the adaptation of the refined techniques used in electronics. A better understanding of the mechanical properties of silicon [2.17] coupled with the adaptation of IC microfabrication techniques led to initial use of silicon as a miniaturized mechanical component [2.5]. This demonstrated the practicality of what is now known as surface micromachining. The application of bulk- and surface-micromachining techniques greatly stimulated research in micromechanical structures and devices. By relying on an already developed body of technology, great advancements were made in a very short period of time. Just as valves were first replaced by transistors and then by integrated circuits, ultimately leading to the development of the microprocessor, mechanical devices interfaced with electronics, such as sensors, have, in recent years been shrunk down in size. This has been accompanied by the ensuing benefits of lower device costs (through mass production), lower interface costs (through on-chip integration), smaller size, and lower weight. It has been predicted that MEMS is a technology that could be to the beginning of the 21st century what the integrated circuit was to the end of the 20th century.

Feynman's conjectures in 1959, as he himself pointed out, were only limited by the level of technological advancement of that day. Today, many of these technological boundaries have been crossed and some have been extended several orders of magnitude, e.g. in the fields of IC fabrication, magnetic and optical data storage, atomic force microscopy, etc. We are now at a point where many of Feynman's conjectures are approaching reality, if not already achieved in one form or another.

2.2.2 MEMS Today

Today, silicon-micromachining based devices have found many commercial applications. Completely assembled mechanisms and motors, fractions of a millimeter in size, are being made in labs around the world. Yet, although tiny motors made micromechanics famous (beginning in 1988 with the 60 μm diameter micromotor developed at the Berkeley Sensor and Actuator Center), it is sensors that currently dominate the commercial sector. Thus far, the silicon diaphragm pressure sensor has been the primary commercial success, with its main uses being in the automotive and medical fields (see Fig. 2.1). For instance, General Motors (GM) currently produces 750,000 air pressure sensors per month for use in engine intake manifolds. In medicine, approximately 10 million disposable blood-pressure sensors are used each year [2.18]. Sensors used for measuring gas concentrations have also been developed. Filters for the removal of viruses from plasma derivatives and biological fluids are scheduled for commercial production in the first quarter of 1997.

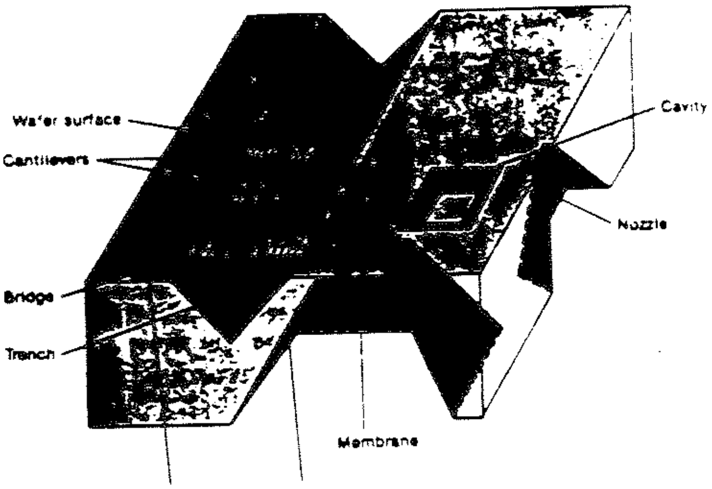

Fig. 2.1 Pressure Sensor

Currently, silicon accelerometers are being developed for active suspension and air-bag deployment in the automotive industry. Companies such as IC Sensors, NovaSensor, and Analog Devices already have such products on the market, whilst many others (HP, Motorolla) anticipate introducing products to the market in the very near future. Micromachines, however, are still largely research curiosities due to an array of difficulties such as suppressing friction, connecting wires, etc.

The field of MEMS is multi-disciplinary, encompassing electrical, mechanical, and chemical engineering in addition to material science and engineering. The field has also spurred basic studies of the physics and chemistry of the materials and structures in the micro-scale.

The MEMS "community" is suitably structured to conduct R&D and promote the fast transfer of research developments into commercial products. In many countries, a co-operative gevernment-university-industry structure has been established. In the US this takes a decentralized form with centers built around different universities (e.g. the Berkeley Sensor and Actuator Center—BSAC, and the Biomedical Microdevices Workshop at Berkeley),. Government agencies such as the National Science Foundation (NSF), ARPA (defense related) and NASA are actively supporting research at universities. Private companies noted above, as well as Microfab Biosystems and IRIS Micromedical are also actively involved in R&D.

The major forums of discussion and presentation of new developments in the field of MEMS are the conferences and symposia that have been organized in recent years. The most important are the *International Conference on Solid-State Sensors and Actuators—Transducers* (held in June of odd-numbered years since 1981), regional conferences, e.g. the *IEEE Solid-State Sensor and Actuator Workshop* held in June of even-numbered years since 1984 in Hilton Head Island, S.C. in the US, and the annual *IEEE Mircro Electro Mechanical Systems Workshops,* held since 1989 in different US locations, and internationally since 1991. Additionally, there are the *Materials Research Society (MRS)* (Fall and Spring), the *American Society of Mechanical Engineers (ASME)* (Winter and Summer) twice-annual meetings, and the *Cambridge Healthtech* meatings at which specific symposia are often devoted to MEMS topics. Up-to-date reviews of research progress in the field can be found in the respective technical digests.

For archival publications, a number of journals catering specifically to the MEMS community have also been established, most notably the *Journal of Microelectromechanical Systems, IEEE Transactions on Electron Devices, Sensors & Actuators,* and the *Journal of Micromechanics and Microengineering.* Additionally, useful material can be found in related technical journals, notably the *Journal of Applied Physics* .

Despite the rapid pace of development, the field of MEMS has not yet reached maturity [2.4]. There is an exponential growth in new devices and gadgets. Although some developments have reached commercial application, most are at the prototype or developmental stages, especially in the case of micromotors. Strong efforts are underway to advance basic material research, process refinement, and material and structural modeling which are the basis upon which new developments can be built.

The schematic diagram of the "MEMS Technology Tree" in Fig. 2.2 [2.23], appropriately divides the on-going activities in the field into four categories: (i) the roots, consisting of the basic MEMS technologies; (ii) the lower trunk, consisting of functional elements; (iii) the upper trunk, where system integration and hybridization is achieved; and (iv) the "fruits" of MEMS, namely the successful commercial applications.

Thus, the current state-of-the-art in MEMS is a staggered patchwork of advancements and expertise spanning the four levels shown in Fig. 2.1. As is to be expected in any newly-developing field, the main advances have been in the lower or more basic levels, with only a few "fruits" having been picked to date. The future of the field, however, is very promising. Most immediately, for example, inexpensive yet highly reliable accelerometers and other sensors could revolutionize the design of suspension, braking, and steering systems in the automotive industry. This has prompted industry and government agencies around the world to pour millions of dollars of research money into MEMS research and development. In 1991, for instance, research spending in the US on MEMS amounted to $15 million, whilst it was $75 and $30 million in Germany and Japan, respectively.

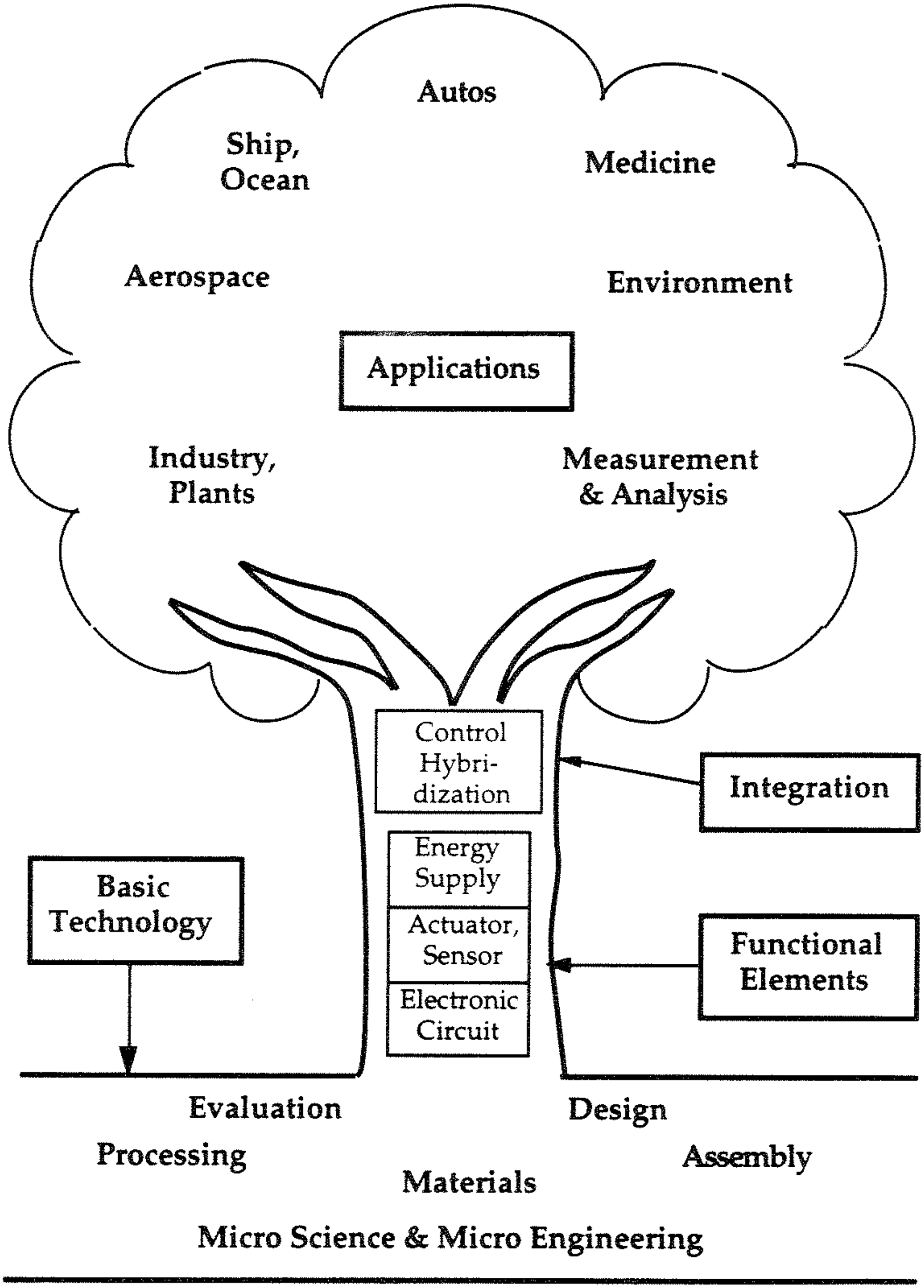

Fig. 2.2 MEMS Technology Tree

2.2.3 Challenges and Opportunities

Despite the many successes, there are numerous challenges that have had to be overcome in the field of MEMS, many of which still loom as barriers to development. Feynman [2.2] had foreseen some of the potential difficulties that are now faced such as the scaling of forces, resulting problems related to friction and lubrication, and material inhomogeneity resulting from the finite grain structure of polycrystalline materials.

The scaling of forces in the micro domain poses challenges and opens new opportunities for alternative device designs. For exampe, mass, and therefore inertia forces, scale as L^3, whereas magnetic forces scale as L^4 [2.21], i.e. when a system scales down a factor of ten in size, magnetic forces scale *down* by a factor of ten relative to the inertia forces (L^4/L^3). Conventional electric motors are typically magnetic motors. These clearly cannot perform in the micro domain where they may have to perform at sizes as low as one thousand times smaller than the smallest functioning magnetic motors— of the order of 1 mm in size [2.21]. Electrostatic forces on the other hand scale advantageously in the micro domain. Depending on the design of the micromachine, electrostatic forces scale as L^2 or L^1 [2.21]; thus when a system scales down in size by a factor of ten, electrostatic forces scale *up* by a factor of either ten or one hundred relative to the inertia forces (L^3/L^2 or L^3/L^1). The negligible electrostatic forces at the scales of conventional motors, for example, become a viable driving force with motors of appropriately small scale. Similarly, hydraulic forces (already useful in conventional macro applications), being caused by pressure (L^2), and surface tension (L^1), prove advantageous in the micro domain.

Material inhomogeneity at the micro-scale is another potential problem. Polycrystalline materials, be they metals, ceramics, or semiconductors have a microstucture of finite size. When the smallest dimensions of a device made of these materials is of the order of the microstructural dimensions (often grain size), the concept of material homogeneity no longer applies. For these cases, conventional mechanical models would not predict the structural responses, thus hampering the design and development of such devices. Furthermore, statistical uncertainty may become important, thus requiring probabilistic analysis of the structural response. In §2.4, the fabrication methods are shown to play a major role in determining the material microstructures. Chapter 3, where approaches to modeling the mechanical behavior of MEMS materials are discussed, further expands on these issues as well as exploring the existing work in the field. In Chapters 4, 5, and 6, models are presented that attempt to take into account the material inhomogeneity and statistical uncertainty described above.

2.2.4 Future Direction

Achieving successful commercial applications for micromachines represents the next anticipated milepost in MEMS. The basic technology in this area is reaching critical mass and is anticipated to produce numerous applications in the next decade. The feasibility to use expensive high performance materials (since only small amounts are required) is another source of promise. With the development of non-silicon fabrication techniques (see §2.4), further advancements along this line can be expected in the near future.

Beyond that which we can envisage today, however, there are doubtless other opportunities for fruitful advances. The continued advancement of basic technologies will in the future produce the hoped-for results. New technologies can radically alter an evolving field in unforeseeable ways. The evolution of mechanized writing serves as a simple example of this trend. The typewriter performs by imprinting individual letters, numbers, and symbols on a piece of paper by depressing a pre-moulded metalic protrusion over an ink ribbon. The progress of the typewriter from the earliest manual "hammer" style models, through to electric machines (faster) and electric "golf-ball" machines and eventually daisywheel-based machines (changeable letter styles) only represented incremental improvements over the original typewriter. New technologies were being utilized to incrementally refine and improve upon the original concept. Even the advent of the "dot-matrix" printer—enabling the reproduction of a variety of symbols and graphics—still used the same concept of impact printing. Ultimately, however, speed and quality limitations were reached that could only be overcome by abandoning impact printing and coming up with a new concept. The advent of the laser printer represented such a breakthrough.

Technological breakthroughs, therefore, open up new possibilities for improving existing functions by quantum leaps rather than by incremental steps. They often lead to areas of applications that we are simply incapable of envisaging today. The ingenuity of designers in incorporating new advancements in novel ways coupled with the utilization of the new possibilities opened up in the micro domain promise to produce many years of innovative designs in the field of MEMS.

Perhaps the most exciting prospect for micromechanics is as a prelude to nanomechanics. Some believe that for micromechanics to succeed, it must keep pace with advances in electronics in the sub-micron domain (e.g. size of some circuit elements are in the sub-micron category). Nano-technology represents a thousand-fold reduction in length scales as compared with current MEMS. It represents the final frontier of miniaturization, at the scale of atoms and molecules, that Feynman had alluded to [2.2]. Developments in this field, however, are at an even earlier stage than those in the micro-domain. Nevertheless, commercial nanomachines once thought to be perhaps decades away are now in development stage [2.26].

2.3 EXAMPLE DEVICES

The folded beam lateral micro resonator (FBLMR) has been used extensively in many applications in the field of MEMS. For example, FBLMRs have been used as accelerometers for active-suspension systems and for air-bag deployment in the automotive industry, as gas concentraion sensors, and in micromechanical filters used in signal processing. The original design is attributed to W. C.-K. Tang [2.19] who developed the device at the Berkeley Sensor and Actuator Center (BSAC). The device is shown schematically in Fig. 2.3 and consists of folded beams acting as springs, anchored to the plane, and attached to a central mass which expands into a comb structure. This arrangement is either driven electrostatically from one side and sensed capacitively at the other side with the comb structures or, alternatively, a push-pull drive using the two combs 180° out of phase is used to drive the structure.

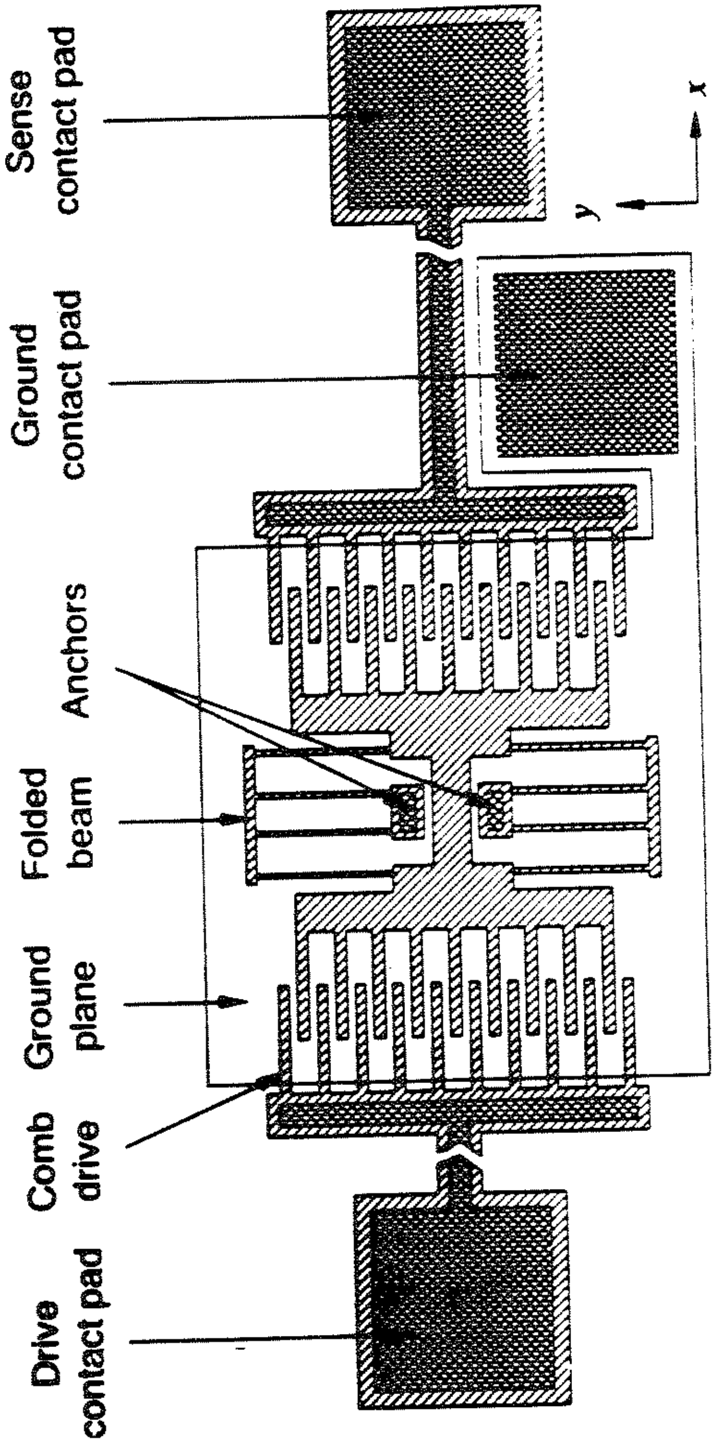

Fig. 2.3 Folded-Beam Lateral Micro Resonator (FBLMR)

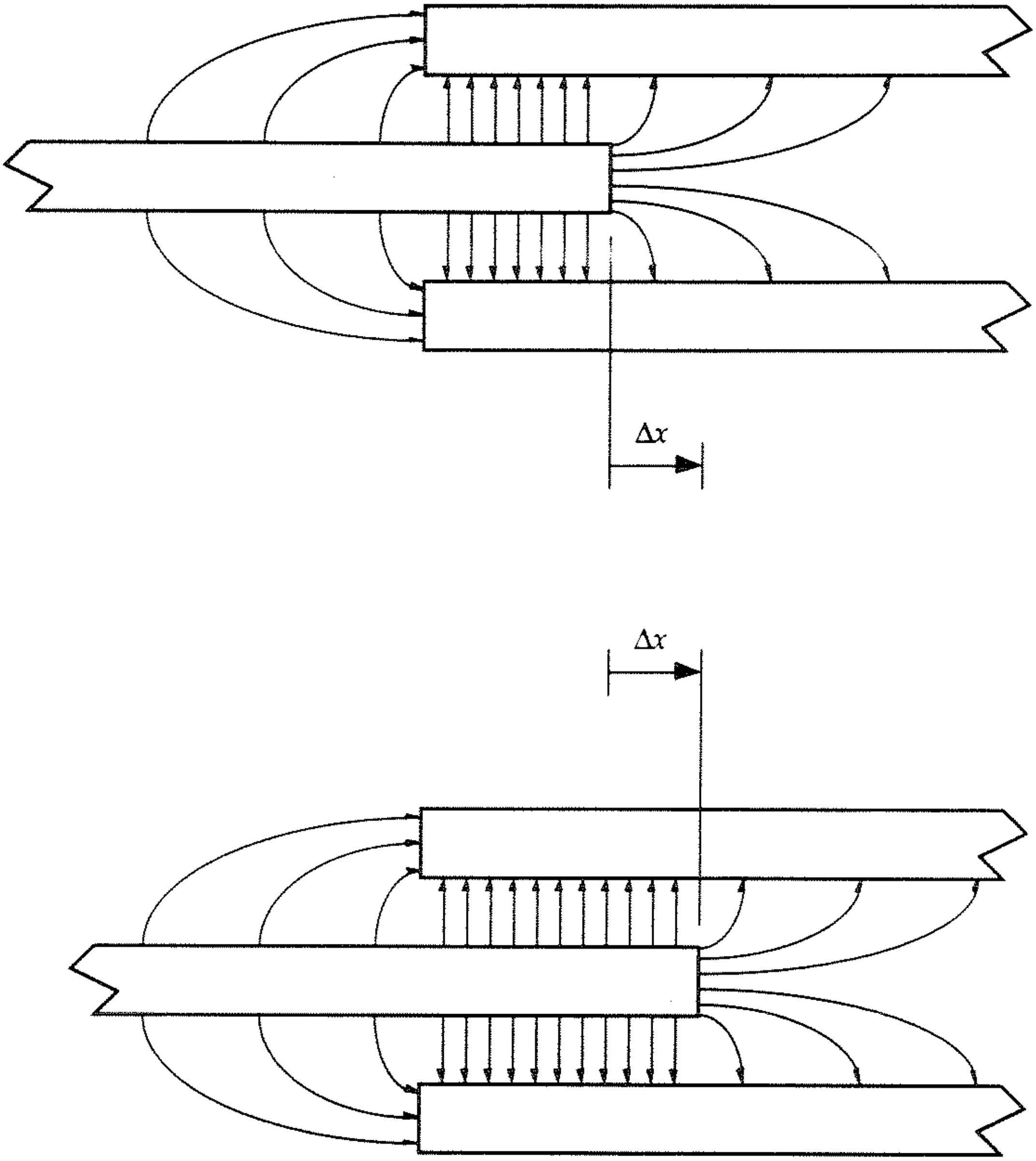

Fig. 2.4 Electrostatic Field Around Combs

Constant in-plane electrostatic excitation is achieved using the lateral-mode comb drive [2.20]. The electrostatic field distributions shown in Fig. 2.4 schematically demonstrate how the lateral electrostatic force is independent of the lateral movement Δx.

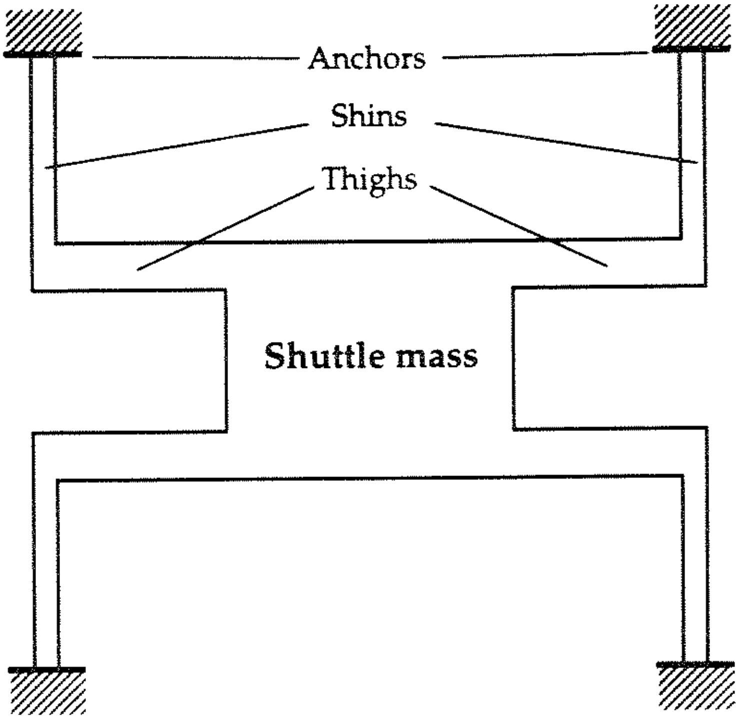

Fig. 2.5 Fixed-Fixed Beam (Crab-Leg) Lateral Resonator

The folded beam design is an elegant solution to some of the problems inherent in structures produced using thin-film deposition. Residual stresses resulting from the fabrication process (see §2.4) are minimized since the structure is free to expand out along the length of the beams, away from the anchor points. Additonally, unlike a fixed-fixed vibrating beam system (Fig. 2.5), extensional axial stresses do not dominate during large-amplitude vibrations, thus simplifying the structural analysis and resulting in a linear spring model for the dynamic analysis.

The folded-beam lateral resonator also has promising applications in micromotors. The comb-drive-based microengine shown in Fig. 2.6 [2.3] is such an example. The drive motions need to be 90° out of phase in order to achieve rotary motion in the output gear.

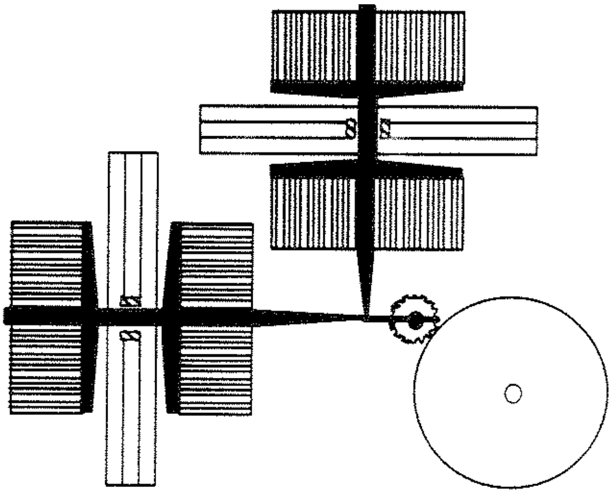

Fig. 2.6 Comb-Drive-Based Microengine

2.4 FABRICATION TECHNIQUES

As has been pointed out, silicon fabrication techniques have been the cradle of micromechanics. Research efforts in all parts of the world are accelerating these developments. The basic processes involved are those of deposition, patterning, and selective etching of various layers of material which are typically on the order of 0.02 μm to 8 μm thick. The resulting structures are mostly planar. Many other techniques, however, are developing such as LIGA (an abbreviation of the german term LIthographie Galvanoformung Abformung—lithography, electroforming, and plastic molding), HEXSIL [2.24], EDM machining, and single-point diamond machining, molding, and plating, that can augment the silicon fabrication process [2.22]. LIGA, for instance, combines lithography, electroforming and microinjection moulding and can realize any cross-section shape and work with a wide variety of materials. A good review of the above is presented by Delapierre [2.1].

The sacrificial layer method is the most commonly used technique of fabricating micro-structures. In one version of this process, a thin film of polycrystalline silicon (polysilicon), typically around 2 μm thick, is deposited by low pressure chemical vapor deposition (LPCVD) at a temperature of approximately 600°C on a continuous layer of phosphosilicate glass (PSG)—see Fig. 2.7. This is followed by a second PSG layer. Next, the wafer is subjected to an anneal period (ranging from 20 minutes up to 4 hours) at temperatures in the 900–1100°C range, where phosphorous doping is achieved by diffusion from two layers of PSG which sandwich the structural layer. The upper PSG is then stripped, the structural silicon layer is patterned and etched and then the sacrificial PSG under the structure is removed by a timed etch using hydrofluric acid (HF). Fig. 2.8 shows the plan view of a silicon wafer and a typical arrangement of the individual, replicated dies and Fig. 2.9 shows the steps in the process sequence outlined above [2.20].

The process outlined above involves a number of variable parameters, each of which can have an important influence on the microstructure of thin-film polysilicon, the resulting structural material. The annealling and doping are performed in order to achieve two main objectives: (i) reducing residual stresses, and (ii) achieving desired electrical properties. The anneal temperature and time, and the dopant concentration all influence important features of the material microstructure such as average grain size, texture (see §3.3), and residual stresses. The most detailed study of residual stresses in thin films and their relation to texture and process conditions is found in the

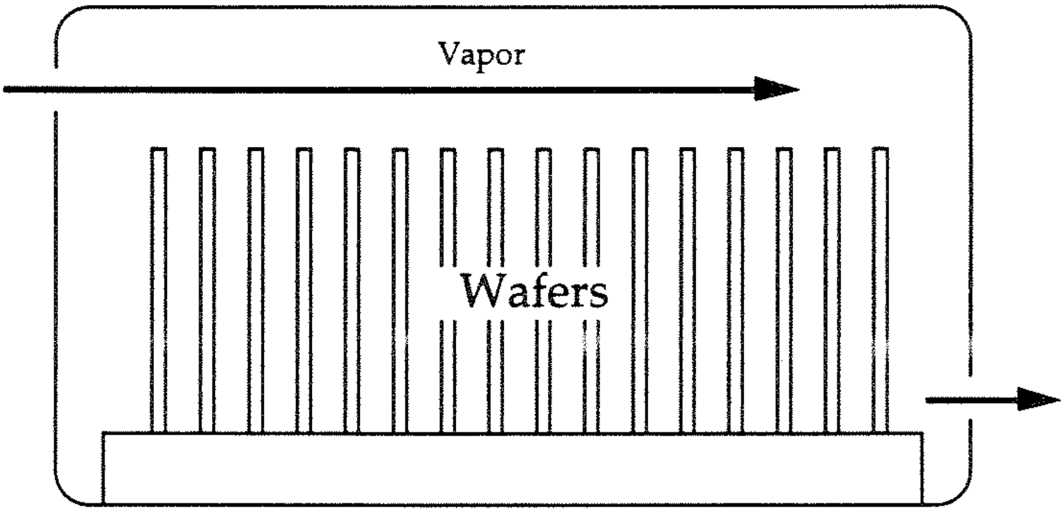

Fig. 2.7 Low Pressure Chemical Vapor Deposition (LPCVD) of Wafers

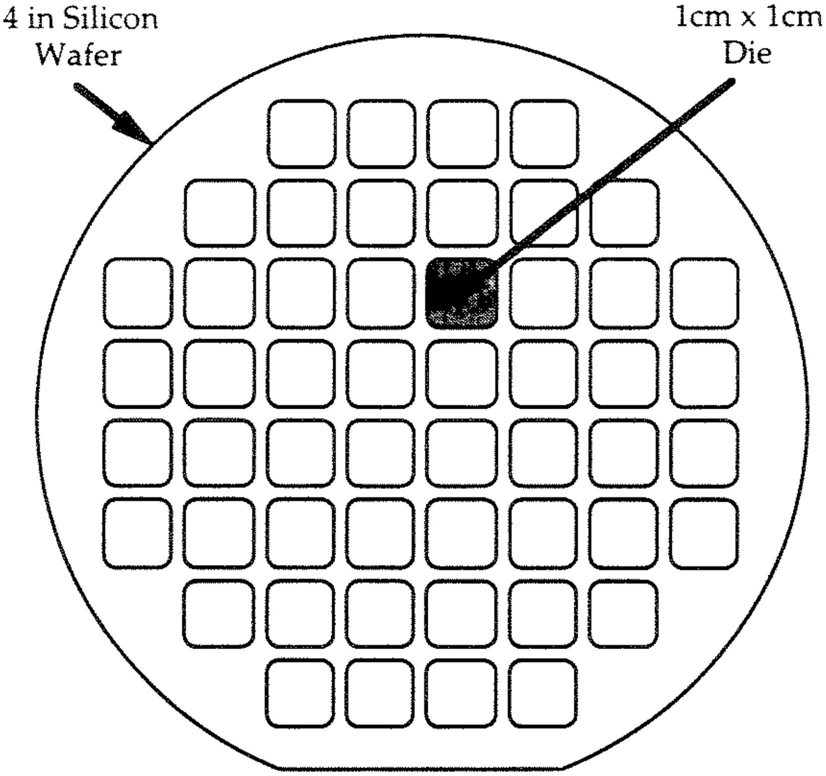

Fig. 2.8 Silicon Wafer & Die

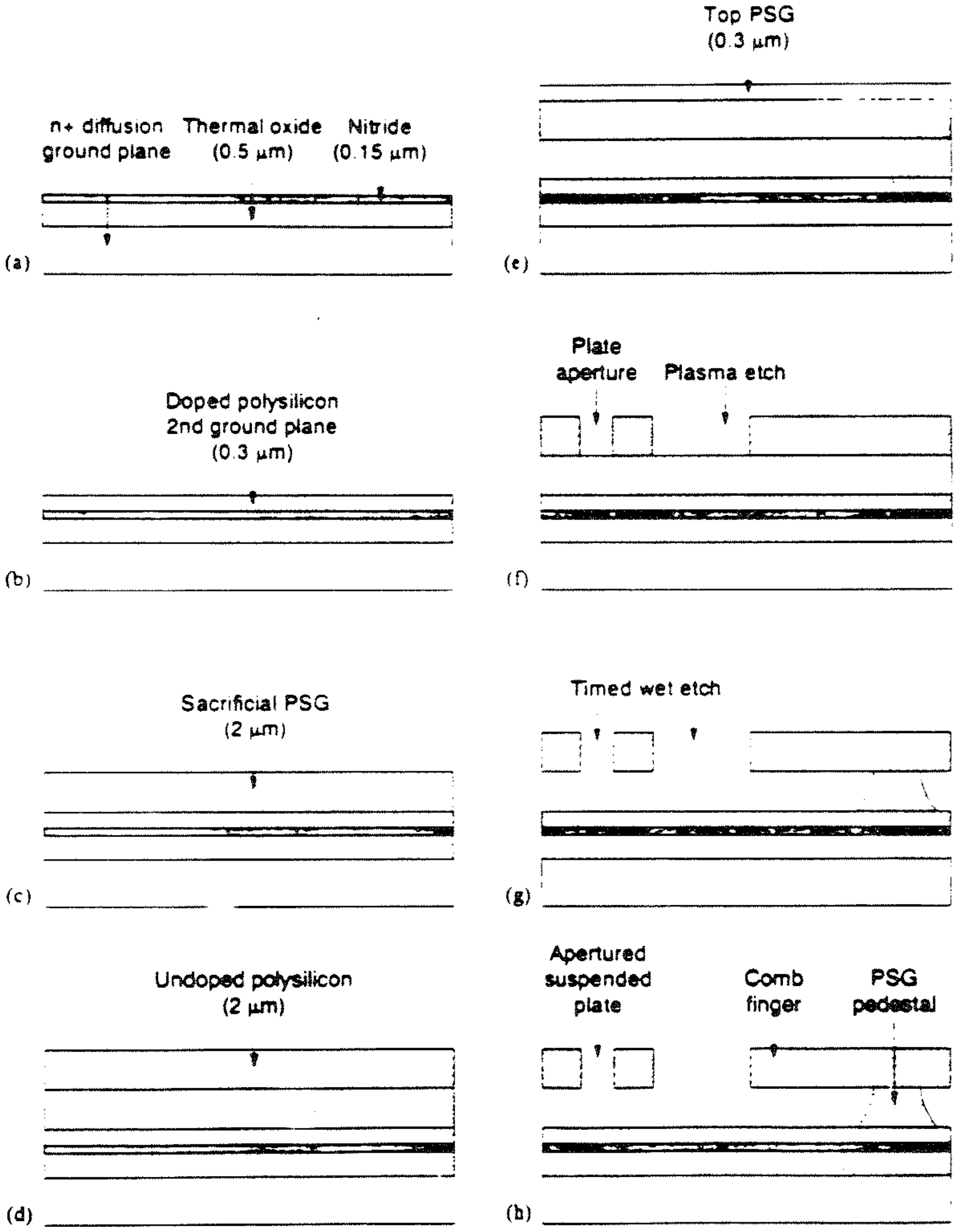

Fig. 2.9 Process Sequence

series of papers by Krulevich et al. [2.6, 2.8, 2.9, 2.10, 2.11, 2.12, 2.13]. Knowing the process conditions, the grain morphology and the crystallographic texture can be predicted. These can then be used in the mechanical modeling of the material (see Chapters 4, 5, and 6). Simultaneous determination of texture, residual stresses, and crystallographic parameters may be achieved with the diffraction method of Ferrari et al. [2.25].

2.5 SUMMARY

This chapter gives an introduction to the field of MEMS for readers unfamiliar with the field. Background is provided by outlining the trend towards miniaturization. The evolution of MEMS is seen as a natural extension of this trend. The most promising developments in MEMS have been both inspired and nurtured by the advanced field of IC fabrication. After achieving a better understanding of the mechanical properties of silicon, these advanced IC fabrication techniques were used to develop early MEMS. The current state-of-the-art in MEMS is then reviewed. The scaling effects in the micro-domain present both challenges and opportunities for device development. Pointers are outlined for the future direction of this field as a precursor to nanomechanics. Example devices are described, most notably the folded-beam linear lateral resonator, followed by a brief description of the fabrication process as it relates to the microstructure of materials.

CHAPTER 2 REFERENCES

[2.1] Delapierre, G., "Micro-Machining: A Survey of the Most Commonly Used Processes," *Sensors and Actuators*, Vol. 17, pp. 123–138, 1989.

[2.2] Feynman, R. P., "There's Plenty of Room at the Bottom," *Journal of Microelectromechanical Systems*, Vol. 1, No. 1, pp. 60–66, 1992.

[2.3] Garcia, E.J. and J.J. Sniegowski, "The Design and Modelling of a Comb-Drive-Based Microengine for Mechanism Drive Applications," *The 7th International Conference on Solid-State Sensors and Actuators (Transducers '93)*, June 7–10, 1993, Yokohama, Japan, pp. 763–766.

[2.4] Howe, R. T., R. S. Muller, K.J. Gabriel, and W.S.N. Trimmer, "Silicon Micromechanics: Sensors and Actuators on a Chip," *IEEE Spectrum*, pp. 29–35, July 1983.

[2.5] Howe, R. T., and R. S. Muller, "Resonant-Microbridge Vapor Sensor," *IEEE Transaction on Electron Devices*, ED-33, pp. 499–506, 1986.

[2.6] Huang, J, P. Krulevitch, G.C. Johnson, R.T. Howe, and H.R. Wenk, "Investigation of Texture and Stress in Undoped Polysilicon Films," *Mat. Res. Soc. Symp. Proc.*, Vol. 182 (1990) p. 201.

[2.7] Koppel, T., "Learning How Bacteria Swim Could Set New Gears in Motion," *Scientific American*, pp. 168–169, September 1991.

[2.8] Krulevitch, P., Tai D. Nguyen, G.C. Johnson, R.T. Howe, H.R. Wenk, and R. Gronsky, "LPCVD Polycrystalline Silicon Thin Films: The Evolution of Structure, Texture, and Stress," *Mat. Res. Soc. Symp. Proc.*, Vol. 202 (1990), p. 167.

[2.9] Krulevitch, P., R.T. Howe, G.C. Johnson, and J. Huang, "Stress in Undoped LPCVD Polycrystalline Silicon," *Digest of Technical Papers, Transducers '91*, San Francisco, CA (1991) p. 949.

[2.10] Krulevitch, P., G.C. Johnson, and R.T. Howe, "Stress and Microstructure in LPCVD Polycrystalline Silicon Films: Experimental Results and Closed Form Modeling of the Stresses," *Mat. Res. Soc. Symp. Proc.*, Vol. 239 (1991) p. 13.

[2.12] Krulevitch, P. Ph.D. Dissertation, University of California at Berkeley, 1994.

[2.11] Krulevitch, P., G.C. Johnson, and R.T. Howe, "Stress and Microstructure in Phosphorus Doped Polycrystalline Silicon," *Mat. Res. Soc. Symp. Proc.*, Vol. 276 (1992) p. 79.

[2.13] Monk, D.J., P. Krulevitch, R.T. Howe, and G.C. Johnson, "Stress-Corrosion Cracking and Blistering of Thin Polycrystalline Silicon Films in Hydrofluoric Acid," presented at the *Materials Research Society Spring Meeting*, San Francisco, CA, Stress and Mechanical Properties of Thin Films IV, 1993.

[2.14] Muller, Richard S., "Microdynamics," *Sensors and Actuators*, A21-A23, pp. 1-8, 1990.

[2.15] O'Connor, L., "MEMS: Microelectromechanical Systems," *Mechanical Engineer*, February, 1992.

[2.16] Oosawa, F., "Molecular Machines in Living Cells," *The 7th International Conference on Solid-State Sensors and Actuators (Transducers '93)*, June 7–10, 1993, Yokohama, Japan, pp. 17–21.

[2.17] Petersen, Kurt (1982). "Silicon as a Mechanical Material," *Proceedings of the IEEE*, Vol. 70, No. 5, pp. 420-457.

[2.18] Stix, G., "Golden Screws," *Scientific American*, pp. 166–169, September 1991.

[2.19] Tang, W. C., T.-C. H. Nguyen, and R. T. Howe, "Laterally Driven Polysilicon Resonant Microstructures," *Sensors and Actuators*, Vol. 20, pp. 25–32, 1989.

[2.20] Tang, W. C., "Electrostatic Comb Drive for Resonant Sensor and Actuator Applications," Ph.D. Dissertation, University of California at Berkeley, October 1990.

[2.21] Trimmer, W. S. N. and K. J. Gabriel, "Design Considerations for a Practical Electrostatic Micro-Motor," *Sensors and Actuators*, Vol. 11, pp. 189-206, 1987.

[2.22] Trimmer, W.S.N., Editorial, *Journal of Microelectromechanical Systems*, Vol. 1, No. 1, p.1, 1992.

[2.23] MEMS Technology Tree

[2.24] Keller, C. and M. Ferrari, "Milli-Scale Polysilicon Structures," *Solid State Sensor and Actuator Workshop*, IEEE, Hilton Head, June 1994, pp. 132-137.

[2.25] Ferrari, M. and L. Lutterotti, "New Method for the Simultaneous Determination of Anisotropic Residual Stress and Texture by X-Ray Diffraction," *Journal of Applied Physics*, Vol. 76, No. 11, pp. 7246-7255, 1994.

[2.26] Ferrari, M. et al., "Silicon Nanotechnology for Biofiltraion and Immunoisolated Cell Xenografts," *MRS Fall Meeting*, 1995.

[2.27] Ferrari, M. "Microfabricated Therapeutic Compound and their Methods of Use," Invention Disclosure UCB Case B 93-045-2, Office of Technology Licensing, University of California at Berkeley. Patent pending.

Chapter 3

MECHANICAL MODELING OF MEMS

3.1 INTRODUCTION

Existing approaches to the modeling and analysis of MEMS materials and structures have performed adequately in many applications. However, the underlying assumptions regarding material properties limit these approaches. Although increasingly sophisticated structural models are being employed in analyzing the mechanical behavior of MEMS [3.2, 3.12, 3.21], the material is typically assumed to be homogeneous and isotropic. Certain processes in MEMS fabrication (§2.4), coupled with the length scales associated with the new frontiers of MEMS technology, however, result in structures for which these simplifying material assumptions are inappropriate. More realistic material models which adequately describe the mechanical behavior of such structures are therefore needed. This chapter serves to demonstrate this need and presents an overview of improved modeling approaches.

The structure of silicon, ranging from the atomic to macroscopic scales, is first introduced for the single crystal and polycrystalline states, including a description of the grain boundary phase. This is followed by a description of texture in polycrystalline silicon. Next, the elastic stress-strain relations for crystalline silicon are described. Current approaches to modeling and analyzing MEMS materials and structures are then reviewed. Shortcomings of these approaches with regard to polycrystalline MEMS structures are discussed in the context of the developments of the earlier sections. Finally, an overview of improved modelling techniques and approaches is presented. These techniques are drawn from numerous fields including homogenization, computational materials science, and rock mechanics, and employ deterministic and stochastic finite element methods, Monte Carlo simulations, and random field theories.

As in Chapter 2, the emphasis is primarily on planar or thin-film polycrystalline silicon. Nevertheless, with minor modifications, the developments presented here are applicable to other materials and geometries.

3.2 STRUCTURE OF SILICON

3.2.1 Crystalline and Polycrystalline States

The various processing techniques for silicon govern the different final states of the material. At one extreme the material can be "grown" as a single crystal, while at the other extreme a structureless and disordered amorphous state can be achieved. The state in between is called the polycrystalline state. The LPCVD method of material processing, used extensively in MEMS fabrication (see §2.4), with the subsequent annealing step to relieve residual stresses, generally results in polycrystalline thin films. We shall therefore concentrate on this state of silicon. However, knowledge about the single crystal structure and its properties is important since the polycrystal is composed of individual crystal grains.

The most typical form in which inorganic non-metallic materials occur is crystalline. This phenomenon is related to the tendency of particles—atoms, ions, or molecules—to adopt a spatial arrangement in equilibrium with the forces of their interaction. This results in a state of minimum energy. There are seven classes of crystalline structure, each with its distinct spatial arrangement of particles in a lattice: cubic, tetragonal, rhombohedral, hexagonal, orthorhombic, monoclinic, and triclinic [3.18]. Single crystal silicon has a diamond cubic structure shown in Fig. 3.1, where the atoms at vertices or at the center of outside faces are shown in black while the atoms inside the cube are shown in white.

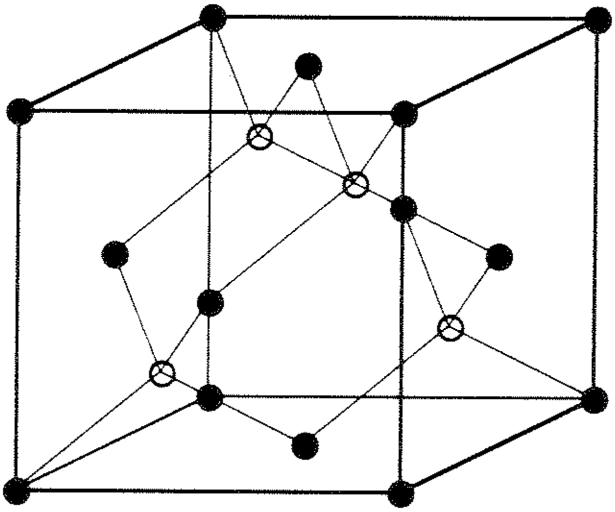

Fig. 3.1 Diamond Cubic Structure of Silicon Crystals

Properties of crystals are directional and vary with the orientation of the crystal latice. A common method of describing orientations is using *Miller indices* [3.18] which define different lattice planes. These indices are represented as three numbers enclosed in parentheses, (k,m,l). By convention, k, m, and l represent the reciprocals of the intercepts of a given plane with the crystal axes. For cubic crystal structure, the crystal axes coincide with cartesian coordiante axes as shown in Fig. 3.2. To illustrate this concept, six different lattice planes are shown in the figure, where, by convention, a bar over an index indicates a negative number. When only the orientation of a plane needs to be indicated, all three numbers are divided by the greatest common factor, and the positive values are taken. For example, the orientation of planes (110) and (330) are identical and are defined simply as (110).

The cubic crystal structure of silicon results in crystals that have identical configurations in certain non-parallel planes. Crystallographically equivalent planes are represented by the Miller indices of one of the planes but are enclosed in braces instead of parentheses, e.g. {100} describes the equivalent planes oriented parallel to any side of the cube.

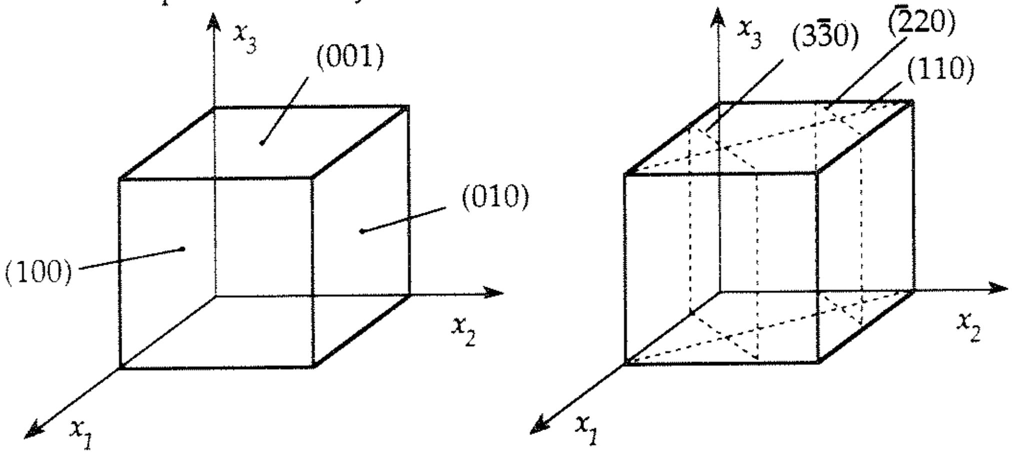

Fig. 3.2 Miller Indices of Lattice Planes

Imperfections such as voids, inclusions, impurities (e.g. dopants), and line and point defects can also be found in crystals. Lattice defects normally result in a 0.1% deviation of elastic moduli [3.18]. Dislocations typically contribute to approximately 1% error—an apparent lowering of elastic moduli of the dislocated crystallite compared to defect-free ones [3.18]. For a linear-elastic material model, these flaws are small and can generally be neglected. These imperfections do, however, play an important role in the inelastic behavior of the material, e.g. brittle fracture, plastic slips, etc.

Polycrystalline silicon is a one-phase aggregate of crystal grains, with individual grains distinguished from adjacent neighbors according to their distinct crystallographic orientations with respect to a global-fixed frame. Separating neighboring grains, there exists a grain boundary region, usually on the order of a few inter-atomic spacings, the properties of which are generally different from the crystalline state. Adjacent crystal grains are by definition differently oriented, thus resulting in a discontinuous variation of material properties from point to point within a sample. This variation is generally random in nature and its characteristics are defined by the sample *texture* [3.3] and are related to the processing conditions for the polycrystal (see §3.2.2).

Grain boundaries (GBs) in a polycrystal are generally considered as a disordered phase between misoriented adjacent crystal grains. In many polycrystals the thicknesses of these GBs are extremely small, on the order of one atomic distance. In order to better visualize GBs the concept of a *coincidence site lattice* is introduced. There are a number of mutual arrangements of grains with a misorientation angle of θ at which a certain number of lattice points of the structure of grains in contact coincide. It is assumed that the mutual orientation of the structures of the neighboring grains at which the most coincidences of lattice points occur is energetically preferred (minimizing the grain boundary energy). This principle is illustrated in Fig. 3.3 [3.18], where two crystal grains of identical structure are mutually disoriented at an angel θ. Also shown is the extent of the GB region (shown shaded) where the arrangement of atoms is different from the crystal lattice structure. This GB region may be wider for non-coinciding lattices.

As seen in Fig. 3.3, the distances between atoms in the GB region (shaded) deviate from those in the interior of the grains and thus cohesive forces

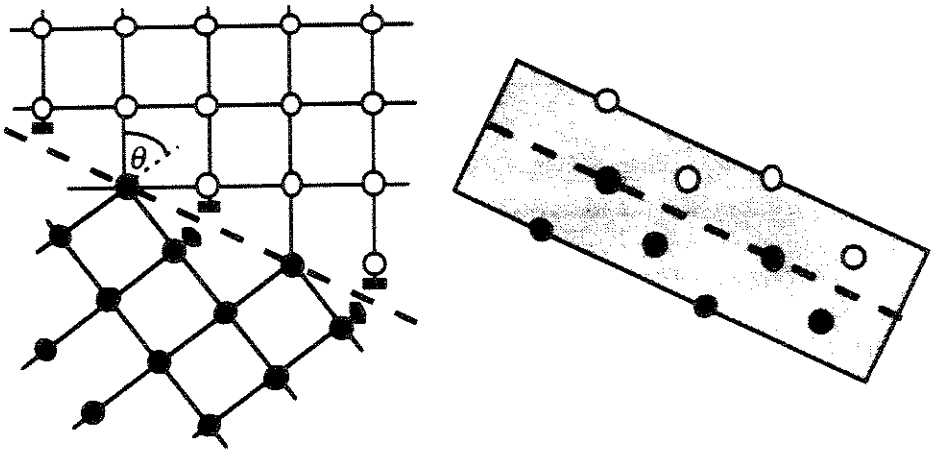

Fig. 3.3 Grain Boundary Angle and Region

between the atoms are also different. The magnitude and resultant directions of these cohesive forces translate into macroscopic material properties such as elastic moduli. As a result, therefore, the GB volume behaves as a separate phase different from the bulk crystals. For linear elastic behavior, this influence can be neglected for most purposes since the volume fraction of GBs is generally negligible compared to the grains. However, due to their effects on propagating slip systems, and their role in phenomena such as fracture, the influence of the GBs on inelastic properties is significant [3.18].

The structure of polycrystals indicates that it is inhomogeneous in the microscopic scale. However, as is the case for many structural materials such as steel (also a polycrystal), the inhomogeneities are at a scale that is several orders of magnitude smaller than the smallest dimension of structural members. For example, a cubic inch of steel contains millions of crystal grains. This disparity in scales allows statistical averaging to be valid and a homogeneity assumption can be made for the material. For polysilicon too, these same assumptions can hold. Indeed, these assumptions have been the basis for most material models in the field of MEMS. Due to the small scales associated with MEMS, however, the validity of this assumption cannot be guaranteed for all cases. Certain process conditons coupled with small dimensions of structural members can result in cases where the homogeneity assumption is no longer valid. In such cases, other approaches that take into account the inhomogeneity of the material must be pursued. Examples are provided in Chapters 5 and 7 that clearly demonstrate this problem.

3.2.2 Texture in Polysilicon

The crystal grains in a polycrystal often have non-random crystallographic orientations. The polycrystal is then said to be *textured* [3.3]. Others associate the term texture to the "preferred orientation of the grains within the polycrystalline aggregate" [3.25].

Texture may arise in a material due to the action of anisotropic solid state processes, such as crystallization, plastic deformation, recrystallization and grain growth, phase transformations, etc. [3.3]. In the context of MEMS and surface machining technology, the LPCVD process and the associated temperature, pressure, anneal time, and dopant concentration are the factors which act to affect the texture (see Fig. 5.1 for a TEM of polysilicon).

In the case of a uniformly random orientation of grains, the polycrystal behaves isotropically on the macroscopic scale and is referred to as a *macroisotropic* material. However, for textured material samples, the overall macroscopic behavior is anisotropic. Techniques exist, such as homogenization (see Chapter 4) through which the macroscopic properties may be estimated based on the single-crystal properties and the material texture. Essentially, a weighted averaging is made over the range of grain orientations. This averaging, however, typically results in bounds on material properties such as elastic moduli. The material texture descriptor most used for this averaging is the orientation distribution function (ODF). The ODF is analogous to a probability density function (PDF) and essentially defines the distribution of the volume fraction of crystallites in the orientation space.

Higher-order textural descriptors have been developed, such as the n-point correlation functions, or orientaion coherency functions (OCFs), or the misorientation distribution function (MDF) [3.19]. These descriptors are useful in describing information beyond what the ODF provides and lead to closer bounds in the homogenization of material properties. A more detailed discussion of this topic can be found in §4.2.2.

3.3 ELASTIC STRESS-STRAIN RELATIONS FOR CRYSTALLINE SILICON

The mechanical behavior of single crystals forms the basis for modeling the mechanical behavior of polycrystals. The following subsections describe in detail the stress-strain relations for crystalline silicon, with an extensive description of coordinate transformations. These tranformations are relevant in predicting the behavior of polycrystals.

3.3.1 Stress and Strain

The symmetric second-ranked *Green-St. Venant strain tensor* is defined by

$$E_{ij} = \tfrac{1}{2}\left(u_{j,i} + u_{i,j} + u_{k,i}u_{k,j}\right) \tag{3.1}$$

where u_i is the displacement in direction i, $u_{i,j}$ denotes the partial derivative $\partial u_i / \partial x_j$ with respect to the spatial coordinate x_j, and where the usual indicial "implied summation" notation is used [3.11]. Defining the tensors ε_{ij} and ω_{ij}

$$\varepsilon_{ij} = \tfrac{1}{2}\left(u_{j,i} + u_{i,j}\right) \tag{3.2}$$

$$\omega_{ij} = \tfrac{1}{2}\left(u_{i,j} - u_{j,i}\right) \tag{3.3}$$

and noting that $u_{i,j} = \varepsilon_{ij} + \omega_{ij}$, we can rewrite Eq. 3.1 as

$$E_{ij} = \varepsilon_{ij} + \tfrac{1}{2}\left(\varepsilon_{ik}\varepsilon_{jk} - \varepsilon_{ik}\omega_{jk} - \omega_{ik}\varepsilon_{jk} + \omega_{ik}\omega_{jk}\right) \tag{3.4}$$

For small strains, i.e. $\left|\varepsilon_{ij}\right| << 1 \; and \; \left|\omega_{ij}\right| << 1$, one can ignore the product terms in Eq. 3.4 and approximate E_{ij} with ε_{ij}, the *infinitesimal strain tensor* defined in Eq. 3.2.

Taking stress to imply the force per unit area inside the structure of the material, for an infinitessimal cube of material, oriented in the direction of the coordinate axes, σ_{ij} is the stress acting in the *jth* direction on the face perpendicular to the *ith* axis.

The stress and strain tensors are both symmetric [3.11], i.e.

$$\sigma_{ij} = \sigma_{ji} \tag{3.5}$$

and

$$\varepsilon_{ij} = \varepsilon_{ji} \tag{3.6}$$

Therefore, there are only six independent components for each tensor.

It is convenient to use the "contracted" or matrix notation to represent the six independent components of stress and strain. The following column matrices thus represent stress and strain vectors, respectively,

$$\boldsymbol{\sigma} = \begin{Bmatrix} \sigma_{11} \\ \sigma_{22} \\ \sigma_{33} \\ \sigma_{23} \\ \sigma_{13} \\ \sigma_{12} \end{Bmatrix}, \quad \boldsymbol{\varepsilon} = \begin{Bmatrix} \varepsilon_{11} \\ \varepsilon_{22} \\ \varepsilon_{33} \\ 2\varepsilon_{23} \\ 2\varepsilon_{13} \\ 2\varepsilon_{12} \end{Bmatrix} \tag{3.7}$$

where the factors '2' appear so that the 4th, 5th, and 6th components of the strain vector represent conventional shear strains, as well as allowing the following expression to hold true

$$\sigma^{T}\varepsilon = \sigma_{ij}\varepsilon_{ij} \tag{3.8}$$

3.3.2 Generalized Hooke's Law

For a linear elastic material, the components of stress are linear functions of the components of strain and this is expressed through the generalized Hooke's Law defined as

$$\sigma_{ij} = C_{ijkl}\varepsilon_{kl} \tag{3.9}$$

where C_{ijkl} is the stiffness tensor. The inverse of this relation is written as

$$\varepsilon_{kl} = S_{ijkl}\sigma_{ij} \tag{3.10}$$

where S_{ijkl} is the compliance tensor. Matrix representations of Eqs. 3.9 & 3.10 are

$$\sigma = \mathbf{C}\varepsilon \tag{3.11}$$

and

$$\varepsilon = \mathbf{S}\sigma \tag{3.12}$$

where **C** and **S** are the 6x6 stiffness and compliance matrices, respectively.

These matrices each contain 36 coefficients. However, if an elastic potential exists, **C** and **S** are symmetric and therefore the number of independent coefficients for the most general case of anisotropy is reduced to 21 [3.10]. This symmetry would not exist if the column matrix definition of ε did not contain the factors '2'.

3.3.3 Elastic Symmetry

If an anisotropic body possesses elastic symmetry, then **C** can be further simplified. For example, if there exists one plane of elastic symmetry, the number of independent constants in **C** reduces to 13; with three orthogonal planes of elastic symmetry, the number reduces further to 9, as shown in Eq. 3.13. In the latter case, the material would be called orthogonally-anisotropic, or *orthotropic* for short. Complete symmetry, where any plane is a plane of elastic symmetry, results in an *isotropic* body and the number of elastic constants reduces to 2 (Eq. 3.14 with $C_{44} = (C_{11} - C_{12})/2$).

$$\mathbf{C} = \begin{bmatrix} C_{11} & C_{12} & C_{13} & 0 & 0 & 0 \\ C_{12} & C_{22} & C_{23} & 0 & 0 & 0 \\ C_{13} & C_{23} & C_{33} & 0 & 0 & 0 \\ 0 & 0 & 0 & C_{44} & 0 & 0 \\ 0 & 0 & 0 & 0 & C_{55} & 0 \\ 0 & 0 & 0 & 0 & 0 & C_{66} \end{bmatrix} \tag{3.13}$$

3.3.4 Symmetry of Crystals

Lekhnitskii [3.10] refers to F. Neumann who set forth a principle for crystals which established the connection between symmetry of construction and elastic symmetry. According to this principle, a material's physical properties have at least the same kind of symmetry as its crystallographic form.

There exist 32 forms of geometric symmetry of crystals which are divided into 7 crystal systems, e.g. cubic, hexagonal, and tetragonal. For each crystal system, a corresponding set of symmetries applies which simplify **C** in various ways. Materials with a cubic crystal structure, e.g. sodium chloride, magnesium oxide, iron, and silicon, have only 3 independent elastic constants and their stiffness matrix is expressed as

$$\mathbf{C} = \begin{bmatrix} C_{11} & C_{12} & C_{12} & 0 & 0 & 0 \\ C_{12} & C_{11} & C_{12} & 0 & 0 & 0 \\ C_{12} & C_{12} & C_{11} & 0 & 0 & 0 \\ 0 & 0 & 0 & C_{44} & 0 & 0 \\ 0 & 0 & 0 & 0 & C_{44} & 0 \\ 0 & 0 & 0 & 0 & 0 & C_{44} \end{bmatrix} \tag{3.14}$$

in the crystal-fixed frame aligned with (100), (010), and (001).

The values for these coefficients are readily available in the literature for various materials and, for some cases, can be precisely determined to three significant figures. For silicon, they are reported as shown in Table 3.1. The small discrepancy between the two sets of values is a result of improved measuring techniques employed by Pampuch's more recent work [3.18].

Table 3.1 C_{ij} Values Reported for Silicon

C_{ij}	Pampuch [3.18]	Burns [3.4]
C_{11}	165.6 GPa	165.7 GPa
C_{12}	63.8 GPa	63.9 GPa
C_{44}	79.5 GPa	79.6 GPa

The components of the stiffness and compliance matrices, C_{ij} and S_{ij}, are directly related to the structure of crystals; however, their *direct* experimental determination is associated with considerable difficulties. For example, a direct determination of C_{11} for a material of cubic structure requires all strains ε_j but ε_1 to be kept constant since $C_{11} = (\partial\sigma_1/\partial\varepsilon_1)_{\varepsilon_2,\varepsilon_3=\text{const}}$. Readers more familiar with the "technical" or "engineering" material constants such as Young's modulus, E, Poisson's ratio, ν, shear modulus, G, or bulk modulus, K, will note that these constants are readily determinable through simple experiments on materials. E, G, ν, and K are easily related to elastic compliances, S_{ij}, e.g. $E = 1/S_{11}$. Since $\mathbf{C} = \mathbf{S}^{-1}$ (as a result of Eqs. 3.11 and 3.12), C_{ij} are therefore easily determined.

3.3.5 Coordinate Transformation

The stress-strain relation of Eq. 3.11, with **C** given by Eqs. 3.13 or 3.14 holds when the cartesian coordinate axes coincide with the principal directions of the crystal. It is only in the case of an isotropic body that the elastic constants are invariant in any orthogonal coordinate system. In order to express the stress-strain relations in any orthogonal coordinate system we need to make the necessary transformations.

Lekhnitskii [3.10] describes the earlier methods for making such transformations. Here, however, we present the more modern matrix approach of Ting [3.23].

Let the coordinate system x_i represent the crystal-fixed frame for which Eqs. 3.11 and 3.12 hold. In the new coordinate system x^*_i, where

$$x_i^* = a_{ij} x_j \tag{3.15}$$

we have

$$\sigma^* = \mathbf{C}^* \varepsilon^* \tag{3.16}$$

and

$$\varepsilon^* = \mathbf{S}^* \sigma^* \tag{3.17}$$

We can relate σ^* with σ as follows

$$\sigma^* = \mathbf{Q} \sigma \tag{3.18}$$

where **Q** is the 6x6 transformation matrix given by

$$\mathbf{Q} = \begin{bmatrix} \mathbf{K} & 2\mathbf{M} \\ \mathbf{N} & \mathbf{L} \end{bmatrix} \tag{3.19}$$

and **K**, **M**, **N**, and **L** are 3x3 submatrices defined in terms of a_{ij}

$$\mathbf{K} = \begin{bmatrix} a_{11}^2 & a_{12}^2 & a_{13}^2 \\ a_{21}^2 & a_{22}^2 & a_{23}^2 \\ a_{31}^2 & a_{32}^2 & a_{33}^2 \end{bmatrix} \tag{3.20}$$

$$\mathbf{M} = \begin{bmatrix} a_{12}a_{13} & a_{13}a_{11} & a_{11}a_{12} \\ a_{22}a_{23} & a_{23}a_{21} & a_{21}a_{22} \\ a_{32}a_{33} & a_{33}a_{31} & a_{31}a_{32} \end{bmatrix} \tag{3.21}$$

$$\mathbf{N} = \begin{bmatrix} a_{21}a_{31} & a_{22}a_{32} & a_{23}a_{33} \\ a_{31}a_{11} & a_{32}a_{12} & a_{33}a_{13} \\ a_{11}a_{21} & a_{12}a_{22} & a_{13}a_{23} \end{bmatrix} \tag{3.22}$$

$$\mathbf{L} = \begin{bmatrix} a_{22}a_{33} + a_{23}a_{32} & a_{23}a_{31} + a_{21}a_{33} & a_{21}a_{32} + a_{22}a_{31} \\ a_{32}a_{13} + a_{33}a_{12} & a_{33}a_{11} + a_{31}a_{13} & a_{31}a_{12} + a_{32}a_{11} \\ a_{12}a_{23} + a_{13}a_{22} & a_{13}a_{21} + a_{11}a_{23} & a_{11}a_{22} + a_{12}a_{21} \end{bmatrix} \tag{3.23}$$

The matrix **Q** cannot be used directly for the strain transformations as in Eq. 3.18 because of the presence of the factors '2' in the definition of ε. Instead we define $\varepsilon' = [\varepsilon_{11}, \varepsilon_{22}, \varepsilon_{33}, \varepsilon_{23}, \varepsilon_{31}, \varepsilon_{12}]^{\mathrm{T}}$, and write

$$\varepsilon = \mathbf{R}\varepsilon' \tag{3.24}$$

where **R** is the 6x6 matrix given by

$$\mathbf{R} = \begin{bmatrix} \mathbf{I} & 0 \\ 0 & 2\mathbf{I} \end{bmatrix} \tag{3.25}$$

where **I** is the 3x3 identity matrix. **Q** can now be used to relate ε'^{*} and ε' as follows

$$\varepsilon'^{*} = \mathbf{Q}\varepsilon' \tag{3.26}$$

Using Eqs. 3.24, 3.26, and the inverse of Eq. 3.24, respectively, we can write the following series of expressions relating ε^{*} to ε

$$\varepsilon^{*} = \mathbf{R}\varepsilon'^{*} = \mathbf{R}\mathbf{Q}\varepsilon' = \left(\mathbf{R}\mathbf{Q}\mathbf{R}^{-1}\right)\varepsilon \tag{3.27}$$

A simple expansion will show that $\left(\mathbf{R}\mathbf{Q}\mathbf{R}^{-1}\right) = \left(\mathbf{Q}^{-1}\right)^{\mathrm{T}}$. Hence Eq. 3.27 simplifies to

$$\varepsilon^{*} = \left(\mathbf{Q}^{-1}\right)^{\mathrm{T}}\varepsilon \tag{3.28}$$

or the inverse, expressed as

$$\varepsilon = (\mathbf{Q})^{\mathrm{T}}\varepsilon^{*} \tag{3.29}$$

Finally, we can derive the expression relating $\mathbf{C}^{*}$ to $\mathbf{C}$. Using Eqs. 3.24, 3.26, and the inverse of Eq. 3.24, respectively, we can write the following series of expressions relating σ^{*} and ε^{*}

$$\sigma^* = \mathbf{Q}\sigma = \mathbf{Q}\mathbf{C}\varepsilon = \left(\mathbf{Q}\mathbf{C}\mathbf{Q}^T\right)\varepsilon^* = \mathbf{C}^*\varepsilon^* \tag{3.30}$$

and therefore

$$\mathbf{C}^* = \mathbf{Q}\mathbf{C}\mathbf{Q}^T \tag{3.31}$$

We can similarly derive an expression relating $\mathbf{S}^*$ to $\mathbf{S}$. This is shown below in two alternative forms

$$\mathbf{S}^* = \left(\mathbf{Q}^{-1}\right)^T \mathbf{S}\mathbf{Q}^{-1} \tag{3.32}$$

or

$$\left(\mathbf{R}^{-1}\mathbf{S}^*\mathbf{R}^{-1}\right) = \mathbf{Q}\left(\mathbf{R}^{-1}\mathbf{S}\mathbf{R}^{-1}\right)\mathbf{Q}^T \tag{3.33}$$

Thus for any orientation of the crystal, we can define coefficients a_{ij} through the coordinate transformation defined in Eq. 3.15. Then **Q** is defined using Eqs. 3.19–3.23 and used in Eq. 3.31 to define the transformed stiffness matrix, $\mathbf{C}^*$, in terms of the crystal-fixed stiffness matrix, **C**, as defined in Eq. 3.14 for silicon. If the compliance matrix, **S**, is known, Eq. 3.32 can be used to determine $\mathbf{S}^*$.

3.4 CURRENT APPROACHES TO MODELING MEMS MATERIALS AND STRUCTURES

In all known theoretical studies on the modeling and analysis of MEMS which precede this dissertation (e.g. Pourahmadi et al. [3.20], Mullen et al. [3.13]), classical theories of engineering mechanics and structures based on assumptions of homogeneity and isotropy are employed. This is true from the simplest cases, where classical Euler-Bernoulli beam theory and Timoshenko's membrane theory are employed, to the application of more elaborate structural theories, e.g. to account for stiffness non-linearities in vibrating beams and the use of Duffing's equation [3.21], large deflection theories for beams [3.2], and residual stresses in membranes [3.12].

Furthermore, although "numerical modeling of the mechanical behavior of sensors and microstructures has gradually been developed as an integral part of the microsensor design process" [3.20], the underlying material property assumptions are still those of homogeneity. It appears, therefore, that increasingly advanced analytical and numerical structural analysis techniques are being employed in achieving improved models of MEMS, without a proportionate effort at improving material models.

Many leaders in the field of MEMS have long recognized the need for improved material models. For example, Senturia [3.22] has stated that "for many of the materials used in microfabricated structures, basic data on mechanical properties and their control through process variables is lacking." Yet he goes on to add that "in addition to the normal mechanical properties of the materials, such as Young's modulus and Poisson's ratio, the designer must be able to predict residual stresses." By referring to a unique "Young's modulus" and a "Poisson's ratio" for a material, Senturia is assuming the material to be both homogeneous and isotropic, before the "basic data" is even examined. Clearly the problems associated with material inhomogeneities and anisotropies are not recognized. This is generally evident in the MEMS field by the lack of attention paid to the modelling of material inhomogeneities and anisotropies.

As is clear from §3.2, isotropy and homogeneity cannot generally be assumed for materials such as polysilicon. For cases where these assumptions are inappropriate, no level of sophisticated structural analysis can closely and consistently predict the mechanical behavior of these structures. Furthermore, the inclusion of better material models may preclude direct application of classical theories for structural elements (such as beam theory, standard plate bending theory, etc.), thus necessitating the development of novel ways to evaluate the structural responses of MEMS. Finally, the variability inherent in the microstructure, may require a probabilistic description of the material behavior and structural response evaluation aimed at assessing the performance reliability of MEMS.

3.5 OVERVIEW OF IMPROVED MODELING APPROACHES

Modelling approaches are needed that can overcome the shortcomings of current approaches which tend to neglect anisotropy and inhomogeneity as well as associated uncertainties in structural response. Generally speaking, these approaches can be grouped in two categories: (i) ones which address the anisotropies for homogeneous cases—these generally tend not to require probabilistic descriptions; and (ii) where inhomogeneities are incorporated into the material models—these cases generally tend to require a probabilistic description. Particular cases of approaches (i) and (ii) are developed in subsequent chapters, however, an review of many of the various possible approaches is desirable. An overveiw is presented here, serving the dual purpose of highlighting the reasons for the choice of each particular approach in Chapters 4, 5, and 6, and outlining a spectrum of alternative approaches that future work in the area can focus upon.

The use of effective properties results in acceptable results for heterogeneous materials for which the microstructure is very fine in comparison with the dimensions of the engineering structural elements. Evaluation of "effective properties" of heterogeneous materials has been extensively covered in the classical literature. Chapter 4 concentrates on homogenization of material properties and is valid for the correct modelling of fine-grained polysilicon thin films.

The modelling of materials which takes into account inhomogeneities and the associated uncertainties, however, is not so straight forward. Directly applicable approaches do not exist in the literature. However, a number of approaches developed for problems in other fields may be adapted for use in the field of MEMS.

It is useful to look at possible components of the modeling that may be necessary for taking into account material inhomogeneities and the associated uncertainties in MEMS mechanical response. Fig. 3.4 outlines a possible modelling approach and indicates how each component could contribute to the final structural model. A distinct division is shown between experimental and theoretical work. In this study, models shown in gray are the main area of focus in modelling inhomogeneous MEMS structural components and complete structures.

A number of promising models which may be adapted for successful application in the area of MEMS include: (i) probabilistic mechanics of discrete media [3.5]; (ii) random field models based on geometric networks [3.14]; (iii) grain-growth models developed in the field of computational materials science; (iv) Torquato's "unified methodology" [3.24]; (v) models based on atomistic simulation [3.1]; and (vi) the emerging field of nanomechanics.

Haddad [3.5], presents a "new" micromechanical approach which, in this context, would model the material as a two-dimensional, randomly arranged layer of elastic-plastic crystals that are bonded together at crystal boundaries. He uses random variables and functions of random variables to characterize the physical and geometric properties of the microstructure.

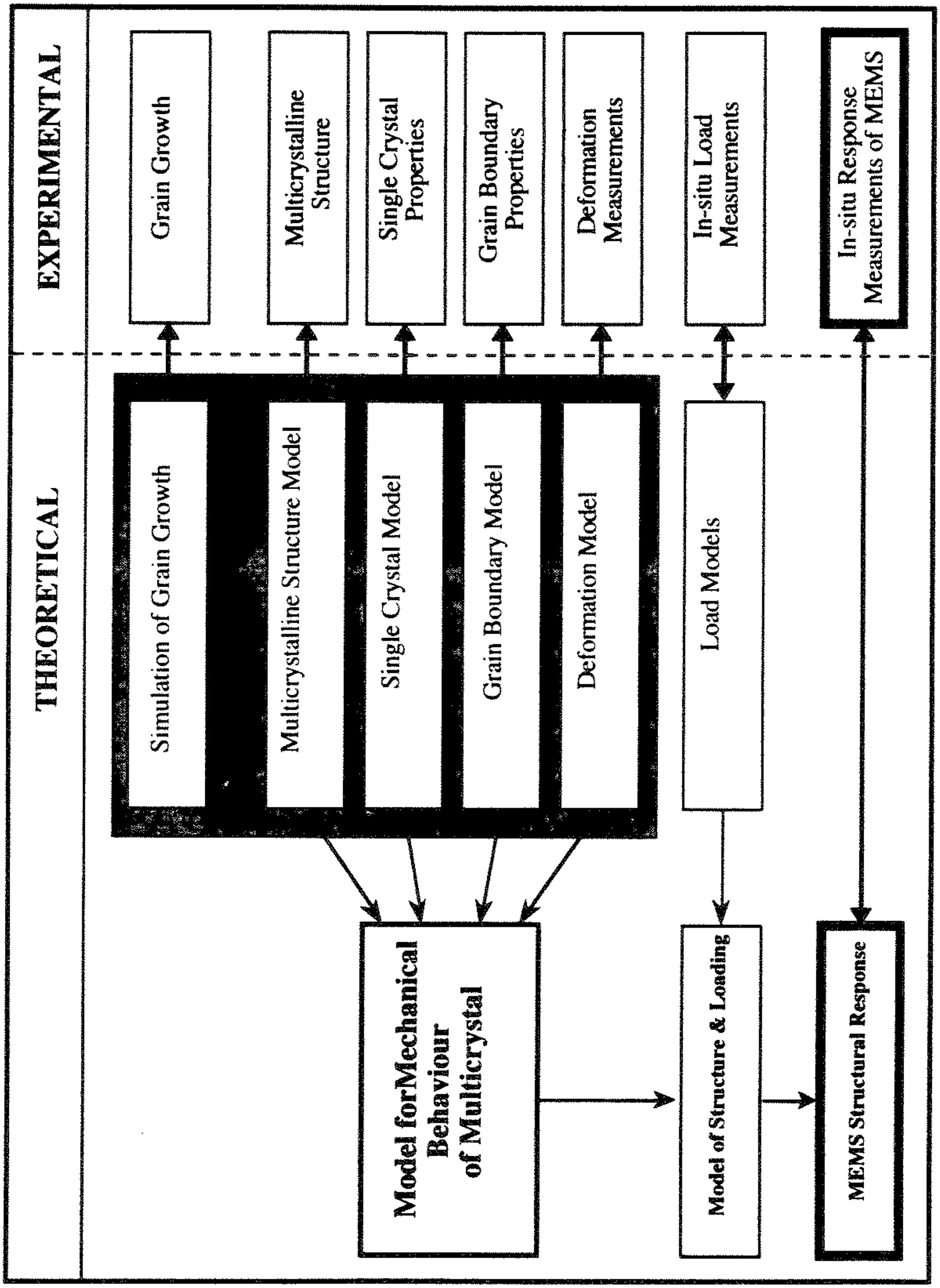

Fig. 3.4 Modeling Approach for Heterogeneous MEMS

Approaches similar to the work presented by Ostoja-Starzewski et al. [3.14, 3.15, 3.16, 3.17] are also applicable for solving inhomogeneous problems in MEMS. Ostoja-Starzewski has established a framework for (i) determining linear elastic random field characteristics of planar Delaunay Networks (which can be thought of as a truss system where each truss member represents the contact between adjacent granular particles); (ii) establishing bounds on effective properties of such networks; and (iii) determination of scaling parameters for use in finite element approximations.

The field of computational material science has advanced to a point where today it is possible to make micro-scale evaluations of material behavior. Applications range from detailed granular modelling of portland cement to the texture development models in metallurgy. These tools can be used to generate MEMS material microstructures and serve as numerical experiments validating some of the simpler models that will be developed such as simulation of crystal grain geometries. Additionally, these tools enable the numerical evaluation of many material properties, including mechanical and electrical properties and are becoming invaluable in designing materials with improved performance levels.

Recent research in the area of atomistic simulation of material microstructure has advanced to a level that can be useful for certain MEMS applications. Currently, for example, knowledge about grain boundaries and their mechanical properties is limited. Atomistic simulation provides a framework for the prediction of grain boundary properties [3.1]. This area stretches the physical study of materials down to the nanometer scale. The new field of nanomechanics also offers opportunities for improved modelling of the grain boundary phase. Indeed, as the dimensions of MEMS structures are reduced and finer grained materials are employed, these effects gain increasing importance and a better understanding can only be attained by employing the findings in the field of nanomechanics.

On a more practical level, Krulevitch et al. [3.9] and Huang et al. [3.6] have studied the texture-stress relationship in doped and undoped polysilicon films, showing a direct correlation between certain textures and states of residual stress in the films. Krulevitch et al. [3.8] have also shown how grain sizes are dependent on process conditions. This knowledge is invaluable in modelling the shapes and sizes of crystallites in polysilicon as well as for realistic modelling of residual stresses (see §3.5).

3.6 SUMMARY

This chapter considered approaches to the modeling of MEMS materials and structures. The emphasis being on polycrystalline silicon thin film applications, the structure and properties of single-crystal silicon were first reviewed, followed by a description of the polycrystalline state. A review of existing methodologies for analyzing MEMS structures reveals that although sophisticated structural analysis techniques are often employed, isotropy and homogeneity are both assumed for the material properties. In view of the properties of the polycrystalline state, it is clear that these assumptions can only hold for untextured fine-grained polysilicon. Modelling approaches are therefore sought for cases where this assumption does not hold.

For the case of fine-grained samples—the "polycrystalline" case—the existence of preferred orientations as a result of the specific processing conditions (e.g. LPCVD technique, doping, annealing) results in anisotropic bulk properties. Although homogeneity can be assumed, appropriate anisotropic elastic properties need to be determined. Appropriate homogenization approaches for the above determination are presented in Chapter 4. These employ the single-crystal elastic stress-strain and coordinate transformation relations developed in this chapter.

For coarse-grained samples—the "multicrystalline" case—the heterogeneity is such that a representative volume element does not exist, i.e. statistical averaging cannot be performed, and therefore homogeneity cannot be assumed. This requires the development of models that take into account the heterogeneities. Additionally, these heterogeneities introduce uncertainties in the behavior of the material which need to be taken into account in a probabilistic manner.

Approaches to modelling inhomogeneities abound in the literature and can be found in the areas of computational materials science, rock mechanics, metallurgy, etc. Approaches based on simulation of grains appear to be the most appropriate in capturing the inhomogeneities and taking into account the probabilistic nature of the problem. A model for generating random grain arrangements in space is chosen for a simulation model and developments on this are presented in Chapter 5. Again, these models rely on the basic single-crystal stress-strain and coordinate transformation relations presented in this chapter. A more efficient probabilistic approach using random fields is presented in Chapter 6.

CHAPTER 3 REFERENCES

[3.1] Alber, I., J. L. Bassani, M. Khantha, V. Vitek, and G. J. Wang, "Grain Boundaries as Heterogeneous Systems—Atomic and Continuum Elastic Properties," *Philosophical Transactions of the Royal Society of London, Series A, Physical Sciences and Engineering,* Vol. 339, No. 1655, pp. 555–586, 1992.

[3.2] Brennen, R. A., M. G. Lim, A. P. Pisano, and A. T. Chou, "Large Displacement Linear Actuator," *ASME Winter Annual Meeting,* New Orleans, LA, November 1993.

[3.3] Bunge, H. J., "The Basic Concepts of Texture Investigation in Polycrystalline Materials," *Steel Research,* Vol. 62, No. 12, pp. 530–541, 1991.

[3.4] Burns, D. W., *Micromechanics of Integrated Sensors and the Planar Processed Pressure Transducer (Chapter III),* Doctoral Dissertation, University of Wisconsin, Madison WI, 1988.

[3.5] Haddad, Y. M., "A Microstructural Approach to the Mechanical Response of a Class of Polycrystalline Systems 1. Theoretical Analysis," *Res Mechanica,* Vol. 29, No. 2, pp. 177–196, 1990.

[3.6] Huang, J., P. Krulevitch, G. C. Johnson, R. T. Howe, and H. R. Wenk, "Investigation of Texture and Stress in Undoped Polysilicon Films," Materials Research Society Symposium, Proceedings, Vol. 182, pp. 201–206, 1990.

[3.7] Kamins, T. I., *Polycrystalline Silicon for Integrated Circuit Applications,* Kluwer Academic, Boston, 1988.

[3.8] Krulevitch, P.A., *Micromechanical Investigations of Silicon and Ni-Ti-Cu Thin Films,* Ph.D. Dissertation, University of California at Berkeley, 1994.

[3.9] Krulevitch, P., G.C. Johnson, and R.T. Howe, "Stress and Microstructure in Phosphorus Doped Polycrystalline Silicon," *Mat. Res. Soc. Symp. Proc.,* Vol. 276 (1992) p. 79.

[3.10] Lekhnitskii, S. G., *Theory of Elasticity of an Anisotropic Elastic Body,* [Edited by J. J. Brandstatter, Translated by P. Fern] Holden-Day, San Francisco, 1963.

[3.11] Lubliner, J., *Plasticity Theory,* Macmillan Publishing Company, New York, 1990.

[3.12] Mehregany, M., M. G. Allen, and S. D. Senturia, *IEEE Solid-State Sensors Workshop,* Hilton Head, S. C., June 1986.

[3.13] Mullen, R.L. M. Mehregany, M. P. Omar, and W. H. Ko, "Theoretical modeling of boundary conditions in microfabricated beams," *Proceedings. IEEE Micro Electro Mechanical Systems: An Investigation of Micro Structures, Sensors, Actuators, Machines and Robots,* Nara, Japan, pp. 154–159, 30 January–2 February, 1991.

[3.14] Ostojastarzewski, M. and C. Wang, "Linear Elasticity of Planar Delaunay Networks—Random Field Characterization of Effective Moduli," *Acta Mechanica,* Vol. 80, No. 1-2, pp. 61–80, 1989.

[3.15] Ostojastarzewski, M. "Bounds on Constitutive Response for a Class of Random Material Microstructures," *Computers & Structures,* Vol. 37, No. 2, pp. 163–167, 1990.

[3.16] Ostojastarzewski, M. and C. Wang, "Linear Elasticity of Planar Delaunay Networks 2. Voigt and Reuss bounds, and Modification for Centroids," *Acta Mechanica,* Vol. 84, No. 1-4, pp. 47–61, 1990.

[3.17] Ostojastarzewski, M., P. Y. Sheng, and I. JASIUK, "Influence of Random Geometry on Effective Properties and Damage Formation in Composite Materials," *Journal of Engineering Materials and Technology—Transactions of the ASME,* Vol. 116, No. 3, pp. 384–391, 1994.

[3.18] Pampuch, R., *Constitution and Properties of Ceramic Materials,* Materials Science Monographs, 58, Elsevier Science Pub. Co., Inc., New York, 1991.

[3.19] Pospiech, J., K. Sztwiertnia, and F. Haessner, "The Misorientation Distribution Function," *Textures and Microstructures,* Vol. 6, pp. 201–215, 1986.

[3.20] Pourahmadi, F. and J. W. Twerdok, "Modeling Micromachined Sensors with Finite Elements," *Machine Design,*Vol. 62, No. 15, pp. 44–60, 1990.

[3.21] Pratt, R. I., G. C. Johnson, R. T. Howe, and J. C. Chang, "Micromechanical Structures for Thin Film Characterization," *IEEE Transducers '91*, pp. 205–208.

[3.22] Senturia, S.D., "Can we Design Microrobotic Devices without knowing the Mechanical Properties of Materials?," *Proceedings of the IEEE Micro Robots and Teleoperators Workshop. An Investigation of Micromechanical Structures, Actuators and Sensors*, Hyannis, MA, USA, 9-11 November 1987.

[3.23] Ting, T. C. T., "Invariants of Anisotropic Elastic Constants," *Quarterly Journal of Mechanics and Applied Mathematics*, Vol. 40, No. 3, 1987.

[3.24] Torquato, S., "Unified Methodology to Quantify the Morphology and Properties of Inhomogeneous Media," (Third International Conference on Electrical Transport and Optical Properties in Inhomogeneous Media, Guanajuato, Mexico, 9-13 Aug. 1993), *Physica A*, Vol. 207, No. 1–3, pp. 79–91, 1994.

[3.25] Wenk, H. R., M. Sintubin, G. C. Johnson, and R. T. Howe, "Texture Analysis of Polycrystalline Silicon Films," *Journal of Applied Physics*, Vol. 67, No. 1, pp. 572–574, 1990.

Chapter 4

HOMOGENIZATION OF MATERIAL PROPERTIES

4.1 INTRODUCTION

A monophase polycrystalline material is an aggregate of crystal grains, with individual grains distinguished from adjacent neighbors according to their distinct crystallographic orientations with respect to a global-fixed frame. Separating neighboring grains, there exists a grain boundary region, usually on the order of a few inter-atomic spacings, the properties of which may be different from the crystalline state. The crystalline state has anisotropic material properties and individual crystal grains are generally differently oriented, thus resulting in a variation of material properties from point to point within a sample. This variation is generally random in nature and its characteristics are related to the processing conditions for the polycrystal (see §3.2.1).

Despite these heterogeneities in polycrystals, the bulk material, e.g. a 1 cm^3 sample consisting of approximately 10^{12} crystals, may be more conveniently treated as a homogeneous continuum at the macro scale. This is achieved by evaluating approximate "effective" properties—usually refered to as "homogenization." With this approach, the detailed micro-scale variations of displacement, stress, and strain fields are not identified.

Homogenization methods, however, are not generally applicable to all MEMS materials. As pointed out in Chapter 3, the assumption for the validity of homogenization may not hold true for some classes of MEMS structures and their constituent materials. These are structures where the microstructural scales, e.g. grain sizes, are of the same order of magnitude as the smallest structural dimensions, e.g. beam depth, thus violating the existence of a representative volume element assumption of homogenization (see §4.2.1). Nevertheless, these techniques are both applicable and desirable in correctly predicting the mechanical behavior of components made up of fine-grained, textured thin films. Homogeneity being valid in these cases, however, still does not allow the blind application of classical structural theories, many of which assume isotropic material behavior. The texture present in many thin films (§2.4) results in anisotropic bulk properties that need to be incorporated in the mechanical models. The methods introduced in this chapter address this need where the homogenized material properties of interest are the elastic moduli.

4.2 HOMOGENIZATION APPROACHES

4.2.1 Basic Concepts

Homogenization of elastic moduli for a heterogeneous material involves finding a homogeneous material that performs similarly to the heterogeneous material subjected to any macro-scale stress or strain field. This may be achieved by ensuring identical energies in the two systems.

If all details of the distribution of the material properties, e.g. the elastic moduli, over a sample of a random elastic medium were known, it would be possible, in principle, to precisely predict the effective elastic moduli. However, such exact, detailed sample information is rarely available, nor is it very desirable when the ultimate aim is to predict the expected behavior of a sample randomly chosen from a set of similarly processed samples. For this, statistical information is needed for predicting the expected effective elastic moduli (EEEM) of the sample. EEEM is defined as the expected value of the homogenized elastic modulus.

With complete statistical information regarding the details of the spatial variations of the microstructure, it is in principle possible to predict exact expected values for the effective elastic moduli[†] . The statistical information, however, is rarely complete and therefore does not allow an exact derivation of the expected effective values. With partial statistical information, it is only possible to determine bounds on the EEEM [4.14].

The most commonly employed statistical information in this context is obtained through texture analysis (§3.2.2) and is normally given as the orientation distribution function (ODF) for the polycrystalline samples [4.2]. Employing appropriate forms of variational principles, bounds are derived on the EEEM using the incomplete statistical information. The principles of minimum potential energy and minimum complementary energy are the most commonly used variational principles. The resulting bounds become narrower when additional statistical information regarding the spatial distribution of the material microstructure is employed, or when assumptions are made regarding the mathematical form of higher-order correlation functions. This issue is further discussed in the following subsection.

Central to all homogenization concepts is the requirement for the existence of a representative volume element (RVE)—a region small enough

---

[†] Even when complete statistical information is available, for general non-linear forms of expectation, extensive integrations would be required, thus rendering the problem practically unfeasible.

with respect to specimen dimensions to approach an infinitesimal cube in continuum assumptions, while at the same time containing a sufficient number of crystal grains so that it is statistically representative of the body as a whole. When this criterion is met, the material properties may be homogenized by finding the mean values of the required parameters. This is valid since, according to the law of large numbers, the coefficients of variation of the effective moduli are negligibly small when the RVE contains a large number of grains, i.e. the problem is then quasi-deterministic.

In the above approaches, the contribution of the grain boundary region (GBR) to the effective bulk properties is neglected. For grain sizes that are orders of magnitude larger than interatomic spacings, this is generally a valid assumption. However, the GBR properties need to be incorporated in the evaluation of the effective properties for cases where the GBR represents a significant volume fraction of the sample, or when the GBR properties are significantly different than the bulk crystal properties.

4.2.2 Microstructural Statistics

A convenient way of representing the statistical variations in the material microstructure is through n-point probability densities of the material parameters, e.g. the elastic moduli, or the crystal orientations [4.14]. The one-point probability density $p_1(c)$, $c = c(\mathbf{x})$ is defined such that $p_1(c)dc$ is the probability to find at point $\mathbf{x}$ the parameter in the range $[c\ , c + dc]$. The two-point probability density $p_2(c_1,c_2)$ is defined such that $p_2(c_1,c_2)dc_1dc_2$ is the probability to find at point $\mathbf{x}_1$ a parameter c_1 in the range $[c_1,\ c_1 + dc_1]$ *and* at point $\mathbf{x}_2$ a parameter c_2 in the range $[c_2,\ c_2 + dc_2]$. Probability densities of higher order are defined in a similar fashion. One should note that lower order probability densities are derivable from higher order densities by integrating out the higher order components, e.g. $p_1 = \int p_2 dc_2$.

Ensemble averages, or expected values are computed by performing the familiar integral

$$\mathrm{E}\left[c_1\right] = \langle c_1 \rangle = \int c_1 p_1(c_1) dc_1 \tag{4.1}$$

where the $\langle \cdot \rangle$ notation, common in the homogenization literature, is introduced. This is generalized to two or more points as shown below:

$$\begin{aligned} \langle c_1 c_2 \rangle &= \iint c_1 c_2 p_2(c_1, c_2) dc_1 dc_2 \\ \langle c_1 c_2 c_3 \rangle &= \iiint c_1 c_2 c_3 p_3(c_1, c_2, c_3) dc_1 dc_2 dc_3 \\ &\vdots \\ \langle c_1 c_2 c_3 \cdots c_n \rangle &= \iiint \cdots \int c_1 c_2 c_3 \cdots c_n p_n(c_1, c_2, c_3, \cdots, c_n) dc_1 dc_2 dc_3 \cdots dc_n \end{aligned} \tag{4.2}$$

For $n>1$, these averages are called n-point correlation functions.

These n-point correlation functions have direct physical meanings. As an example, consider a polycrystalline sample, shown in Fig. 4.1, with crystal grains that are elongated in the x_2 axis direction. Assume crystal properties are mutually statistically independent. Taking two points, "1" and "2" that lie on a line perpendicular to the x_2 axis with a separation smaller than the mean grain length in the x_2 direction, we can see that $\langle c_1 c_2 \rangle$ is almost equal to $\langle c_1 \rangle^2$ since the probability that the two points fall in the same grain is close to zero. Rotating by 90°, the same two points result in a value very close to $\langle c_1^2 \rangle$ for $\langle c_1 c_2 \rangle$ since the probability that the two points fall in the same grain is close to 1. Thus, $\langle c_1 c_2 \rangle$ reflects the geometric anisotropy of grains. Similarly, higher order correlation functions represent information regarding grain shapes $(n = 3)$, boundary curvatures $(n = 4)$, etc. [4.14].

The n-point correlation functions can completely describe the statistical properties of polycrystals. There are, however, other forms of higher order

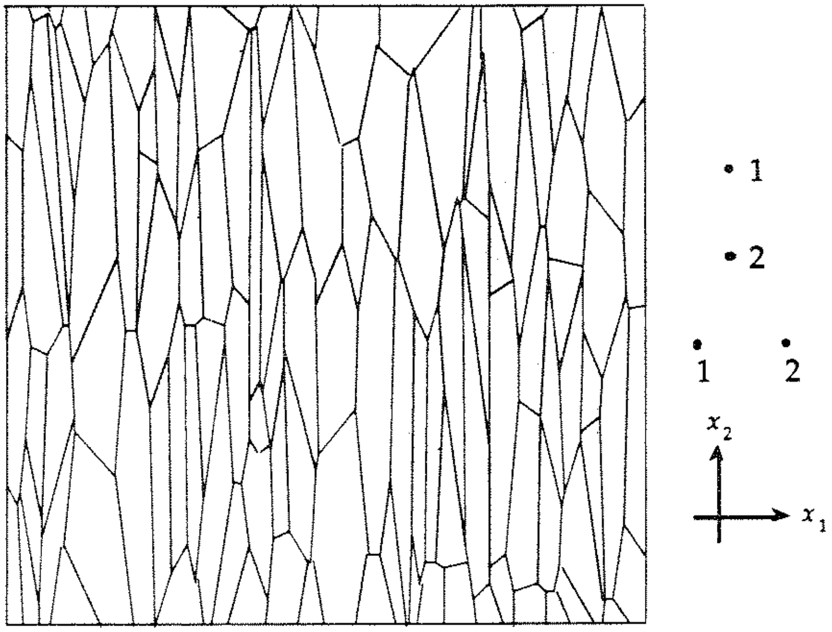

Fig. 4.1 Cross-Section of Polycrystal with Elongated Grains

statistical descriptors of the material microstructure. One that is often used is the misorientation distribution function (MDF), developed by Pospiech et al. [4.18], which describes the distribution of orientation differences between adjacent crystals. Since the properties of grain boundaries are dependent on the misorientation of adjacent grains (see §3.2.1), the MDF is most useful in describing the grain boundary properties in a polycrystal [4.6]. The MDF can be related to the 2-point correlation function using relationships developed by Morawiec and Pospiech [4.16].

Finally, it should be clear that we are still estimating expected values. Therefore the use of *n*th-order statistical information should not be confused with efforts at estimating the uncertainty in the effective elastic moduli. The problem here is essentially treated deterministically since the RVEs involved contain, by definition, very large numbers of grains. The problems of uncertainly arise in cases where small numbers of grains are involved and homogenization cannot be employed (see Chapter 5).

4.2.3 Bounding Techniques

Without any statistical information about the polycrystalline material microstructure, only the crystal-fixed stiffness or compliance properties are known. Taking the minimum and maximum values among all possible orientations for the different elastic moduli, the so called 0th order bounds ($C^{(-0)}$ and $C^{(+0)}$) are obtained. These bounds, however, tend to be very wide even for moderately anisotropic materials and have limited use in homogenization. Bounds that are acceptably close are obtained using statistical information regarding the microstructure.

As early as 1889, Voigt [4.21] studied the problem of calculating the effective 4th rank stiffness tensor of elasticity of a polycrystalline aggregate, C^{eff}, from the corresponding tensor of the constituent crystallites. Voigt's proposal was to use the crystal orientational average (1st-order statistic) as an approximation, C^{V}, to C^{eff}. Reuss [4.19] used the inverse of Voigt's approach in 1929, averaging the compliance tensor, the inverse of which, C^{R}, is the Reuss approximation. In 1952, using two basic variational principles of elasticity theory, Hill [4.9] proved that the Voigt and Reuss averages are upper and lower bounds for the true effective stiffness tensor such that the following relation always holds for elastic moduli derived from C^{R} and C^{V}, e.g. the shear modulus G:

$$G^{R} \leq G^{eff} \leq G^{V} \tag{4.3}$$

As shown later, bounds based on C^{V} and C^{R} are much narrower than those based on $C^{(-0)}$ and $C^{(+0)}$. Bounds based on C^{V} and C^{R} have also been referred to as 1st-order bounds since they use the 1-point statistical information previously discussed and are therefore also denoted as $C^{(+1)}$ and $C^{(-1)}$, respectively. Higher-order bounds, based on $C^{(\pm n)}$, $n \geq 2$, use additional statistical information and, as pointed out earlier, can reflect some of the geometrical aspects of the microstructure.

The use of higher-order statistical information results in successively closer bounds on effective elastic moduli, e.g. G^{eff}, such that

$$G^{(-0)} \leq G^{(-1)} \leq G^{(-2)} \leq \ldots \leq G^{eff} \leq \ldots \leq G^{(+2)} \leq G^{(+1)} \leq G^{(+0)} \tag{4.4}$$

The bounds of Voigt and Reuss (VRH bounds) are the best possible if only volume fraction information (i.e. 1st-order statistics) regarding the various orientations are known for the polycrystal. As an example, VRH bounds are now calculated for the averaged elastic moduli of textured polycrystals with cubic crystal symmetry, as is the case for silicon.

The Voigt approximation takes the texture-weighted orientational average of the stiffness matrix, with components expressed in a crystal-fixed frame, and is symbolically expressed as

$$\mathbf{C}^{V} = \langle \mathbf{C} \rangle = \frac{1}{8\pi^2} \int_0^{2\pi} \int_0^{2\pi} \int_0^{\pi} \Pi(\mathbf{C}) f(\theta, \psi, \phi) \sin(\phi) d\theta d\psi d\phi \tag{4.5}$$

where f(.) is the orientation distribution function (ODF), θ, ψ, ϕ are the Euler angles [4.3], and $\Pi(.)$, introduced by Ferrari [4.4], is the frame-change operator defined in terms of sines and cosines of the Euler angles. This yields a rigorous upper bound on the effective polycrystalline elastic moduli. Averaging of the crystal compliance matrix, $\mathbf{S} = \mathbf{C}^{-1}$, performed via Eq. 4.5, yields a rigorous lower bound (the Reuss bound) on the effective polycrystal elastic moduli. The arithmetic average of the bounds is called Hill's estimate [4.9].

Noted examples of higher-order bounds include those by Hashin and Shtrikman [4.8] (2nd-order bounds) as well as the self-consistent estimates [4.14]. It will be shown later, however, that for the homogenization of polycrystalline silicon, the Voigt and Reuss bounds are sufficiently narrow and the Hill estimate is very close to the value to which higher-order bounds converge. The more costly higher-order bounds are therefore not used here. The interested reader is referred to comprehensive reviews of these methods by Hirsekorn [4.10] and by Kröner [4.14].

An example cited by Kröner is now outlined which elegantly illustrates the concepts of converging higher-order bounds. This example also shows how the Voigt and Reuss bounds for polycrystalline silicon compare to the higher-order bounds. For a perfectly disordered (and thus with a fully assigned set of statistical properties) macroisotropic aggregates of cubic crystallites the expected effective shear modulus, $G = G^{eff}$, is shown to be the solution to the following cubic equation:

$$G^3 + (\alpha_1 - \alpha_2)G^2 + (\beta_1 - \beta_2)G - \gamma = 0 \tag{4.6}$$

where

$$\begin{aligned} \alpha_1 &= \tfrac{3}{40}(8\mu + 12\nu + 15\kappa) \\ \alpha_2 &= \tfrac{1}{5}(3\mu + 2\nu) \\ \beta_1 &= \tfrac{3}{20}\kappa(2\mu + 3\nu) \\ \beta_2 &= \tfrac{3}{40}(6\kappa\nu + 9\kappa\mu + 20\mu\nu) \\ \gamma &= \tfrac{3}{4}\kappa\mu\nu \end{aligned} \tag{4.7}$$

and

$$\begin{aligned} \kappa &= \tfrac{1}{3}(C_{11} + 2C_{12}) \\ \mu &= C_{44} \\ \nu &= \tfrac{1}{2}(C_{11} - C_{12}) \end{aligned} \tag{4.8}$$

where C_{ij} are the stiffness coefficients for the cubic crystalline material, as defined in §3.3.4. Since full statistical information is available (assumed in this case) the exact value of G can be found by solving the cubic equation. Note that for this material, the bulk modulus, κ, is precisely known regardless of the order of bounds (i.e. bounds on κ coincide for all orders ≥ 1). Equation (4.6) is equivalent to

$$G = \frac{\alpha_2 G^2 + \beta_2 G + \gamma}{G^2 + \alpha_1 G + \beta_1} \tag{4.9}$$

which forms the basis for an iterative solution to G as shown below:

$$G^{(i+2)} = \frac{\alpha_2 (G^{(i)})^2 + \beta_2 G^{(i)} + \gamma}{(G^{(i)})^2 + \alpha_1 G^{(i)} + \beta_1} \tag{4.10}$$

Kröner [4.14] has shown that by using ith-order bounds in the right-hand side, the left-hand side would yield (i+2)th-order bounds on G. Starting with the following values for the initial solutions of $G^{(\pm 0)}$ and $G^{(\pm 1)}$, all other solutions, $G^{(\pm n)}$, can be found:

$$\begin{aligned} G^{(+0)} &= G^{(\max)} = C_{44} \\ G^{(-0)} &= G^{(\min)} = \tfrac{1}{2}(C_{11} - C_{12}) \\ G^{(+1)} &= G^{V} = \alpha_2 \\ G^{(-1)} &= G^{R} = \gamma/\beta_1 \end{aligned} \tag{4.11}$$

Since this is a macroisotropic material, only two independent constants define the effective elastic properties. Often, the Young's modulus and Poisson's ratio, ν, are chosen. Here we will use G and E. Use can be made of the following relations

$$\begin{aligned} G &= \frac{E}{2(1+\nu)} \\ \kappa &= \frac{E}{3(1-2\nu)} \end{aligned} \tag{4.12}$$

to express E in terms of G and κ as shown below

$$E = \frac{9\kappa}{3\left(\kappa/G\right)+1} \tag{4.13}$$

By substituting values for $G^{(\pm n)}$ and κ in this expression, bounds on E, expressed as $E^{(\pm n)}$, are also found for $n \geq 1$. The 0th-order bounds on E cannot be obtained using Eq. 4.13 since the notion of macroisotropy does not hold in the derivation of these bounds. $E^{(\pm 0)}$ are the maximum and minimum values E can take over all orientations and these are as follows

$$\begin{aligned} E^{(-0)} &= \frac{C_{11}^2 - C_{12}^2}{C_{11}} \\ E^{(+0)} &= \frac{4(C_{11}+C_{12})C_{44}}{C_{11}+C_{12}+2C_{44}} \end{aligned} \tag{4.14}$$

Bounds on G and E, up to the 3rd-order, are shown in Fig. 4.2 for macroisotropic polycrystalline silicon, where the respective Hill averages—the arithmetic mean of the 1st-order Voigt and Reuss bounds—are shown as horizontal straight lines.

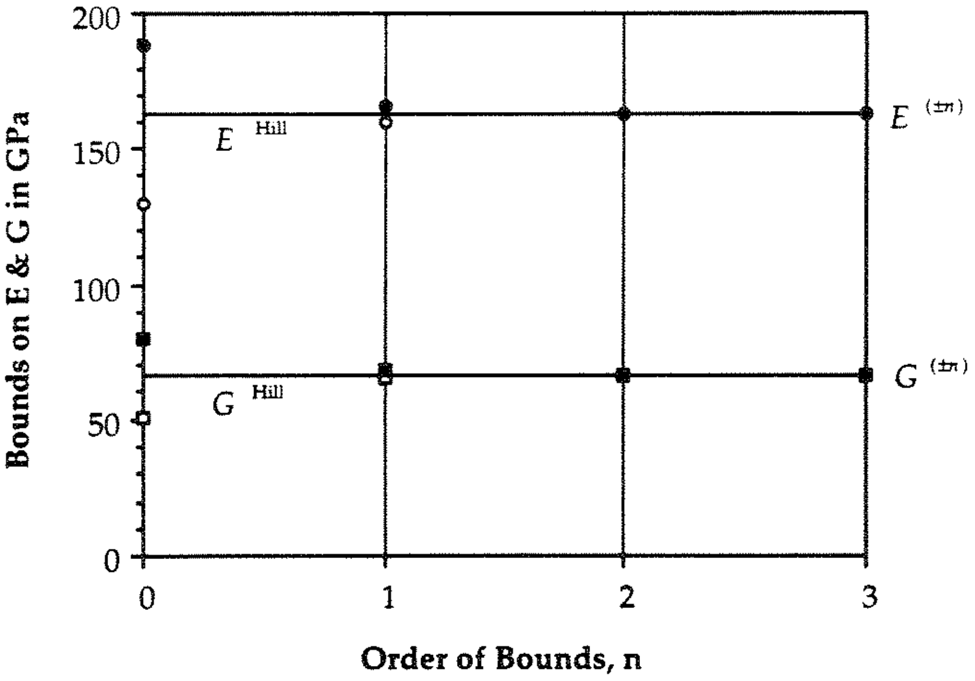

Fig. 4.2 0th-, 1st-, 2nd-, and 3rd-Order Bounds on Young's and Shear Moduli for Untextured Polysilicon & Comparison with Hill Averages

Clearly, the first-order Voigt and Reuss bounds are narrow for polycrystalline silicon. Furthermore, the Hill average is in close agreement with the value to which the higher order bounds are converging. We can therefore conclude that the use of Voigt and Reuss bounds and the Hill average is appropriate in the homogenization of the elastic properties of polycrystalline silicon.

4.3 TEXTURED THIN-FILM POLYCRYSTALLINE SILICON

4.3.1 0th-Order Bounds for {100} and {110} Textures

{100} and {110} textures, i.e. with the {100} and {110} planes lying in the plane of the film, are common in polysilicon thin films as grown in the manufacture and processing of MEMS (see §3.2.2). Results for the variations of Young's modulus are presented for these textures. The 0-th order bounds, i.e. $E^{(\pm 0)}$, define the range of possible values over all in-plane orientations, ψ. For grains randomly oriented in the plane, this is a measure of the uncertainty involved. Figs. 4.3 (a) and (b) show schematic representations of these textures.

It is clear from Fig. 4.3 (a) that properties repeat after every 90° of in-plane rotation, while from Fig. 4.3 (b) it can be inferred that repetition occurs only after 180° of in-plane rotations.

The transformed stiffness matrix, $\mathbf{C}^*$, previously defined in §3.3.5 (Eq. 3.31) in terms of the crystal-fixed stiffness matrix, $\mathbf{C}$, and the 6x6 transformation matrix $\mathbf{Q}$ (Eqs. 3.19–23) is shown again below

$$\mathbf{C}^* = \mathbf{Q}\,\mathbf{C}\,\mathbf{Q}^{\mathrm{T}} \tag{4.15}$$

For the case of {100} texture, $\mathbf{C}^*$ takes the following form when defined in terms of the in-plane rotation angle ψ:

$$C^* = \frac{1}{4}\begin{bmatrix} 4C_{11}+[1-\cos(4\psi)]U & 4C_{12}-[1-\cos(4\psi)]U & 4C_{12} & 0 & 0 & U\sin(4\psi) \\ 4C_{12}-[1-\cos(4\psi)]U & 4C_{11}+[1-\cos(4\psi)]U & 4C_{12} & 0 & 0 & -U\sin(4\psi) \\ 4C_{12} & 4C_{12} & 4C_{11} & 0 & 0 & 0 \\ 0 & 0 & 0 & 4C_{44} & 0 & 0 \\ 0 & 0 & 0 & 0 & 4C_{44} & 0 \\ U\sin(4\psi) & -U\sin(4\psi) & 0 & 0 & 0 & [1+\cos(4\psi)]U+2V \end{bmatrix} \tag{4.16}$$

where

$$\begin{aligned} U &= -C_{11}+C_{12}+2C_{44} \\ V &= C_{11}-C_{12} \end{aligned} \tag{4.17}$$

The in-plane angle, ψ, appears with the coefficient 4, thus verifying the fact that properties repeat every 90°.

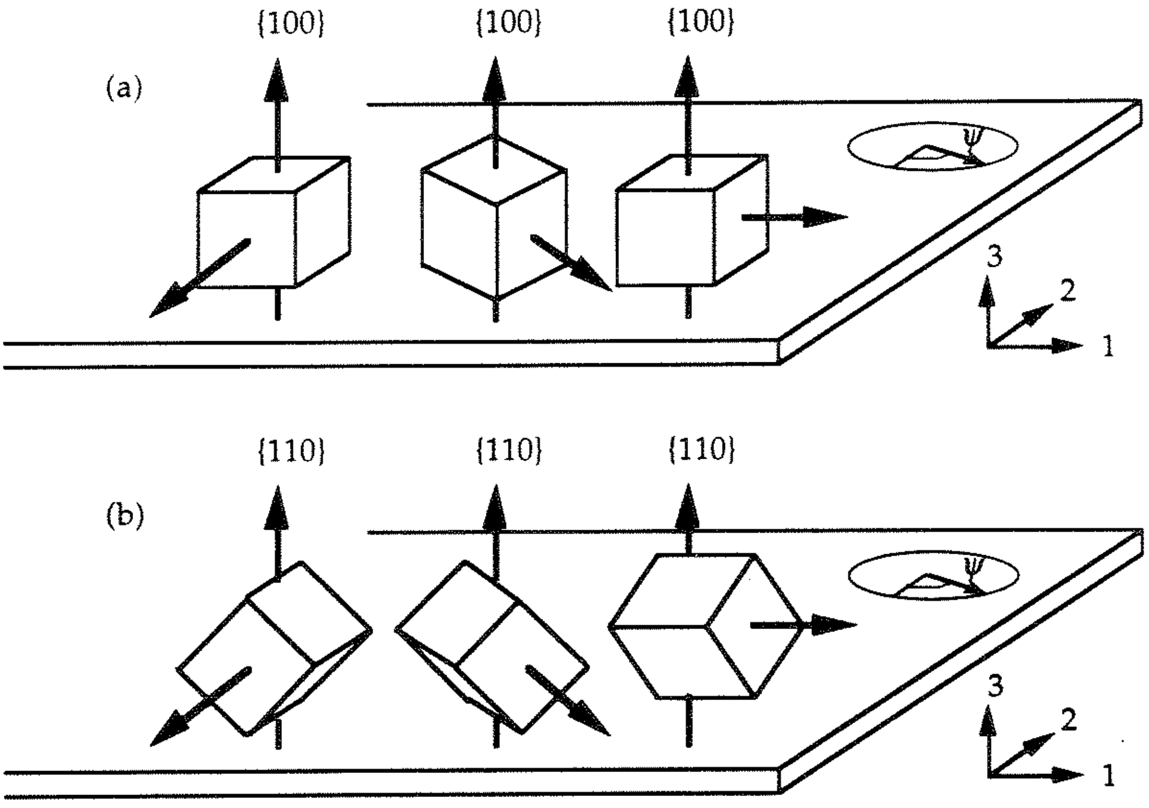

Fig. 4.3 Schematic Diagram for Crystal Orientations in (a): {100}, and (b): {110} Thin-Film Textures, Showing In-Plane Rotations, ψ

For {110} texture, two rotational transformations, $\mathbf{Q}_a$ and $\mathbf{Q}_b$, are evaluated using Eqs. 3.19–23 for the 45° rotation about the x_2 axis (achieving {110} texture) and the in-plane variable rotation ψ, respectively. The derivation of $\mathbf{C}^*$ then takes the following form:

$$\mathbf{C}^* = \mathbf{Q}_b \left(\mathbf{Q}_a\, \mathbf{C}\, \mathbf{Q}_a^T\right) \mathbf{Q}_b^T \tag{4.18}$$

The non-zero elements in $\mathbf{C}^*$ are shown below:

$$\begin{aligned}
C_{11}^* &= \tfrac{1}{16}[16C_{11} - 3U\cos(4\psi) + 7U + 4U\cos(2\psi)] \\
C_{12}^* &= \tfrac{1}{16}[16C_{11} - 32C_{44} + 13U + 3U\cos(4\psi)] \\
C_{13}^* &= \tfrac{1}{4}[4C_{12} - U\cos(2\psi) - U] \\
C_{16}^* &= \tfrac{1}{16}[2U\sin(2\psi) - 3U\sin(4\psi)] \\
C_{22}^* &= C_{11}^* \\
C_{23}^* &= \tfrac{1}{4}[U\cos(2\psi) - U + 4C_{12}] \\
C_{26}^* &= \tfrac{1}{16}[2U\sin(2\psi) + 3U\sin(4\psi)] \\
C_{33}^* &= \tfrac{1}{2}(2C_{11} + U) \\
C_{36}^* &= -\tfrac{1}{4}[U\sin(2\psi)] \\
C_{44}^* &= \tfrac{1}{4}[2V + U + U\cos(2\psi)] \\
C_{45}^* &= C_{36}^* \\
C_{55}^* &= \tfrac{1}{4}[2V + U - U\cos(2\psi)] \\
C_{66}^* &= \tfrac{1}{16}[8V + 5U + 3U\cos(4\psi)]
\end{aligned} \tag{4.19}$$

where U and V are as defined in Eq. 4.17. Note that in both cases $\mathbf{C}^*$ is a symmetric stiffness matrix. The in-plane angle, ψ, appears above with coefficients 2 and 4, thus verifying the fact that properties repeat every 180°.

The Young's modulus in the x_1 direction, E_{11}, is derived for {100} texture in terms of the in-plane orientation angle ψ, using the relation $E_{11} = 1/S_{11}^*$, where $\mathbf{S}^* = [\mathbf{C}^*]^{-1}$. This results in a simple analytic expression for the Young's modulus in the x_1 direction, $E_{11}^{\{100\}}(\psi)$, given by

$$E_{11}^{\{100\}}(\psi) = \frac{1}{a\cos 4\psi + b} \tag{4.20}$$

where a and b are constants related to C_{11}, C_{12}, and α as follows:

$$a = \frac{(\alpha - 1)}{4(C_{11} - C_{12})\alpha} \tag{4.21}$$

$$b = \frac{(3\alpha + 1)C_{11} + (1 - \alpha)C_{12}}{4(C_{11}^2 - C_{12}^2)\alpha} \tag{4.22}$$

and α, the "degree of anisotropy," is defined as

$$\alpha = \frac{2C_{44}}{(C_{11} - C_{12})} \tag{4.23}$$

An analytic expression is similarly derived for the {110} case; however, it is too lengthy to express conveniently (it takes up more than ninety lines of FORTRAN code). The above derivations were performed using the symbolic manipulation code MACSYMA [4.25].

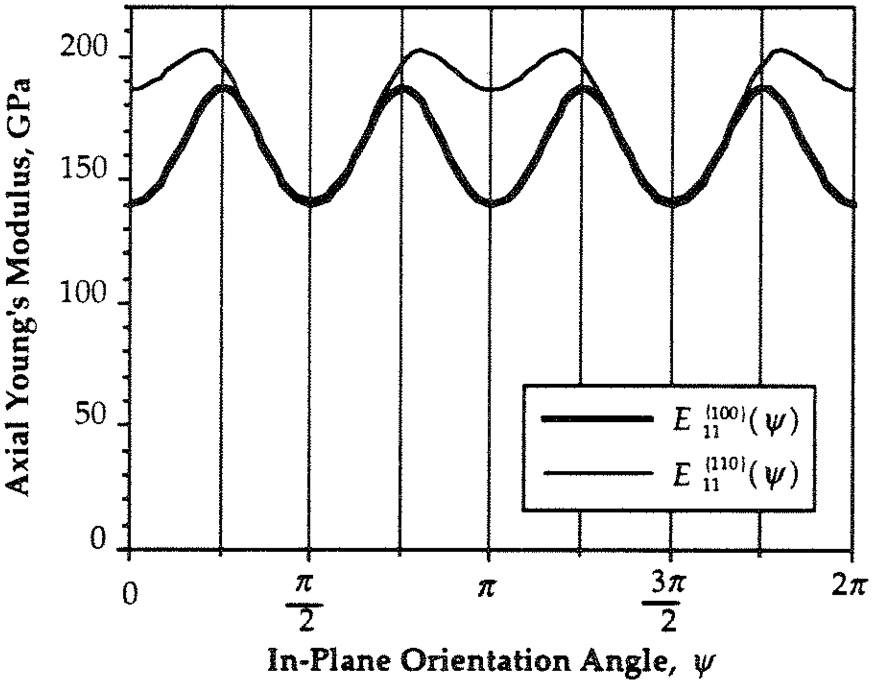

Fig. 4.4 Variations of $E_{11}(\psi)$ for {100} and {110} Textures

For comparison purposes, plots of $E_{11}(\psi)$ vs. ψ are shown for both {100} and {110} textures in Fig. 4.4. The range of values that $E_{11}(\psi)$ takes is of particular importance in cases where homogenization techniques cannot be applied. Due to the small number of crystal grains contributing to the overall structural behavior in these cases, the uncertainty in the response is proportional to the range which the elastic moduli (e.g. $E_{11}(\psi)$) take. This issue is explored in Chapter 5.

4.3.2 VRH Bounds for {100} Texture

Analytical expressions are derived for the Voigt and Reuss estimates of the stiffness matrix using Eq. 4.5 and the symbolic manipulation code MACSYMA [4.25]. For transverse isotropy, with uniform ODF in the ψ direction and with $\theta = \phi = 0$ (i.e. {100} texture), the problem may be treated as a plane problem, thus only a 3 by 3 submatrix (the planar components from the **C** matrix definition in §3.3) needs to be examined. The following is assigned for ODF:

$$f(\theta, \psi, \phi) = \delta(\theta = 0)\delta(\phi = 0)1 \qquad (4.24)$$

resulting in the following Voigt and Reuss estimates

$$\mathbf{C}^{V}_{\{100\}} = \frac{1}{4}\begin{bmatrix} (\alpha+3)C_{11} + (1-\alpha)C_{12} & (\alpha+3)C_{12} + (1-\alpha)C_{11} & 0 \\ (\alpha+3)C_{12} + (1-\alpha)C_{11} & (\alpha+3)C_{11} + (1-\alpha)C_{12} & 0 \\ 0 & 0 & (C_{11} - C_{12})(\alpha+1) \end{bmatrix} \qquad (4.25)$$

and

$$\mathbf{C}^{R}_{\{100\}} = \frac{1}{2(\alpha+1)}\begin{bmatrix} (3\alpha+1)C_{11} + (1-\alpha)C_{12} & (3\alpha+1)C_{12} + (1-\alpha)C_{11} & 0 \\ (3\alpha+1)C_{12} + (1-\alpha)C_{11} & (3\alpha+1)C_{11} + (1-\alpha)C_{12} & 0 \\ 0 & 0 & 2\alpha(C_{11} - C_{12}) \end{bmatrix} \qquad (4.26)$$

respectively, with the degree of anisotropy, α, defined in Eq. 4.23. These results concur with earlier work [4.11].

Transverse isotropy implies that the in-plane elastic properties are fully described by two independent parameters. Here, G and E are chosen. The

Voigt and Reuss bounds on the shear modulus, G^V and G^R, respectively, are as follows:

$$G^V_{\{100\}}(\alpha) = \frac{(\alpha+1)(C_{11}-C_{12})}{4} \qquad G^R_{\{100\}}(\alpha) = \frac{\alpha(C_{11}-C_{12})}{(\alpha+1)} \tag{4.27}$$

These are normalized by dividing by the value of G for the transversely isotropic case ($\alpha = 1$), resulting in

$$\frac{G^V_{\{100\}}(\alpha)}{G^{isotropic}_{\{100\}}} = \frac{(\alpha+1)}{2} \qquad \frac{G^R_{\{100\}}(\alpha)}{G^{isotropic}_{\{100\}}} = \frac{2\alpha}{(\alpha+1)} \tag{4.28}$$

where

$$G^{isotropic}_{\{100\}} = G^V_{\{100\}}(\alpha=1) = G^R_{\{100\}}(\alpha=1) = \tfrac{1}{2}(C_{11}-C_{12}) \tag{4.29}$$

Similarly, the Voigt and Reuss bounds on Young's modulus, E^V and E^R, respectively, are as follows:

$$E^V_{\{100\}}(\alpha) = \frac{2(\alpha+1)(C_{11}^2-C_{12}^2)}{(\alpha+3)C_{11}+(1-\alpha)C_{12}} \qquad E^R_{\{100\}}(\alpha) = \frac{4\alpha(C_{11}^2-C_{12}^2)}{(3\alpha+1)C_{11}+(1-\alpha)C_{12}} \tag{4.30}$$

These are normalized by dividing by the value of E for the transversely isotropic case ($\alpha = 1$), resulting in

$$\frac{E^V_{\{100\}}(\alpha)}{E^{isotropic}_{\{100\}}} = \frac{2(\alpha+1)C_{11}}{(\alpha+3)C_{11}+(1-\alpha)C_{12}} \qquad \frac{E^R_{\{100\}}(\alpha)}{E^{isotropic}_{\{100\}}} = \frac{4\alpha C_{11}}{(3\alpha+1)C_{11}+(1-\alpha)C_{12}} \tag{4.31}$$

where

$$E^{isotropic}_{\{100\}} = E^V_{\{100\}}(\alpha=1) = E^R_{\{100\}}(\alpha=1) = C_{11} - \frac{C_{12}^2}{C_{11}} \tag{4.32}$$

Normalized values of the Voigt and Reuss bounds and the Hill average for *G* and *E* are plotted against the anisotropy parameter, α, in Figs. 4.5 and 4.6, respectively.

These results indicate that, in contrast with materials with much higher degrees of anisotropy, the Voigt and Reuss bounds for polysilicon ($\alpha = 1.562$) are relatively narrow and the Hill estimate is a sufficiently close approximation to the elastic moduli. There is therefore no pressing need for obtaining higher-order statistics on the material microstructure in order to achieve narrower bounds. For materials with high degrees of anisotropy, the use of higher order homogenization schemes is required for an accurate estimation of the effective elastic properties.

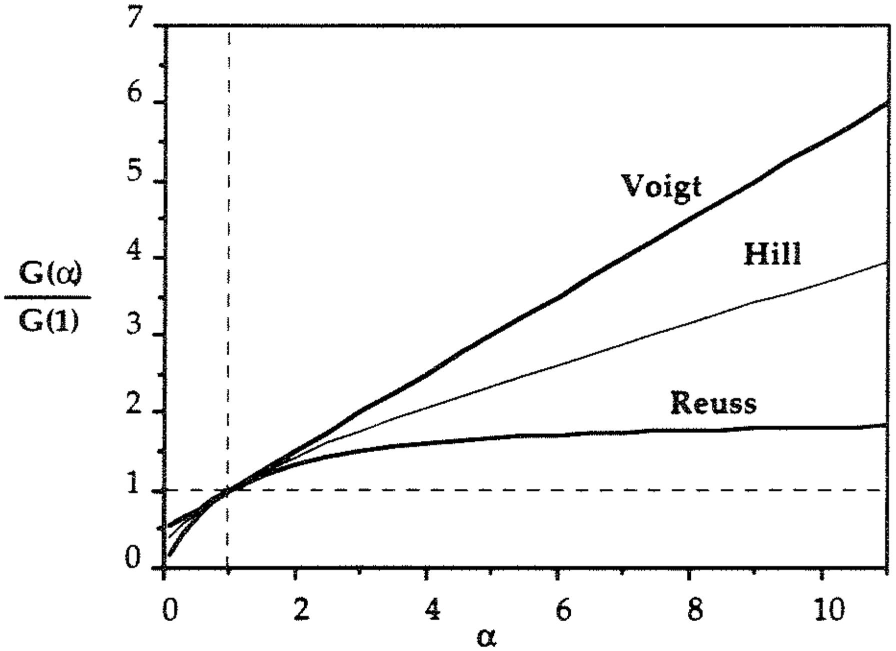

Fig. 4.5 VRH Averages for Normalized Shear Modulus vs. Degree of Anisotropy, α, for {100} Texture

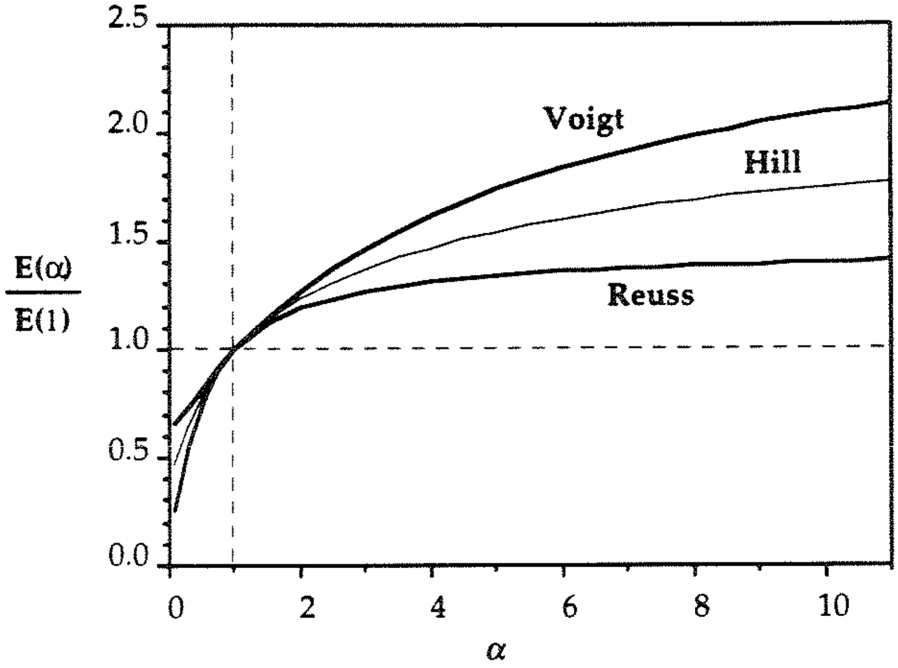

Fig. 4.6 VRH Averages for Normalized Young's Modulus vs. Degree of Anisotropy, α, for {100} Texture

4.4 SUMMARY

Polysilicon, like all polycrystalline materials, is a heterogenous material. This heterogeneity, however, becomes insignificant as the macroscopic scales become increasingly large. Problems in which a RVE can be shown to exist for the polycrystalline material, i.e. where statistical averaging can take place, can be approximated as a homogeneous continuum. This approximation is termed homogenization. The expected effective elastic moduli are predicted using bounding techniques relying on energy principles. These bounds become narrower with increased statistical knowledge about the microstructure of the material. The first-order Voigt and Reuss bounds or the narrower second-order Hashin-Strikman bounds are normally adequate in bounding the elastic moduli for a polycrystal of moderate anisotropy. The results presented in this chapter indicate that the Voigt and Reuss bounds on the elastic moduli of polysilicon are sufficiently close for use in the material modelling of textured fine-grained samples.

While for polysilicon the Voigt and Reuss bounds are narrow, for the multicrystalline case the uncertainty in the effective elastic properties would be significant as evidenced by the significant range in the 0th order bounds shown in Figs. 4.2 and 4.4. Homogenization techniques generally apply for cases where a very large number of crystals are averaged. The importance of grain size in relation to the smallest dimension of the structure, would therefore increase for multicrystalline structures where there are only a few grains, i.e. a RVE does not exist, and statistical averaging cannot be performed. These are examined in Chapter 5 where a new modeling approach is taken in predicting their behavior.

CHAPTER 4 REFERENCES

[4.1] Bunge, H. J., *Krist. Tech.* **3**, 431 (1968).

[4.2] Bunge, H. J., *Texture Analysis in Materials Science*, Butterworth, Berlin 1982 (p. 42).

[4.3] Chandrasekar, S. and S. Santhanam, "A Calculation of the Bulk Modulus of Polycrystalline Materials," *J. Mat. Sci.* **24**, 4265 (1989).

[4.4] Ferrari, M. and G. C. Johnson, "The Equilibrium Properties of a 6mm Polycrystal Exhibiting Transverse Isotropy," *Journal of Applied Physics*. Vol. 63, pp. 4460–4468, 1988.

[4.5] Ferrari, M. and G. C. Johnson, "The Effective Elasticities of Short-Fiber Composites with Arbitrary Orientation Distribution," *Mechanics of Materials*, Vol. 8, No. 1, pp. 67–73, 1989.

[4.6] Garbacz, A. and M.W. Grabski, "The relationship Between Texture and CSL Boundaries Distribution in Polycrystalline Materials 1. The Grain Boundary Misorientation Distribution in Random Polycrystal," *Acta Metallurgica et Materialia*, Vol. 41, No. 2, pp. 469–473, 1993.

[4.7] Gubernatis, J. E. and J. A. Krumhansl, "Macroscopic Engineering Properties of Polycrystalline Materials: Elastic Properties," *Journal of Applied Physics*. Vol. 46, 1875–1883, 1975.

[4.8] Hashin, Z. and S. J. Shtrikman, *J. Mech. Phys. Solids* **10**, 343 (1962).

[4.9] Hill, R., *Proc. Phys. Soc.* **A65**, 349 (1952).

[4.10] Hirsekorn, S., "Elastic Properties of Polycrystals—A Review," *Textures and Microstructures*, Vol. 12, 1, 1990.

[4.11] Johnson, G. C., "Acoustoelastic Response of a Polycrystalline Aggregate with Orthotropic Texture," *Journal of Applied Mechanics*, Vol. 52, pp. 659–663, 1985.

[4.12] Kröner, E. J., "Bounds for Effective Elastic Moduli of Disordered Materials," *J. Mech. Phys. Solids* Vol. 25, No. 2, pp. 137–155, 1977.

[4.13] Kröner, E. J., "Self-consistent Scheme and Graded Disorder in Polycrystal Elasticity," *J. Phys. F: Metal Phys.* Vol. 8, No. 11, pp. 2261–2267, 1978.

[4.14] Kröner, E. J., *Engng. Mech. Div. ASCE* **106**, 889 (1980).

[4.15] Morawiec, A., "Calculation of Polycrystal Elastic Constants from Single-Crystal Data," *phys. stat. sol. (b)* **154**, 535, 1989.

[4.16] Morawiec, A. and J. Pospiech, "Functions Describing Orientation Correlations in Polycrystalline Materials," *Textures and Microstructures*, Vol. 19, pp. 67–74, 1992.

[4.17] Morris, Peter R., "Elastic constants of polycrystals," *Int. J. Engng. Sci.* Vol. 8, No. 1, pp. 49–61, 1970.

[4.18] Pospiech, J., K. Sztwiertnia, and F. Haessner, "The Misorientation Distribution Function," *Textures and Microstructures*, Vol. 6, pp. 201–215, 1986.

[4.19] Reuss, A. Z., *angew. Math. Mech.* **9**, 55 (1929).

[4.20] Sisodia, P., A. Dhoble, and M. P. Verma, "Shear Moduli of Macro-isotropic Cubic Polycrystalline Materials," *phys. stat. sol. (b)* Vol. 163, No. 2, 345–354, 1991.

[4.21] Voigt, W., *Lehrbuch der Kristallphysik*, Teubner, Leipzig 1928 (p. 962).

[4.22] Watt, J. P., "Hashin-Shtrikman Bounds on the Effective Elastic Moduli of Polycrystals with Trigonal (3,3) and Tetragonal (4,4,4m) Symmetry," *J. Appl. Phys.* Vol. 60, No. 9, pp. 3120–3124, 1986.

[4.23] Zuo, Liang, Jiazheng Xu, and Zhide Liang, "Averaging Fourth-Rank Elastic Tensors for Textured Polycrystalline Aggregates Without Physical Symmetry," *Journal of Applied Physics*, Vol. 66, No. 6, pp. 2338–2341, 1989.

[4.24] *Proc. IEEE Micro Electro Mechanical Systems*, Nara, Japan, 1991

[4.25] The Mathlab Group Laboratory for Computer Science, MIT, *MACSYMA Reference Manual*, Version 10, 1993.

Chapter 5

MULTICRYSTALLINE SIMULATION MODEL

5.1 INTRODUCTION

This chapter presents a discrete geometric model of multicrystalline structures. A continuous parameter random field is defined which models multicrystalline material structures' mechanical behavior. Advanced image analysis techniques for obtaining the geometrical details of the mictrostructure of materials are discussed. Various mathematical models of the geometry of the multicrystalline structure are then outlined, followed by a detailed study of the most realistic and applicable of these models, the Poisson Voronoï diagram (PVD) [5.3]. After outlining algorithms for the construction of PVDs, relevant statistical and geometrical properties of this model are presented. This is followed by a description of how PVDs can be applied in the analysis of MEMS, including pointers to how calibration of the mathematical models can be achieved. Finally, details of the finite element implementation are delineated, including a discussion of element characteristics, mesh generation, mesh refinement, and error analysis for two-dimensional problems.

5.2 IMAGE ANALYSIS OF MATERIAL MICROSTRUCTURE

Recent advances in image analysis, especially as applied to the field of computational materials science, have provided tools that can be used in studying the microstructure of semiconductors, the primary materials used in MEMS. As indicated in §3.5, digital-image-based microstructures are now routinely retrieved from scanning electron micrographs (SEMs) and transmission electron micrographs (TEMs). These images can be stored for later use in the study of the material properties using computer simulations. This is true not only for advanced composites and ceramics, but also for more traditional materials such as portland cement [5.9].

The geometric microstructural characteristics of a polycrystalline material sample is fully described when the shape, size, and location of each individual crystal grain and its associated boundary region is defined. For the process conditions and structural dimensions currently typical in MEMS fabrication that result in 'multicrystalline' bodies, it is valid to assume that the grain boundaries are infinitesimally thin compared to the grain sizes. The grain boundaries can therefore be represented in terms of a set of lines in two-dimensions (2-D), or surfaces in three-dimensions (3-D). These lines and surfaces divide the region of interest into a space-filling mosaic of distinct, enclosed cells which represent the crystal grains. The main aim in image analysis for our purposes is, therefore, to extract the complete and correct set of grain boundaries associated with a particular sample.

The inputs for the image analysis are TEMs of the typical material used in MEMS, i.e. polycrystalline silicon (polysilicon). An example of this is shown in Fig. 5.1. These images are 2-D representations of polysilicon's 3-D microstructure. Generally, the full 3-D microstructure would be of interest. However, for thin film polysilicon with columnar grains (a common phenomenon in MEMS) the grain boundaries are perpendicular to the plane of the film. Therefore, a 2-D representation is sufficient. Thus, a plan-view TEM

gives complete information about the geometrical characteristics of the microstructure. Numerous stereological techniques are available for the correct interpretation of 2-D representations of general 3-D microstructures [5.2, 5.19, 5.26, 5.31]. An approach based on PVDs is presented in §5.4.3.

Fig. 5.1 TEM of the Microstructure of Polycrystalline Silicon

Russ [5.20] outlines systematic approaches to the image analysis of the microstructure of materials. He discusses methods that extract the microstructure of polycrystalline samples using gradient operators to locate boundaries between crystal grains, e.g. of the type shown in Fig. 5.1. In two recent papers, Sakaue [5.21] and Takeuchi [5.28] outline state-of-the-art techniques used respectively to extract grain boundary information from sample images and to repair any defects in the images. These techniques, applicable to polycrystalline samples, produce an output that is a space-filling mosaic representing the real microstructural geometric structure.

Using the above methodology, a set of sample TEMs of the material microstructure, corresponding to a particular process condition, can be analyzed, and a representative set of geometric data obtained (TEM in Fig. 5.1 kindly provided by Peter A. Krulevitch). This data can then be used to calibrate theoretical geometric models. These are discussed in the following section.

5.3 THEORETICAL MODELS

If we have a single sample of material which we wish to analyze, we would not need to consider the problem from a statistical point of view; we could formulate the problem simply based on the single-sample information obtained by image analysis of the TEM. However, we are not concerned here with the detailed variation of a single sample. Rather, we wish to be able to predict the behavior of a large class of samples prepared using the same process conditions. Short of the direct use of a large representative database of empirical information (with the associated costs of manufacturing, experimental data acquisition, storage, and processing) we are forced to use mathematical models that idealize the actual geometric structures found by image analysis. Some applicable models are discussed in this section.

In §3.3, various grain growth simulation models were discussed in which the process kinetics is modeled, ultimately producing a final crystal grain structure for the material under study. Srolovitz, et al. [5.22] are the main proponents of these approaches, which model physical phenomena at the various micro- and macro- scales involved in the processing and subsequent annealing of materials. These simulation models, however, have been mainly restricted to metallic materials, and may not be directly applicable to the materials used in MEMS, e.g. polycrystalline silicon. Moreover, the models used by Srolovitz et al. do not model the relevant processing methods used in MEMS technology, e.g. low pressure chemical vapor deposition (LPCVD) (see §2.1). While, in their present form, these models are not readily applicable to MEMS material microstructures, with appropriate adaptations, they may have future applications in modelling process-sensitive phenomena such as spatial residual stress variations, spatial correlation of grain orientations, etc.

A class of geometric models for the random subdivision of space into cells, or 'crystals,' is now considered. These models are based on a concept analogous to the physical process of crystal growth. One starts with an arrangement of points in space, representing the 'seeds' or nuclei of the crystal grains. The simplifying assumption is that the seeds grow at the same rate in all directions, i.e. as spheres, staying fixed in space without pushing apart as they grow into contact [5.10]. These models provide a flexibility that allows their use in modelling a wide range of polycrystalline microstructures. The model parameters can be identified by employing empirical data obtained through the image analysis techniques outlined in §5.2.

Depending on the initial conditions, two different sub-classes of these models arise. If all the seeds start to grow at the same time, the resulting model will have cells with either straight edges (in 2-D) or planes (in 3-D) delineating their boundaries. This model is called the Voronoï diagram [5.3]. However, if the nuclei are allowed to start growing at different times (but neglected if they fall within an already growing cell), the resulting model would generally have cells with curved boundary lines or surfaces. This is called the Johnson-Mehl model [5.10]. Figs. 5.2 and 5.3a show planar examples of these two models.

These models have a high degree of flexibility in their final form. Firstly, differing initial seed arrangements result in qualitatively different final outcomes. Secondly, the tessellations can be transformed through stretching. An example of this is shown in Fig. 5.3b, where the Voronoï diagram of Fig. 5.2 has been thus transformed.

More involved techniques of transforming tessellations of the type shown in Figs. 5.2 and 5.3a also exist. Kawasaki et al. [5.13] present vertex models for 2-D grain growth. Starting from a generated Voronoï diagram, various geometric rules analogous to annealing mechanisms are used in determining time-dependent evolutionary changes in the topology, such as grain recombination and annihilation. The resulting tessellations have larger average grain sizes than the initial tessellations. Vaz et al. [5.32] show a similar approach, but start with a stretched Voronoï diagram prior to the simulated grain growth phase.

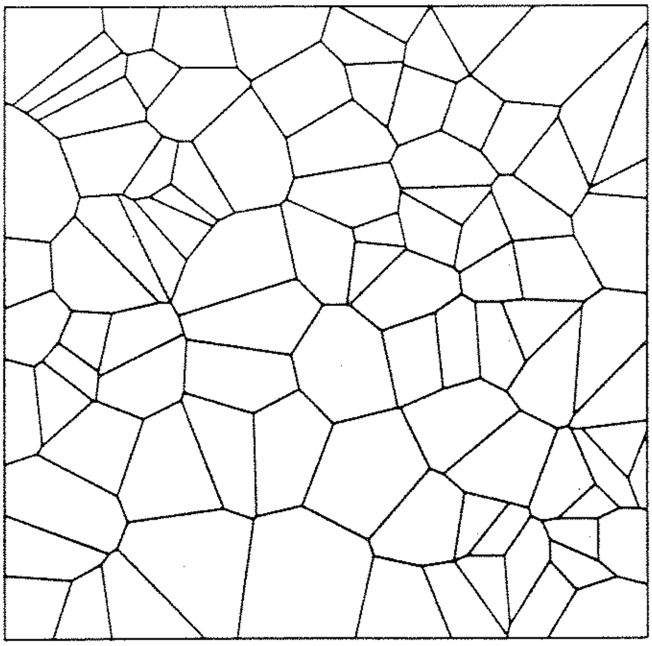

Fig. 5.2 Voronoï Diagram in 2-D

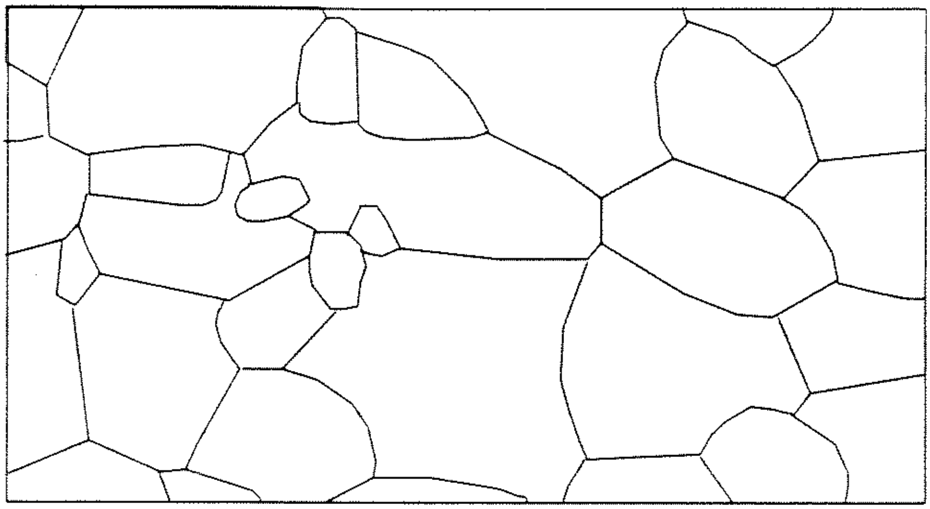

Fig. 5.3a Johnson-Mehl Model in 2-D

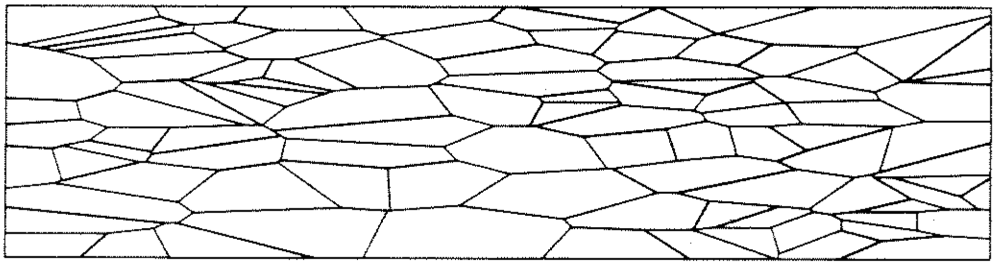

Fig. 5.3b Transformed Voronoï Diagram

These techniques open new possibilities in modelling some of the physical phenomena that lead to the final material microstructure in MEMS. However, in order to have realistic models, significant studies must first be made of the relevant physical processes involved in the material processing and annealing. These additional studies would have to include the estimation of temperature- and pressure-dependent parameters and the exploration of complications created by the addition of impurities such as dopants. In their present form, however, these vertex models are not readily applicable to problems in MEMS.

Clearly, a large array of geometric models exist that could be tailored for appropriate use in modelling MEMS material microstructures. In this study, the Voronoï diagram is used due to its flexibility and simplicity, its well understood properties, and the availability of robust algorithms for its construction.

5.4 VORONOÏ DIAGRAMS

Voronoï diagrams are one of the most fundamental data structures in computational geometry [5.3]. In this section, the various forms and basic properties of these diagrams are introduced and their use in modelling multicrystalline microstructures is discussed. A detailed description of Voronoï diagrams is presented, including outlines of the various alternative algorithms used for their construction. Their application to the modelling of the mechanics of random non-homogeneous discrete systems such as multicrystalline and polycrystalline structures in MEMS is then discussed.

5.4.1 Review

Voronoï diagram is the term used to describe a particular geometric structure that subdivides n-dimensional Euclidean space into disjoint regions based on a set of generating points in that space [5.3].

The simplicity and intuitive appeal of this concept has meant that Voronoï diagrams have been 'discovered' on numerous occasions and studied fairly independently in different fields. In the applied natural sciences, Voronoï diagrams are used in modelling natural phenomena in diverse fields such as astronomy [5.12], crystallography [5.27], ecology [5.5], and meteorology [5.29]. In mathematics, they are used as auxiliary structures for investigating and calculating related mathematical objects. In computer science, they serve as a data structure for algorithmic problems that are inherently geometric. This diversity of application and 'discovery' has resulted in a plethora of names describing the same geometric structure, e.g. *Dirichlet tessellation, area of influence polygons, Thiessen polygons, Wigner-Seitz regions.*

The Voronoï diagram has a dual tessellation called the Delaunay tessellation [5.18]. For each Voronoï edge (2-D) or face (3-D) that connects two Voronoï cells, one can connect the seeds of those cells with a straight line. This construction of lines would result in the Delaunay triangulation of the seeds (Fig. 5.4). This tessellation has also found widespread use, e.g. for automatic mesh generation in finite element applications [5.18].

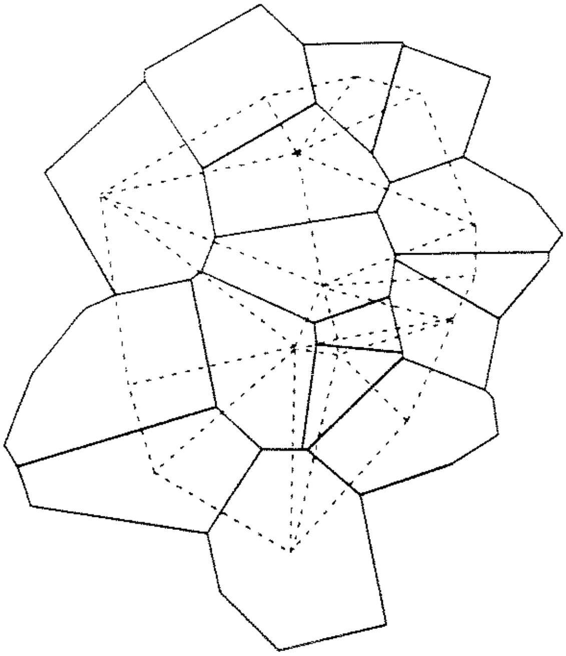

Fig. 5.4 Delaunay Triangulation Over Voronoï Cell Seeds

Only in the last two years have unifying approaches to the exposition of the mathematical and algorithmic properties and application areas of

Voronoï diagrams and Delaunay tessellations appeared in the scientific literature. The survey paper by Aurenhammer [5.3] and the book by Okabe *et al.* [5.18] are the best examples of such approaches to date.

5.4.2 Construction of Planar Voronoï Tesselations

Given some number of generated points in the plane, the Voronoï diagram, or tessellation, associated with those points divides the plane according to the *nearest-neighbor rule*: each generated point is associated with the region of the plane closest to it. The generated regions in the plane, called Voronoï cells, are convex polyhedra, bounded by straight lines which are the perpendicular bisectors of the lines joining adjacent nuclei (Fig. 5.2).

This concept can be extended to three dimensions, with similar results, except bisecting planes replace the bisecting lines and each region or cell becomes a convex polyhedron.

The construction algorithm used here is an extension of the method developed by Tipper for the construction of a single planar Voronoï cell [5.30]. Perpendicular bisectors of lines that connect a particular seed, denoted by s^*, and all the other points are first identified. Next, the intersections of the perpendicular bisectors with each other are found. The intersection point closest to s^* is clearly one of the vertices of the Voronoï cell associated with s^*. Starting from this point, the perimeter of the Voronoï cell is defined by going along successive intersecting bisectors until the cell is closed. This is shown in Fig. 5.5, where s^* is the central seed. The single-cell method is then repeated for all other cells.

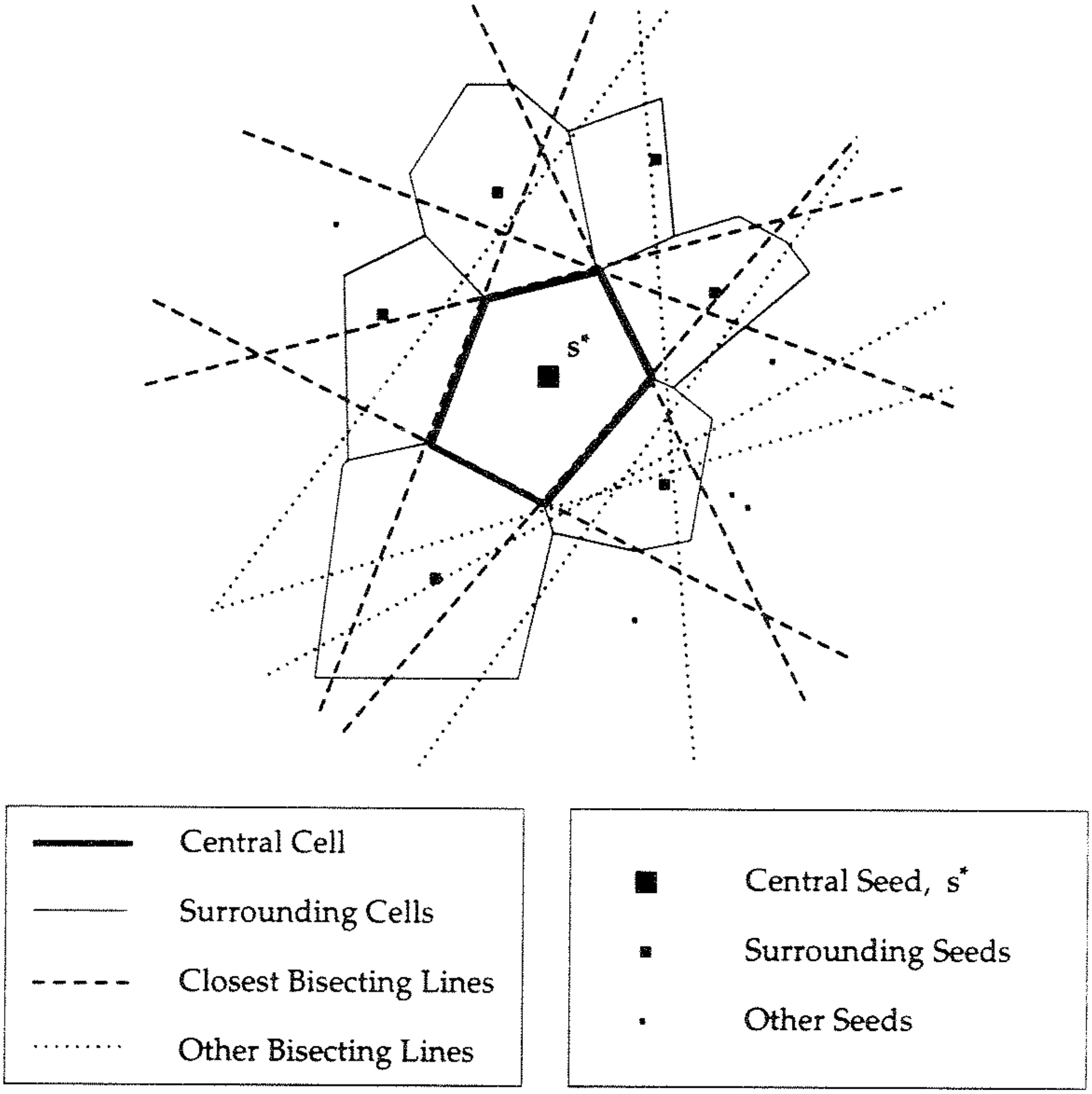

Fig. 5.5 Construction of One Voronoï Cell

5.4.3 Basic Properties

The properties of the Voronoï diagram depend on the generating set of points. Different models for planar or spatial point arrangements produce different Voronoï diagrams. These generating points may be either deterministic or probabilistic. The latter is often referred to as a point process.

An interesting and useful point process is the Poisson point process [5.7, 5.18, 5.24]. Voronoï diagrams based on this process, commonly referred to as Poisson-Voronoï Diagrams (PVDs), have widely studied properties. Statistics have been either analytically derived or numerically generated, describing the properties of cell areas, cell side lengths, number of vertices per cell and internal angles of cell vertices. PVDs are also representative of many naturally occurring phenomena, including the structure of poly- and multi-crystalline arrangements in metallic materials [5.3, 5.18]. Some authors have pointed out some of the shortfalls of PVDs. For example, Weaire and Rivier [5.33] indicate that PVDs have different appearances from space-filling natural structures. Rivier [5.14] has suggested that PVDs represent 'young' structures which are not fully equilibrated under the influence of constraints. This concept is analogous to polycrystalline sample microstructures prior to annealing.

Another interesting and potentially useful Voronoï diagram is one where the seed locations are associated with the eigenvalues of complex random matrices. This Voronoï diagram is sometimes referred to as the Random Matrix Voronoï Froth (RMVF) [5.15]. RMVFs are more regular than PVDs, and are claimed to model certain natural phenomena better than PVDs [5.15].

Although RMVFs overcome some of the shortfalls of PVDs, RMVFs are purely limited to planar applications since the real and imaginary parts of the eigenvalues of complex matrices are used to define the two coordinates of the seeds in the plane. Furthermore, studies of statistical properties of RMVF cells have been limited to a few simulation studies. Due to these limitations, PVDs are chosen over RMVFs for further study and application to modelling MEMS material microstructures. The following section describes in detail the properties of PVDs.

5.4.4 Poisson-Voronoï Diagrams

5.4.4.1 Definition

When the generating set of points for a Voronoï diagram are located in the plane or in 3-D space according to the homogeneous Poisson point process, the resulting tessellation is referred to as the Poisson Voronoï diagram (PVD) [5.18]. According to this process, the probability that $N(A) = x$ points are located in any subset A in $\Re^n$ is given by

$$\mathrm{P}(N(A) = x) = \frac{(\lambda A)^x e^{-\lambda A}}{x!}, \; x = 0,1,2,\ldots \tag{5.1}$$

where the intensity of the process, λ, is a constant that equals the mean density of points in a unit volume, when $n = 3$, or unit area, when $n = 2$ [5.18]. This definition can be generalized by relaxing the homogeneity, and defining the point process by

$$\mathrm{P}(N(A) = x) = \frac{[m(A)]^x e^{-m(A)}}{x!}, \; x = 0,1,2,\ldots \tag{5.2}$$

where

$$m(A) = \int_A \lambda(\mathbf{x}) dA \tag{5.3}$$

This point process is called the general Poisson point process, with the intensity function $\lambda(\mathbf{x})$, where $\mathbf{x}$ denotes the spatial coordinate. Here, however, we restrict our study to the homogeneous Poisson point process.

5.4.4.2 Properties and Uses

Due to the widespread use of PVDs, there has been great interest in obtaining information about them. This information includes moments, distributions, and correlations of various characteristics such as cell areas or volumes, number of sides or faces, perimeter lengths (in 2-D), and side or edge lengths. Analytical first-order moments of a variety of these characteristics have been successfully derived [5.18]. Although there have been some analytical derivations of higher moments and distributions [5.17], many researchers have resorted to Monte Carlo simulation approaches for estimating many of these properties [5.14, 5.18, 5.23].

The individual cell areas of planar PVDs have been shown to be generalized gamma distributed [5.18]. Another property of particular interest is the chord length. Linear probes in 2-D or 3-D PVDs intersect the cells, with the distance between successive intersections being called the chord length. The distribution of chord lengths for both 2-D and 3-D PVDs have been derived [5.16] and can be approximately modeled using sums of truncated normal distributions. These distributions prove useful in a random field modelling approach described in §6.2.

PVDs can either model a given empirical structure or be used as a normative model against which other tessellations can be evaluated. Their use as applied to modelling MEMS multicrystalline microstructures are outlined in the following section.

5.4.5 Application to MEMS

Calibrating theoretical models, such as PVDs, such that they better represent the real material microstructure would result in varying levels of closeness of fit depending on the complexity of the real problem. Stoyan and Stoyan [5.25] describe methods that can quantify how closely a PVD models an observed tessellation. Criteria can thereby be developed that result in the acceptance or rejection of a PVD as a model. For rejected examples, generalizations of the Voronoï model already described can be employed to obtain a closer fit. For example, use can be made of the non-homogeneous Poisson point process (Eq. 5.2), doubly stochastic Poisson point processes, scaling and stretching techniques, and grain growth extensions of the type proposed by Kawasaki et al. [5.13].

The final results of interest in the analysis of the mechanical response of MEMS, however, are not very sensitive to the accuracy of the geometric models with regard to crystal grain shapes (see Ch. 7). Ferrari and Lin [5.8] have recently reported results for the extensional behavior of multicrystalline beams using a relatively crude model that employs rectangular prisms to model individual crystals. It appears that the influence of the distribution of grain sizes and the associated material texture are the most important factors affecting the global behavior, e.g. the axial or flexural stiffness of multicrystalline beams. This simplifies the calibration of PVDs for application to MEMS structural components.

Local responses such as stresses at critical structural locations would be more sensitive to the closeness of fit of the geometric model. Such local phenomena are critical to failure analyses in fracture and fatigue problems. Further extensions of this methodology to the study of failures, etc. may require the use of more elaborate models of the type outlined in §3.3, §5.3, and above, that more closely fit the actual multicrystalline structure.

In the context of this study, we are interested in the elastic behavior of MEMS, and global responses are of most interest. Using calibrated PVDs, where average grain sizes are matched, we are able to adequately predict, in a probabilistic sense, the global elastic behavior of MEMS structures.

5.5 FINITE-ELEMENT IMPLEMENTATION

The discrete geometric model we have defined will be used to simulate the mechanical behavior of the material microstructure of polysilicon. To this end, we shall use finite elements to analyze an assemblage of silicon crystal grains, with associated orientation angles, making up a multicrystalline structure. The general purpose, research-oriented finite element code FEAP is used for this purpose [5.35].

Due to the large storage and processing requirements associated with simulating and analyzing structures with 3-D PVDs, we shall limit our application of discrete models to 2-D problems. Many problems in MEMS, such as beams and plates with columnar grains, can be modeled in this way. The extension to 3-D, however, can be carried out using a similar methodology.

The finite element model employs an easy to generate, efficient, and convergent finite element discretization mesh that maintains the integrity of the crystal structure such that different orientation angles, ψ, can be assigned for each grain.

In the following sub-sections, the rationale behind the choices for the element formulation, meshing, and mesh refinement is first presented. Then, finite element discretization errors are analyzed and a suitable extrapolation scheme is proposed to reduce these errors.

5.5.1 Element Characteristics

There is no evidence of inelastic deformation at room temperature for polysilicon and there are no slip mechanisms in the diamond cubic structure. Given the types of MEMS structures that are being fabricated [5.34] and the associated range of imposed force and displacement boundary conditions, a linear elastic assumption for the material behavior is therefore appropriate. The linear elastic stress-strain relations for silicon have been defined in §3.3. These relations are defined in the crystal-fixed frame and undergo rotational transformations dependent on the crystal grain orientations defined in terms of Euler angles [5.6]. These general transformations were used in §3.3 to derive stress-strain relations in the global coordinate axes for certain dominant textures found in polycrystalline silicon, namely {100}, {110}, and {111} [5.11]. These relations are now employed in the development of element stiffness matrices.

When discretizing problems based on the crystal structure shown in Fig. 5.2, the integrity of the crystal grains must be maintained since different orientation angles are assigned for each grain. The simplest 'mesh' that could satisfy this requirement would simply be the cell structure of PVDs. For this mesh we would need to employ general n-sided polygonal elements to represent each individual crystal grain. Due to the range of n-sided polygons found in PVDs (3- to 14-sided polygons have been reported [5.17]), we need to formulate either a large number of new elements, or a general adaptable n-sided polygonal element. Since the formulation problems of these approaches would be considerable, and since the resulting elements may have unreliable behavior in modelling planar problems, neither of these approaches will be pursued.

The use of existing quadrilateral elements avoids the problems associated with developing new elements. These elements are well studied and have superior convergence properties. Nevertheless, the use of quadrilateral elements in modelling planar multicrystalline structures presents two problems: maintaining the integrity of the crystal grains, and ensuring that the elements remain easily generatable. These problems are associated with meshing and are outweighed by the advantages of using quadrilateral elements. The solution of the meshing problem will be addressed in §5.5.2.

Meshing of the random geometry of the crystalline polygons generally results in linearly distorted quadrilateral elements. Nine-noded isoparametric quadrilateral elements (Fig. 5.6) are used in this study since they better represent cartesian polynomials than 8-noded elements and are generally preferable in minimizing the finite element discretization errors [5.35].

Material homogeneity is assumed within each crystal, allowing the material coefficients to be taken out of the integrations involving the shape functions, thus simplifying the finite element analysis.

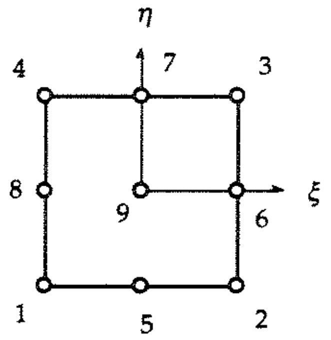

Fig. 5.6 Nine-Noded Isoparametric Quadrilateral Element Showing Node Numbering

5.5.2 Meshing and Mesh Refinement

To maintain the integrity of the crystal structure, each polygonal crystal must be individually discretized. There are an infinite number of ways to discretize an n-sided polygon in terms of quadrilaterals. However, the possibilities for this problem are restricted if we require easy automatic generation of the elements based on the data defining the crystal structure. Additionally, since adjacent crystals share nodes, each node on the edge of the polygons must be matched in these crystals. This further limits discretization options. An illustrative number of typical subdivisions of a pentagon into quadrilaterals that satisfy both the simplicity and node-sharing requirements are shown in Fig. 5.7.

The crystal subdivisions into elements used in this dissertation appear in Figs. 5.7(a) and (b). Fig. 5.7(b) represents a mesh refinement of the subdivision shown in Fig. 5.7(a). Each *n*-sided polygon that defines the crystal boundaries is thus divided into *n* or 3*n* quadrilaterals, enabling convergence checks and the use of extrapolation schemes outlined in §5.5.3.

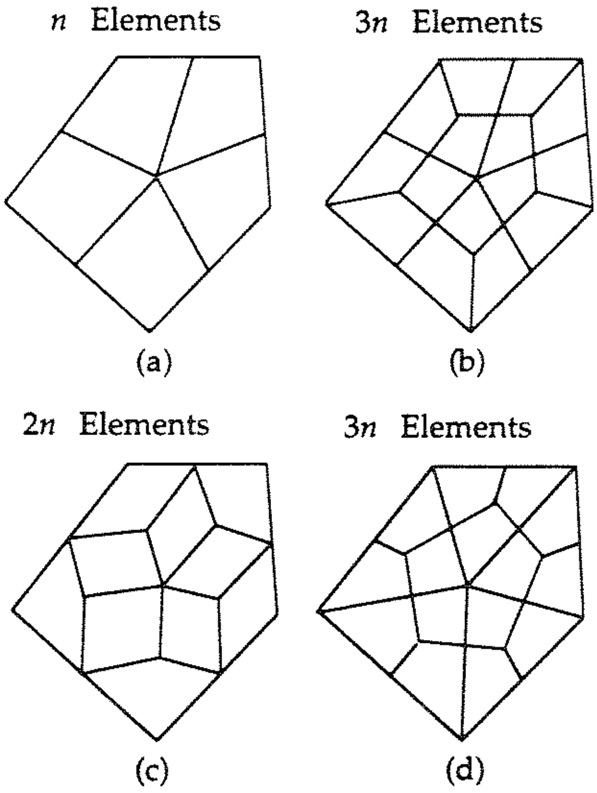

Fig. 5.7 Subdivisions of a Typical Crystal Grain into Quadrilateral Elements

An interesting aspect of the selected mesh refinement pattern is its serendipitous usability in modelling grain boundaries. As indicated in §3.2.1, for fine grained polysilicon, the grain boundary region, which is of the order of a few inter-atomic distances in dimension, becomes significant compared to the 'bulk' crystal grain scales. These boundary regions may have different elastic moduli than the crystal and can be assigned appropriate values, as indicated in §3.5 [5.1]. They can be modeled with separate elements of required width, e.g. as shown in Fig. 5.8, where the shaded region indicates material properties differing from the 'bulk' crystal grain.

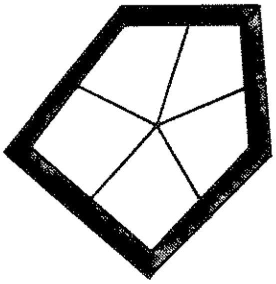

Fig. 5.8 Grain Finite-Element Mesh with Grain Boundaries Shown

5.5.3 Error Analysis and Extrapolation

The finite element method offers only an approximation of the exact solution. We therefore need to gain an understanding of the magnitude of the errors and to formulate our problem such that the desired level of accuracy is economically achieved. To this end, a typical example problem is chosen and the displacement field errors are analyzed. This is followed by a Richardson extrapolation [5.35], using results derived from using the mesh refining sequence outlined in §5.5.2, that is shown to reduce the displacement field errors by at least an order of magnitude.

As an example, the bending behavior of a typical multicrystalline cantilevered beam made up of a finite number, N = 33, of crystals is considered as shown in Fig. 5.9, where the crystal structure is based on the Voronoï tessellation of Poisson points with intensity, $\lambda = 3/d^2$, defined in §5.4.4.1.

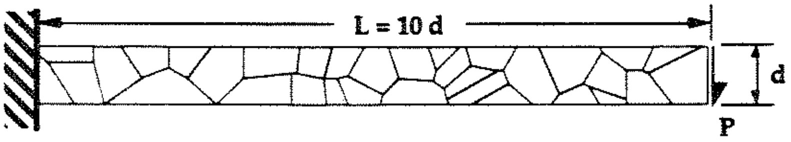

Fig. 5.9 Example "Multicrystalline" Structure and Loading

We wish to minimize the finite element discretization errors associated with the distorted shapes of the quadrilateral elements that divide each n-sided crystal into n or $3n$ elements. A uniform crystal orientation is assigned throughout the beam so that the problem can be first solved using a regular grid of elements. By reducing the size of the grid, convergence is reached to the desired level of accuracy, i.e. our 'exact' result. The problem is then re-solved using the subdivisions based on the crystal structure shown in Fig. 5.9 and the discretizations into quadrilateral finite elements as in Fig. 5.7(a) and again using the mesh refinement as in Fig. 5.7(b). This process is repeated for the full range of in-plane orientation angles, i.e. 0° to 180°. The results are plotted in Fig. 5.10, where the % errors in the tip displacement are shown. Results using a Richardson extrapolation scheme are also included. This scheme is outlined below.

If the displacement is known to converge at $O(h^n)$, two approximate solutions u^1 and u^2 can be obtained with meshes of size h and h/m, respectively. With u being the exact solution, we can write

$$\frac{u^1 - u}{u^2 - u} = \frac{O(h^n)}{O\left((h/m)^n\right)} = m^n \tag{5.4}$$

Therefore an almost exact expression for *u* can be found

$$u = \frac{m^n u^2 - u^1}{m^n - 1} \tag{5.5}$$

The problem considered here employs a non-standard mesh refinement step, dividing each quadrilateral element into 3 rather than 4 smaller elements. Therefore $m = \sqrt{3}$ (rather than $m = \sqrt{4} = 2$), resulting in the following expression for the extrapolated tip displacement in the 2-D problem ($n = 2$):

$$u = \frac{3u^2 - u^1}{2} \tag{5.6}$$

This extrapolation is used in calculating the values plotted in Fig. 5.10. It is clear that the errors of the extrapolated solution are at least an order of magnitude smaller than those for u^1.

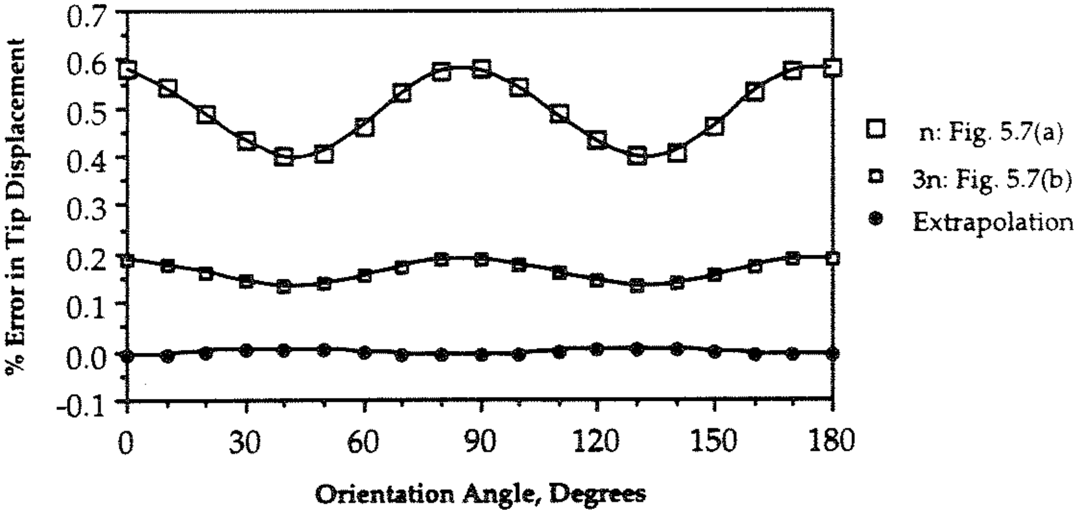

Fig. 5.10 Finite Element Errors and Extrapolation Results

5.6 SUMMARY

This chapter presented details of a proposed multicrystalline simulation model suitable for the probabilistic analysis of multicrystalline MEMS structures. The model in its current form is restricted to 2-D problems; however, the methodology for extension to 3-D is clear. Image analysis techniques that can be used for obtaining empirical data on the material microstructure were first outlined. This was followed by a general description of theoretical models amenable to describing multicrystalline states such as they exist in polysilicon MEMS. The focus was then shifted to the Poisson Voronoï Diagram (PVD) that is the basis for the simulation model presented in this chapter. Finally, the finite element implementation was described.

For implementation as a simulation model, suitably calibrated random tessellations are first generated based on a Poisson point process. These are then modeled using finite elements of the type developed in §5.5 and the boundary value problems are solved using the finite element method. The simulated results are used to estimate the probabilistic responses of interest in Chapter 7.

CHAPTER 5 REFERENCES

[5.1] Alber, I., J. L. Bassani, M. Khantha, V. Vitek, and G. J. Wang, "Grain Boundaries as Heterogeneous Systems—Atomic and Continuum Elastic Properties," *Philosophical Transactions of the Royal Society of London, Series A, Physical Sciences and Engineering*, Vol. 339, No. 1655, pp. 555–586, 1992.

[5.2] Ambartzumian, R. V., *Combinatorial Integral Geometry with Applications to Mathematical Stereology* [edited with an appendix by Adrian Baddeley], Wiley, New York, 1982.

[5.3] Aurenhammer, F., "Voronoï Diagrams—A Survey of a Fundamental Geometric Data Structure," *ACM Computing Surveys*, Vol. 23, No. 3, pp. 345-405, 1991.

[5.4] Beran, Mark J., *Statistical Continuum Theories*, Interscience Publishers, New York, 1968.

[5.5] Brown, G. S., "Point Density in Stems Per Acre," *New Zealand Forestry Service Research Notes*, Vol. 38, pp. 1–11, 1965.

[5.6] Bunge, H. J., *Texture Analysis in Materials Science*, Butterworth, Berlin, 1982 (p. 42).

[5.7] Cox, D. R. and V. Isham, Point Processes, Chapman and Hall, London, 1980.

[5.8] Ferrari, M. and C-L. Lin, "Extensional Behavior of Multi-Crystalline Beams," *Report (University of California, Berkeley: Structural Engineering Mechanics and Materials)*, UCB/SEMM-92/20, 1992.

[5.9] Garboczi, E. J. and D. P. Bentz, "Computational Materials Science of Cement-Based Materials," *MRS Bulletin*, Vol. 18, No. 3, pp. 50–54, 1993.

[5.10] Gilbert, E. N., "Random Subdivision of Space into Crystals," *Annals of Mathematical Statistics*, Vol. 33, pp. 958–972, 1962.

[5.11] Huang, J., P. Krulevitch, G. C. Johnson, R. T. Howe, and H. R. Wenk, "Investigation of Texture and Stress in Undoped Polysilicon Films," *Materials Research Society Symposium Proceedings*, Vol. 182, pp. 201–206, 1990.

[5.12] Icke, V. and R. van de Weygaert, "Fragmenting the Universe I. Statistics of Two-dimensional Voronoï Foams," *Astronomy and Astrophysics*, Vol. 184, pp. 16–32, 1987.

[5.13] Kawasaki, K., T. Nagai, and K. Nakashima, "Vertex Models for Two-Dimensional Grain Growth," *Philosophical Magazine B*, Vol. 60, No. 3, pp. 399–421, 1989.

[5.14] Kumar, S., S. K. Kurtz, J. R. Banavar, and M. G. Sharma, "Properties of a Three-Dimensional Poisson-Voronoï Tesselation: A Monte Carlo Study," Journal of Statistical Physics, Vol. 67, Nos. 3/4, pp. 523–551, 1992.

[5.15] Le Caër, G. and J. S. Ho, "The Voronoï Tessellation Generated from Eigenvalues of Complex Random Matrices," *Journal of Physics A: Mathematical and General*, Vol. 23, pp. 3279–3295, 1990.

[5.16] Muche, L. and D. Stoyan, "Contact and Chord Length Distributions of the Poisson Voronoï Tessellation," *Paper presented at the Upsala Conference*, 1990.

[5.17] Mulheran, P. A., "On the Statistical Properties of the Two-Dimensional Random Voronoï Network," *Philosophical Magazine Letters*, Vol. 66, No. 5, pp. 219–224, 1992.

[5.18] Okabe, A., B. Boots, and K. Sugihara, *Spatial Tessellations—Concepts and Applications of Voronoï Diagrams*, John Wiley & Sons, Chichester, England, 1992.

[5.19] Russ, John C., *Practical Stereology*, Plenum Press, New York, 1986.

[5.20] Russ, J. C., "Image Analysis of the Microstructure of Materials," In: Williams, D. B., A. R. Pelton, and R. Gronsky (Eds.), *Images of Materials*, Oxford University Press, New York, 1991.

[5.21] Sakaue, K., "Image Processing Techniques for Grain Boundary Extraction," *ISIJ International*, Vol. 30, No. 7, pp. 475–481, 1990.

[5.22] Srolovitz, D. J., G. S. Grest, and M. P. Anderson, "Computer Simulation of Recrystallization—I. Homogeneous Nucleation and Growth," *Acta Metallurgica*, Vol. 34, No. 9, pp. 1833–1845, 1986.

[5.23] Stoyan, D. and H. Herman, "Some Methods for Statistical Analysis of Planar Random tessellations," *Statistics*, Vol. 17, No. 3, pp. 407–420, 1986.

[5.24] Stoyan, Dietrich, W.S. Kendall, and J. Mecke, *Stochastic Geometry and its Applications*, Wiley, Chichester, 1987.

[5.25] Stoyan, D. and H. Stoyan, "Exploratory Data Analysis for Planar Tessellations: Structural Analysis and Point Process Methods," *Applied Stochastic Models and Data Analysis*, Vol. 6, pp. 13–25, 1990.

[5.26] Stoyan, D., "Stereology and Stochastic Geometry," *International Statistical Review*, Vol. 58, No. 3, pp. 227–242, 1990.

[5.27] Stoyan, D. and K. Wiencek, "Spatial Correlations in Metal Structures and their Analysis," *Materials Characterization*, Vol. 26, No. 3, pp. 167–176, 1991.

[5.28] Takeuchi, T., "Automatic Repair of Defects in Grain Boundary Images," *ISIJ International*, Vol. 30, No. 7, pp. 482–489, 1990.

[5.29] Thiessen, A. H., "Precipitation Averages for Large Areas," *Monthly Weather Review*, Vol. 39, pp. 1082–1084, 1911.

[5.30] Tipper, J. C., "Fortran Programs to Construct the Planar Voronoï Diagram," *Computers & Geosciences*, Vol. 17, No. 5, pp. 597–632, 1991.

[5.31] Underwood, Ervin E., *Quantitative Stereology*, Addison-Wesley Pub. Co., Reading, Mass., 1981.

[5.32] Vaz, M. F., A. Soares, and M. A. Fortes, "Computer Simulation of Grain Growth in a Non-Equiaxed Polycrystal," *Scripta Metallurgica et Materialia*, Vol. 24, pp. 2453–2458, 1990.

[5.33] Weaire, D. and N. Rivier, "I would have to look up the title for this one," *Contemporary Physics*, Vol. 25, pp. 59–99, 1984.

[5.34] Wise, K. D., "Integrated Microelectromechanical Systems: A Perspective on MEMS in the 90s." *Proc. IEEE Microelectromechanical Systems*, Nara Japan, 1991, pp. 33–38.

[5.35] Zienkiewicz, O. C. and R. L. Taylor, *The Finite Element Method, Vol. 1*, McGraw-Hill, London, U.K., 1989.

Chapter 6

RANDOM FIELD MODELS

6.1 INTRODUCTION

The discrete model presented in Chapter 5 represents a direct form of analyzing the mechanical behavior of multicrystalline MEMS structures and is useful in providing insights into the phenomenological characteristics of the problem through a simulation approach. However, since the necessary finite element discretization requires the generation of a new mesh for each simulation, that approach is computationally intensive and has limited applicability. The results are dependent on load and displacement boundary conditions, grain sizes, and the beam geometry. Any change in these boundary conditions or parameters would require a complete re-analysis. Furthermore, the simulation approach can be prohibitively costly for computing small probabilities associated with extreme levels of performance.

Now, a more efficient approach, employing continuous-parameter random fields and stochastic finite elements is presented. Individual elastic moduli, such as the Young's modulus along one axis, E_i, or more generally, the elastic stiffness matrix coefficients, C_{ij}, are modeled as random fields.

This random field approach may aptly be termed "probabilistic smoothing." The mean of the random field corresponds to estimates obtained through traditional homogenization methods, e.g. the Hill estimate (§4.3). The random field model, however, includes additional information regarding the second-moment properties of the modeled properties. Using the random field approach, in addition to the mean structural response, the standard deviation of the response is found using only one stochastic finite element analysis. Furthermore, the probability that the response will exceed a given threshold is obtained by using just a few finite element analyses.

The following sections begin by introducing and briefly defining the notion of a "random field." This is followed by a brief outline of methods for the mathematical modeling of random fields based on observations, and their discretization for subsequent use with stochastic finite element methods. Next, an approach for the modeling of beam-like MEMS structures is described. The effective axial Young's modulus, $E_{eff}(x)$, is first modeled as a continuous-parameter random function of distance, x, along the beam axis. This is followed by the random field modeling of the second moment of area, $I(x)$, that results from the uncertain cross-sectional dimensions of the beam along its length. A more general random field approach is then introduced for 2-D and 3-D multicrystalline structures. The effective material stiffness matrix is modeled based on a continuous-parameter random field vector of crystal orientations, suitably transformed to reflect the existing texture using transformations developed in §4.1. Finally, details of the finite element implementation for the above random field models are delineated, including a discussion of the element characteristics.

6.2 RANDOM FIELDS

6.2.1 Definition

A random field is an indexed set of random variables $U(\mathbf{x})$, with the index $\mathbf{x}$ describing coordinates in a multi-dimensional space. Random fields are sometimes referred to as stochastic processes, however, the term "field" serves to indicate the multi-dimensional nature of the index space, usually defined in terms of one or more spatial coordinate axes, while, strictly speaking, the term stochastic process refers to a time-varying phenomenon.

Random fields can be continuous-parameter or discrete parameter. In this context, where x represents spatial coordinates, continuous values of the parameter set x are admissible, thus the resulting random fields are continuous-parameter. A realization of the field along an axis x, however, may be discontinuous, e.g. in the extreme case where a crystal boundary is *exactly* vertical across the depth of the whole beam when modelling $E_{eff}(x)$.

6.2.2 Mathematical Modeling

Random fields can be defined using various approaches, e.g. by their joint PDF, their joint characteristic function, or in terms of moment functions [6.7, 6.17]. For most practical purposes, however, the first- and second-moments, called the *mean function*, $\mu_U(\mathrm{x})$, and the *autocorrelation function*, $\phi_{UU}(\mathrm{x}_1, \mathrm{x}_2)$, respectively, suffice in describing random fields. This approach is pursued here.

The mean and autocorrelation functions are defined below using the first- and second-moment relations

$$\mu_U(\mathrm{x}) = \mathrm{E}\left[\mathrm{U}(\mathrm{x})\right] \tag{6.1}$$

$$\phi_{UU}(\mathrm{x}_1, \mathrm{x}_2) = \mathrm{E}\left[\mathrm{U}(\mathrm{x}_1)\,\mathrm{U}(\mathrm{x}_2)\right] \tag{6.2}$$

where E[.] indicates the expectation operator.

A random field is homogeneous in the strict sense if all of its finite-dimensional distributions are invariant with respect to a shift in the parameter origin. If the mean and autocorrelation functions are invariant, the random field is considered homogeneous in the wide sense [6.7]. For the cases considered here, homogeneity can be assumed in the wide sense. This implies a constant value for the mean function and allows the representation of the autocorrelation function as a function of a "difference" quantity, i.e., the length of the vector joining the two points $\mathbf{x}_1$ and $\mathbf{x}_2$. Thus,

$$\mu_U(\mathbf{x}) = \mu_U \tag{6.4}$$

$$\phi_{UU}(x_1, x_2) = R_{UU}(\chi) \tag{6.5}$$

where

$$\chi = \|\mathbf{x}_2 - \mathbf{x}_1\| \tag{6.6}$$

is the distane between the two points. We can also define the autocorrelation coefficient function as

$$\rho_{UU}(\chi) = \frac{R_{UU}(\chi) - \mu_U^2}{\sigma_U^2} \tag{6.7}$$

where

$$\sigma_U^2 = R_{UU}(0) - \mu_U^2 \tag{6.8}$$

represents the variance of the random field.

The objective here is to mathematically model the random fields of interest based on observations of the MEMS multicrystalline materials. Näther [6.11], Ramm [6.13], and Ivanov and Leonenko [6.7] have extensive studies on the observation, estimation, and statistical analysis of random fields, respectively. These references are comprehensive sources of methods that can be used to solve a large variety of problems. For homogeneous random fields, we can simply generate enough data to be able to estimate μ_U, σ_U, and $\rho_{UU'}(\chi)$.

For the case of modeling the effective axial Young's modulus, $E_{eff}(x)$, an approach suggested by Vanmarcke [6.17] is used to find the autocorrelation function (see §6.3.3). For modeling the effective material stiffness matrix, $\mathbf{C}(\mathbf{x})$, random field, a semi-analytical approach is employed for deriving the autocorrelation function (see §6.5.2).

6.2.3 Discretization

The random field models need to be discretized—i.e. be represented in terms of a finite number of random variables—in order to solve problems using finite elements. A random field such as $\mathrm{E}(\mathbf{x})$ can be represented through interpolation functions and nodal random variables following the Expansion Optimal Linear Estimation (EOLE) method of Li and Der Kiureghian [6.9].

Consider the following eigenvalue problem associated with the $n \times n$ covariance matrix Σ_{EE} of nodal values E_i of the Young's modulus random field $\mathrm{E}(\mathbf{x})$

$$\Sigma_{\mathrm{EE}} \phi_i = \theta_i \, \phi_i \tag{6.9}$$

where θ_i and ϕ_i are the eigenvalues and eigenvectors of the covariance matrix, respectively.

The EOLE method represents $\mathrm{E}(\mathbf{x})$ by the following sum

$$\hat{\mathrm{E}}(\mathbf{x}) = \mu_E + \sum_{i=1}^{r} \frac{\zeta_i}{\sqrt{\theta_i}} \phi_i^{\mathrm{T}} \Sigma_{\mathrm{E}(\mathbf{x})\mathrm{E}} \tag{6.10}$$

where μ_E is the mean-value of $\mathrm{E}(\mathbf{x})$, $r : r \leq n$ is the minimum number of terms required to accurately model the random field, $\Sigma_{\mathrm{E}(\mathbf{x})\mathrm{E}}$ is a column vector containing the covariances of $\mathrm{E}(\mathbf{x})$ with the nodal random variables E_i (computed from the known autocorrelation function), and ζ_i are a set of r

independent standard normal (zero mean, unit standard deviation) variates. This assumes the field is Gaussian.

§6.6.1 shows results comparing the EOLE-discretized random field stochastic finite element method with simulation results based on the discrete model of Chapter 5 for the case of multicrystalline beams. This discretization method is also applicable to 2- and 3-D random fields.

6.3 MODELING OF E(X)

6.3.1 Modeling Approach

The bending behavior of multicrystalline beams can be adequately predicted using a flexural rigidity characterization. The random crystalline structure results in a randomly varying effective bending stiffness, $EI_{eff}(x)$, expressed as a function of distance, x, where E represents the Young's modulus and I the second moment of area, I_{zz}, along the beam (see Fig. 6.1). A random field function that models $EI_{eff}(x)$ is saught. Assuming a constant value for I, the variations of $EI_{eff}(x)$ are then only due to the random arrangements of crystals and their uncertain orientations.

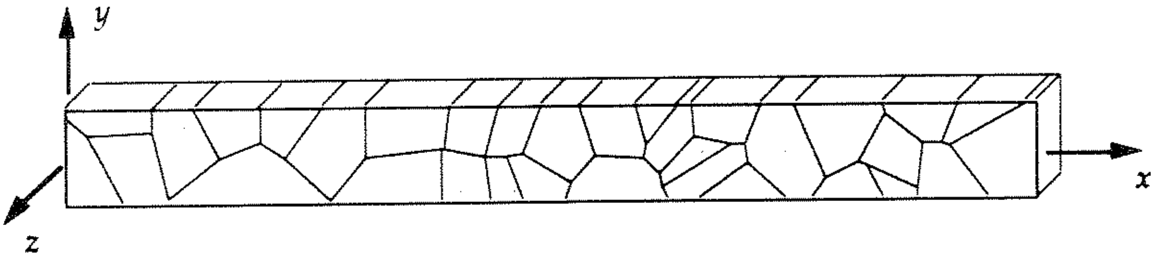

Fig. 6.1 Multicrystalline Beam Showing Axes

This section considers multicrystalline arrangements represented by Poisson Voronoï Diagrams (PVDs), as introduced in Chapter 5, in planar problems. The methodology, however, is applicable to any multicrystalline arrangements, including those empirically derived through image analysis techniques. It is also extendible to 3-D cases.

By defining a particular beam depth, *d*, and the intensity of the Poisson point process, λ, used to generate the PVD, the geometrical characteristics of the planar beam problem are fully defined. What remains is the information provided by the orientation distribution function, ODF. Assuming strong out-of-plane texture (see §4.5), the distribution of in-plane rotations, $f_\Psi(\psi)$, would give a complete description of the ODF.

Values for $E_{eff}(x)$ are generated by a moving window approach in fields of simulated crystals, with constant *I*, shown schematically in Fig. 6.2. The value for the effective Young's modulus is then evaluated for the window by finding the Young's modulus for a homogeneous and isotropic beam segment having depth *d* and width *W*. In the limit as the window width, *W*, tends to zero, this value can be considered to equal $E_{eff}(x)$. This concept is further described in §6.3.2.

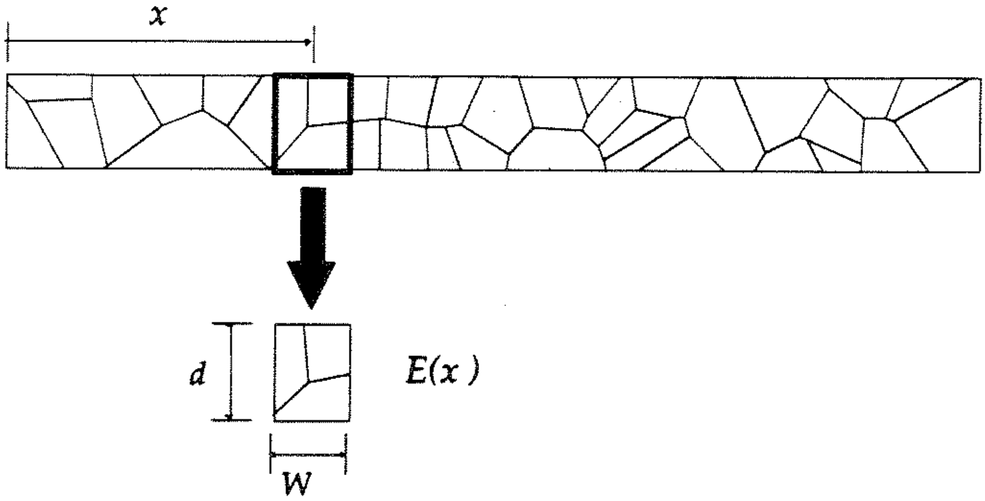

Fig. 6.2 Multicrystalline beam showing moving window

Fig. 6.3 illustrates three example PVD-based beams. Although these beams have different dimensions, they are scaled variations of just one multicrystalline beam. Clearly, the random field $E_{eff}(x)$ for these beams would be similar, with only a scaling factor to distinguish between them. To account for such scaling, a dimensionless problem description is now pursued so that the random fields may be more efficiently modelled.

A scale parameter, ζ, defined as

$$\zeta = d\sqrt{\lambda} \tag{6.11}$$

is introduced, where ζ is proportional to the mean number of crystals per cross-section. For Figs. 6.3(a), (b), and (c), ζ is equal to $\sqrt{3}$. Beam problems with PVD for crystal geometries are fully defined given ζ and $f_{\Psi}(\psi)$.

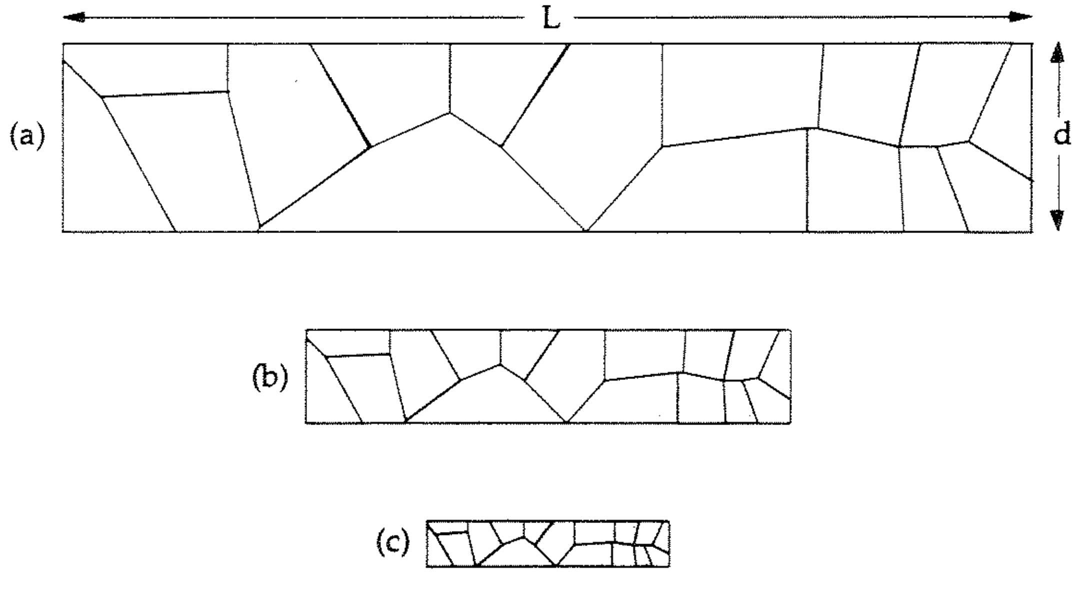

Fig. 6.3 Three Example PVD-Based Planar Multicrystalline Beams

The auto-correlation coefficient function of the random field $E_{eff}(x)$ resulting from a multicrystalline beam is found to be independent of the ODF (§6.3.4) for the case of uncorrelated crystal orientations. This implies a decoupling of the problem, such that the auto-correlation coefficient function is only a function of the problem geometry. This then enables the development of a general model for the auto-correlation function of $E_{eff}(x)$ as a function of ζ only. Although some sources report a certain degree of correlation between adjacent crystal orientations, the assumption of uncorrelated crystal orientations is still widely accepted and employed in material modeling and characterization. In applications where the adjacent crystal orientations are correlated, the auto-correlation function of $E_{eff}(x)$ will be a function of both ζ and higher-order textural characteristics of the material, such as the misorientation distribution function (§4.2.2).

The mean of the random field $E_{eff}(x)$ is found from the ODF. Due to the averaging performed at a section, the standard deviation is not geometry-independent. This is further illustrated in the following sections. An auto-correlation coefficient model for $E_{eff}(x)$ is used and fitted to observed data for simulated microstructures using the PVD model formulated in Chapter 5.

6.3.2 Evaluation of $E_{eff}(x)$ at a Section

In the following sub-sections, a numerical approach employing finite elements is first presented, followed by an analytical-geometric approach: both are aimed at evaluating the effective axial Young's modulus, $E_{eff}(x)$, at a section along the length of a multicrystalline beam.

6.3.2.1 Finite Element Derivation

A recent study by Wang [6.18] reports on the within-specimen variability in the modulus of elasticity for wood, where a "grading" machine is used to measure the bending deformations through a fixed loading pattern. Here, a similar idea is employed, but numerical "experiments" are conducted using two alternative methods: (a) subjecting a window along the multicrystalline beam to a uniaxial tension; and (b) subjecting the window to pure flexure. These loading conditions are shown in Fig. 6.4 together with the associated finite-element mesh, Fig. 6.4 (c), used in the numerical derivations described below.

For the beam in tension, as in Fig. 6.4 (a), the average strain, ε_{avg}, is calculated by measuring the average displacement of the right side of the window relative to the left and dividing by the width of the window. The stress state for the problem then enables the direct calculation of the effective Young's modulus for axial tension, E_T

$$E_T = \frac{\sigma_T}{\varepsilon_{avg}} \tag{6.12}$$

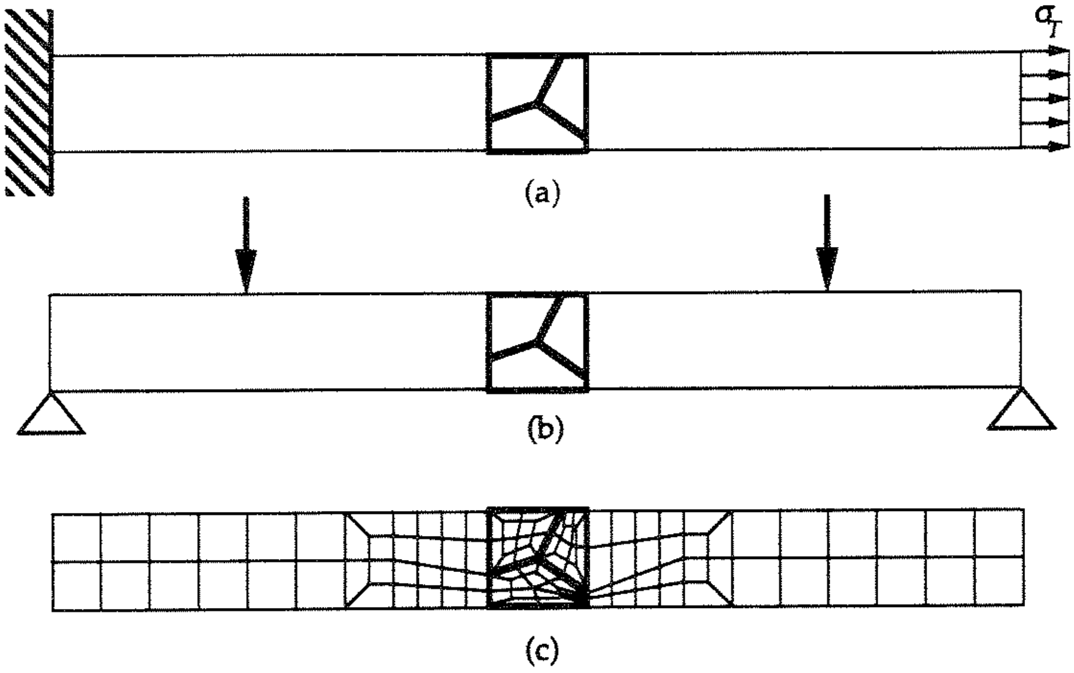

Fig. 6.4 Beam in Tension (a) and in Pure Flexure (b);
(c) Finite Element Mesh

For the beam in flexure, as in Fig. 6.4 (b), the state of strain is more complicated. We fit a plane section through the displaced nodal positions of the left and right sides of the window, imposing zero strain at mid-section. This is illustrated for a typical node in Fig. 6.5, noting that since strains in direction 2 are negligible, only displacements in direction 1 are considered. The slopes of the best fit lines, m_L and m_R, are found by minimizing the sum of the squares of the errors e_j on either side of the deformed window. These slopes define the average curvature, ϕ_{avg}, of the window

$$\phi_{avg} = \frac{1}{m_L} - \frac{1}{m_R} \tag{6.13}$$

and the effective Young's modulus for flexure, E_F, is then calculated according to the following relation

(6.14)

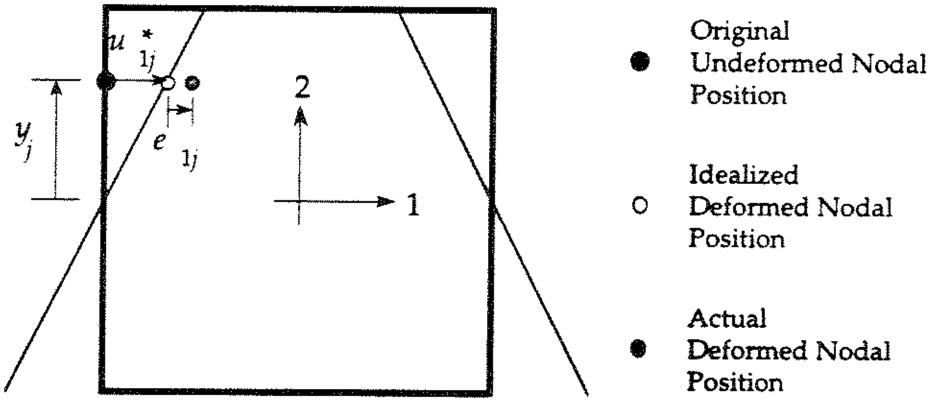

Fig. 6.5 Axial Deformation of a Typical Node

The above finite element procedures are cumbersome and computationally demanding, due to the repeated remeshings necessary for each window. However, they can serve to verify the accuracy of the more simplified techniques that are introduced next.

6.3.2.2 Analytic-Geometric Derivation

Here an "analytic-geometric" approach is pursued. At a section of a multicrystalline beam, the beam is composed of a finite number, n, of crystals, each with a distinct orientation angle. For each crystal, the axial Young's modulus, E_i, is defined in terms of the orientation angle, ψ_i, with respect to the beam axis.

The orientation-dependent axial Young's modulus, $E(\psi_i)$, for in-plane rotations, ψ_i, was derived for various texture states in §4.3 and is shown again below for the case of {100} texture:

$$E_i = E(\psi_i) = \frac{1}{a \cos 4\psi_i + b} \tag{6.15}$$

where a and b are constants related to C_{11}, C_{12}, and α as follows:

$$a = \frac{(\alpha - 1)}{4(C_{11} - C_{12})\alpha} \tag{6.16}$$

$$b = \frac{(3\alpha + 1)C_{11} + (1 - \alpha)C_{12}}{4(C_{11}^2 - C_{12}^2)\alpha} \tag{6.17}$$

where

$$\alpha = \frac{2\,C_{44}}{(C_{11} - C_{12})} \tag{6.18}$$

The effective Young's modulus for a section may be approximated as a weighted average of the n E_is. A simple approach would be to weight the contributing E_is according to the relative areas, A_i, that the corresponding crystals occupy in a window. This would give an appropriate answer if the window was being subjected to a uniform tension. For the case of flexure, not only do the sizes of the crystals count, but so do their positions relative to the neutral axis of the beam at that section.

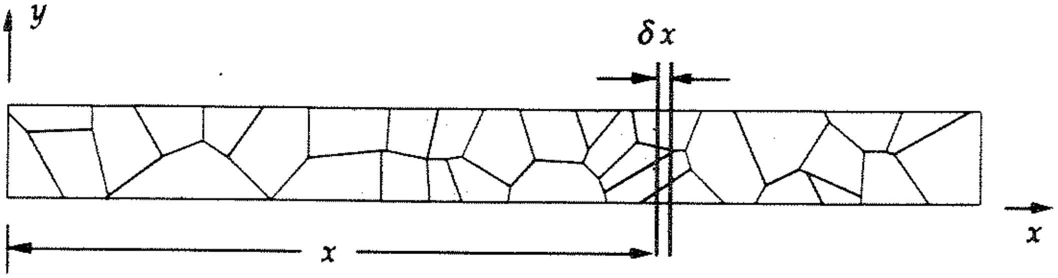

Fig. 6.6 Vertical "Slice" Taken Along a Multicrystalline Beam

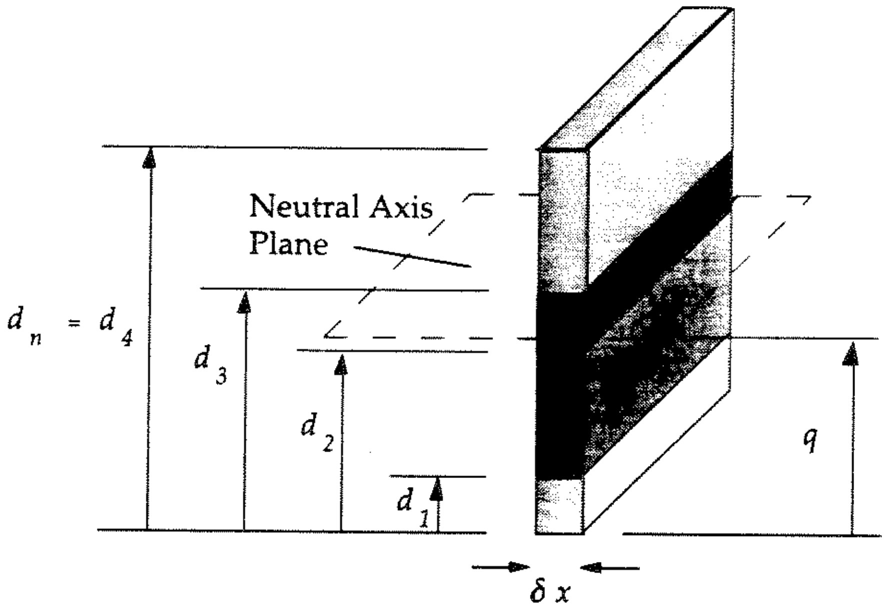

Fig. 6.7 Cross-section of Vertical "Slice"

Considering a multicrystalline window with n crystals, an approximation for the effective window axial Young's modulus, E_W, is:

$$E_W \approx \frac{1}{A_{Total}} \sum_{i=1}^{n} A_i E(\psi_i) \tag{6.19}$$

where $E(\psi_i)$ is as defined in Eq. 6.15, A_i are the individual crystal areas within the window, and A_{Total} is the sum of all A_i, equal to the area of the widow. The expression for E_W reduces to $E_{eff}(x)$ at a section as $W \to 0$

$$E_{eff}(x) \approx \frac{1}{d_n}\sum_{i=1}^{n}(d_i - d_{i-1})E(\psi_i) \tag{6.20}$$

with d_i defined in Fig. 6.7.

Considering a vertical "slice" taken along a multicrystalline beam, as shown in Fig. 6.6, this would reduce to a "section" in the limit as the slice width, δx, tends to zero. A typical slice is shown schematically in Fig. 6.7. It is composed of n crystals, each with its top surface a distance d_i from the x axis, and with its distinct in-plane crystallographic orientation, ψ_i, and corresponding axial Young's modulus, $E(\psi_i)$, as derived from Eq. 6.15 (note that $d_0 = 0$). This section is thus made up of n distinct materials with different values for their Young's moduli. The different shadings in Fig. 6.7 serve to indicate the different material properties.

Using the transformed cross-sectional area approach [6.12], $E_{eff}(x)$ for flexure is given by the following expression

$$E_{eff}(x) = \frac{12}{d_n^3}\sum_{i=1}^{n}\left[d_i\left(q^2 - d_i q + d_i^2/3\right) - d_{i-1}\left(q^2 - d_{i-1}q + d_{i-1}^2/3\right)\right]E_1(\psi_i) \tag{6.21}$$

where, the height of the neutral axis, q, above the x axis is given by

$$q = \frac{\sum_{i=1}^{n}\left(d_i^{\,2} - d_{i-1}^{\,2}\right)E_1(\psi_i)}{2\sum_{i=1}^{n}\left(d_i - d_{i-1}\right)E_1(\psi_i)} \tag{6.22}$$

Comparing the axial and flexural approaches, Eqs. 6.20 & 6.21, we note that the general analytical-geometrical expression for $E_{eff}(x)$ is

$$E_{eff}(x) = \sum_{i=1}^{n} w_i\, E\,(\psi_i) \tag{6.23}$$

where, w_i, are the weights given by

$$w_i = \frac{(d_i - d_{i-1})}{d_n} \tag{6.24}$$

for the tension case, and

$$w_i = \frac{12}{d_n^3}\left[d_i\left(q^2 - d_i q + d_i^2/3\right) - d_{i-1}\left(q^2 - d_{i-1} q + d_{i-1}^2/3\right)\right] \tag{6.25}$$

with q defined in Eq. 6.22 for the case of flexure. An example problem is shown in §6.6.1 where the above geometric idealization is used in defining $E_{eff}(x)$. The results of beam deflections using this approach are shown to compare well with the multicrystalline finite element model.

6.3.3 Modeling and Identification of the Auto-Correlation Function

Using the procedure described in the previous section, realizations of the random field of the effective Young's modulus, $E_{eff}(x)$, along a multicrystalline beam are computed. One such realization using the flexural assumption is shown in Fig. 6.8. This is obtained by assigning a set of uniformly distributed in-plane orientation angles, U(0,π), for the constituent {100} crystals. By generating an ensemble of such realizations, statistical characteristics of the random field such as the mean, variance and the auto-correlation function may be estimated.

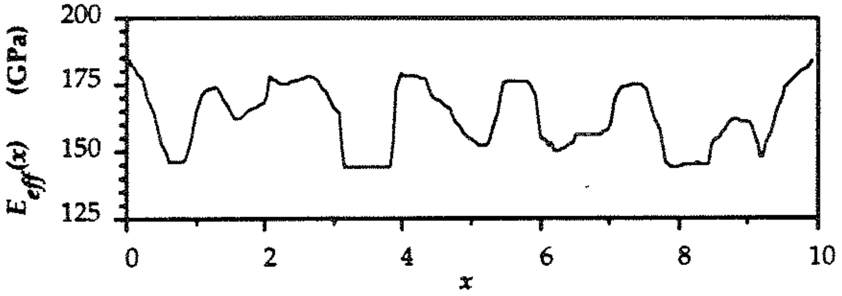

Fig. 6.8 Effective Young's Modulus vs. Beam Position

Use can be made of various existing models for describing the statistics of the random field. Here, use is made of a class of models introduced by Vanmarcke [6.17] that is appropriate in this context.

6.3.3.1 Local Average Fields

The effective Young's modulus, or any other material property, obtained as realizations of a random field using the windowing method outlined previously is a *moving average* field. From a continuous parameter stationary random field $E(x)$ with mean μ and standard deviation σ, a family of moving average fields $E_W(x)$ can be derived by [6.17]:

$$E_W(x) = \frac{1}{W}\int_{x-W/2}^{x+W/2} E(u)\,du \tag{6.26}$$

where W denotes the window width or averaging length.

Properties of moving average fields are based on the parent, or point-to-point random field. For a homogeneous random field, the mean is not affected by the averaging operation; however, the variance of $E_W(x)$ is, given by

$$\mathrm{Var}[E_W] = \sigma_W^2 = \gamma(W)\sigma^2 \tag{6.27}$$

where $\gamma(W)$, denoting the *variance function* of $E(x)$, is a dimensionless function measuring the reduction of the point variance under local averaging. In the limit as W tends to infinity, the expression $W\gamma(W)$ approaches a constant value, θ, known as the *scale of fluctuation* [6.17].

The covariance function, $B_W(\chi)$, of local average fields is given by:

$$B_W(\chi) = \frac{\sigma^2}{2W^2}\left[\Delta(W+\chi) - 2\Delta(\chi) + \Delta(W-\chi)\right] \tag{6.28}$$

where $\Delta(W) = W^2\gamma(W)$. Thus knowing $\gamma(W)$ and σ of the parent random field, the covariance function, and hence the autocorrelation coefficient function, $\rho_W(\chi) = B_W(\chi) / \sigma_w{}^2$, of a moving average field such as the one produced by the windowing method previously outlined can be derived for different values of W using Eq. 6.28. The $\rho_W(\chi)$ for the point-to-point random field is found as W approaches zero. For practical problems, a value of $W \leq \theta/10$ is sufficiently small and can be used to define the point-to-point autocorrelation function.

6.3.3.2 Variance Function Model

Use is now made of a family of models for the variance function, $\gamma(W)$, described by Vanmarcke [6.17] as:

$$\gamma_m(W) = \left[1 + \left(\frac{W}{\theta}\right)^m\right]^{-1/m} \tag{6.29}$$

Substituting for $\gamma(W)$ in Eq. 6.28, we obtain an analytical expression for the moving average correlation function for a given window width W as shown below:

$$\begin{aligned} B_W(\chi) = \frac{\sigma^2}{2W^2}\Bigg\{ &(W+\chi)^2\left[1+\left(\frac{|W+\chi|}{\theta}\right)^m\right]^{-1/m} \\ &-2\chi^2\left[1+\left(\frac{|\chi|}{\theta}\right)^m\right]^{-1/m} \\ &+(W-\chi)^2\left[1+\left(\frac{|W-\chi|}{\theta}\right)^m\right]^{-1/m}\Bigg\} \end{aligned} \tag{6.30}$$

Thus, given θ, m, and σ the correlation function for a specified W is fully defined. The set of values $\{\theta, m, \sigma\}$, as well as the mean, μ, of the random field, can be empirically estimated from the generated data for various values of the parameter ζ, derived earlier. The estimation of μ and σ is clear and the following subsection describes the estimation of θ and m.

6.3.3.3 Empirical Estimation of θ and m

As $W \to 0$, $\sigma_W^2 \to \sigma^2$. Therefore $\gamma(W)$ can be approximated using the relation $\gamma(W) \approx \sigma_W^2 / \sigma_{small\ W}^2$ (based on Eq. 6.27). Also, as W becomes large, Eq. 6.29 implies that $\gamma(W) \to \theta/W$. Therefore by plotting $W\ \gamma(W)$ vs. W, the asymptotic value of θ can estimated. This is illustrated in Fig. 6.9 for an example beam with d = 1 and λ = 3 (i.e. $\zeta = \sqrt{3}$). The value for $W\gamma(W)$ converges rapidly and the scale of fluctuation, θ, is found to be approximately equal to 0.56 for this example.

To find m, the model variance function, $\gamma_m(W)$, is fitted to the observed variance function, $\gamma(W)$, through a least squares method, where $|\gamma_m(W) - \gamma(W)|^2$ is minimized for the set of data points corresponding to different Ws. Fig. 6.10 shows the best fit with m = 2.5 as a dotted line.

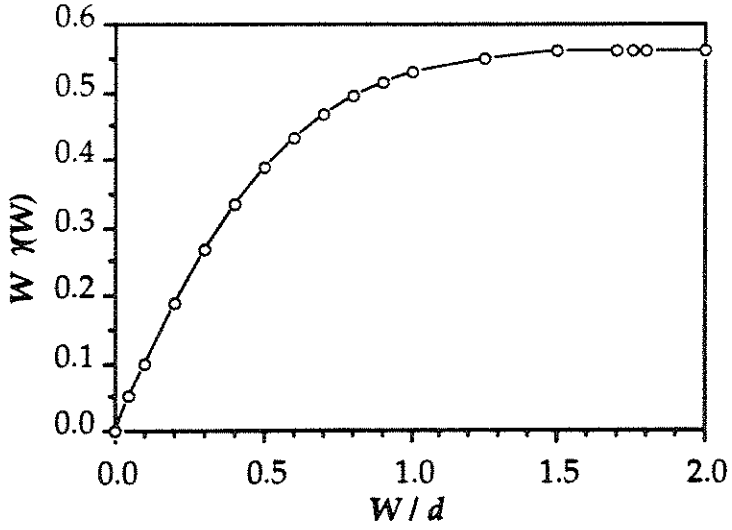

Fig. 6.9 Convergence of $W\gamma(W)$ to θ

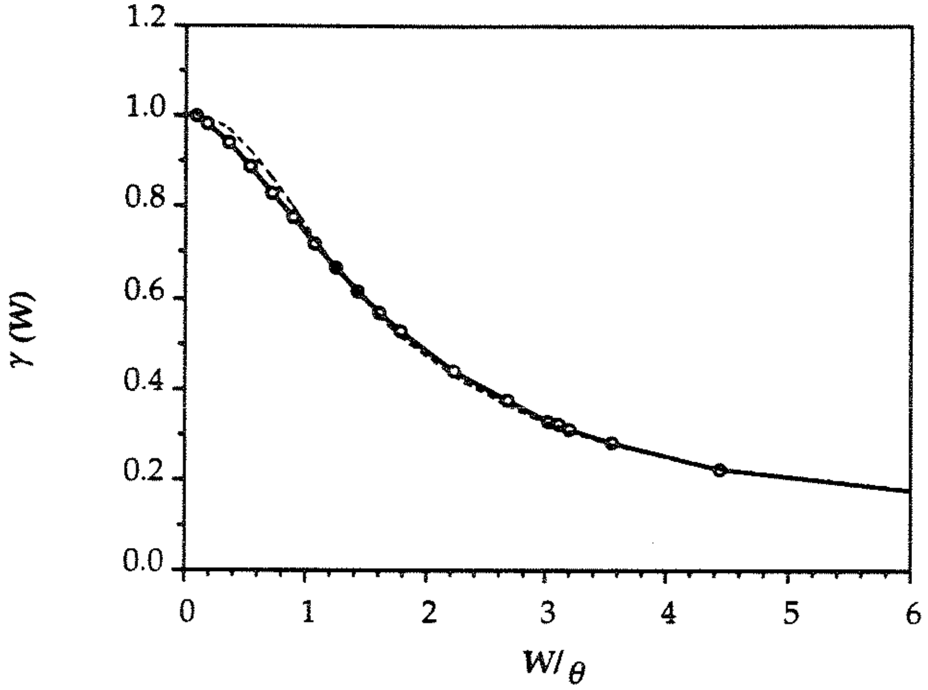

Fig. 6.10 Actual and Model $\gamma(W)$ vs. W/θ

6.3.3.4 Summary of Procedure

Random multicrystalline beams are first generated based on the Poisson point process and their associated Voronoï tessellation. Random orientation angles are then assigned to each crystal based on a prescribed ODF which reflects the texture present in the material.

Flexural rigidity is assumed to be the dominant quantity defining the bending behavior of long beams. The effective Young's modulus at a section is evaluated using area-weighted approximations of Eqs. 6.20 & 6.21 (see §6.6.1 for comparison with "exact" finite element solutions).

Taking moving averages of successive "points" of the data to represent windows of increasing width, the scale of fluctuation, θ, is estimated as shown in Fig. 6.9. This is then used to model the variance function, $\gamma(W)$, with Eq. 6.29, using a least squares fit.

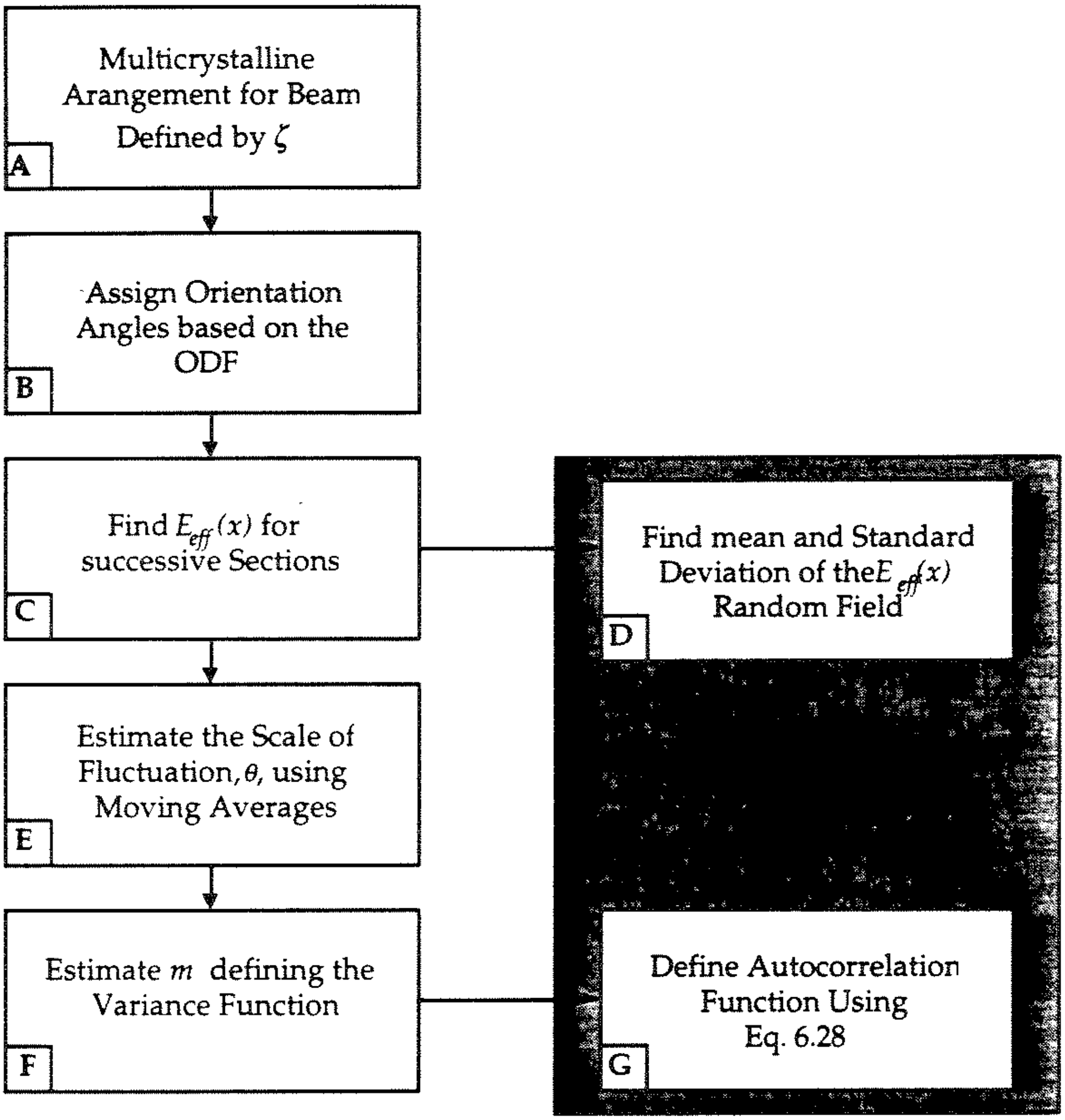

Fig. 6.11 Flow Chart Showing the Procedure for Modeling the Random Field

Having established values for $\{\theta, m, \sigma\}$, Eq. 6.30 is used as the analytical expression defining the auto-correlation function of the moving window random field, shown schematically in Fig. 6.2. The above procedure is summarized in the flow chart shown in Fig. 6.11.

6.3.4 Texture and Grain Size Effects

By following the procedure summarized in §6.3.3.4, values for θ, m, σ, and μ are established from an ensemble of point-to-point samples of effective Young's moduli, which define the stationary process, $E_{eff}(x)$, for the selected crystal grain structure (defined by $\zeta = d\sqrt{\lambda}$) and associated ODF.

A representative set of results are summarized in Table 6.1, defining the covariance function (Eq. 6.30) for each case. U(a,b) indicates the uniform distribution, with limits a and b, and N(μ,σ) indicates a normal distribution with mean μ and standard deviation σ which is truncated outside of the interval $(-\pi,\pi)$ and then normalized. Increased values of λ indicate higher densities of crystals, i.e. smaller crystals within the beam. For U(0,π) ODFs, μ = 164.3 GPa.

Table 6.1 Effects of Texture and Average Grain Size on $\{\theta,m,\sigma\}$

$\zeta = d\sqrt{\lambda}$	ODF	m	σ (GPa)	θ
1	U(0,π)	2.5	13.02	0.9718
√3	U(0,π)	2.5	11.94	0.5626
3	U(0,π)	2.5	10.74	0.2663
√3	N(0,π/8)	2.5	10.89	0.5195
√3	N(0,π/40)	2.5	1.01	0.5929

In the following sub-sections, the effects of the ODF and grain size on the random field characteristics of $E_{eff}(x)$ are assessed in turn.

6.3.4.1 Texture Dependence

The results in Table 6.1 show examples with the following ODFs: uniform distribution, U(0,π), and two different truncated normally distributed textured cases, N(0,π/8) and N(0,π/40) respectively. It is observed that values for *m* are identical in all cases. Furthermore, for equal ζ values ($\zeta = \sqrt{3}$), the scale of fluctuation, θ, is nearly the same, indicating independence of this parameter from texture. The standard deviations, σ, however, vary significantly as do the means (not shown here). Variations in σ do not affect the shape of the covariance function and only have a scaling effect. The similarities between these cases are seen more clearly by looking at plots of the autocorrelation coefficient functions in Fig. 6.12.

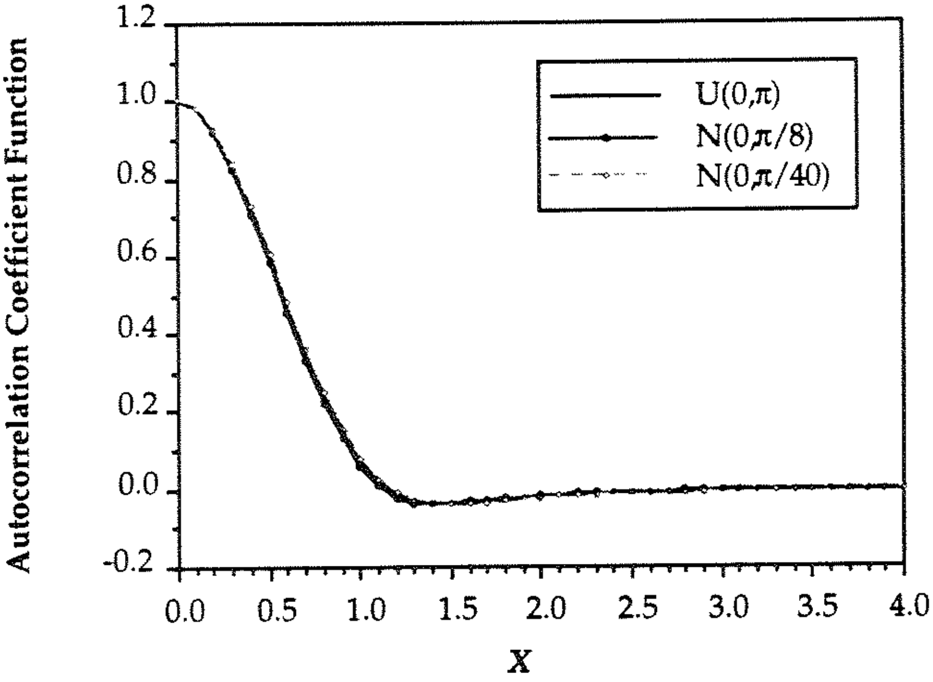

Fig. 6.12 Comparison of Autocorrelation Coefficient Functions

The functions are sufficiently close for us to conclude that the autocorrelation coefficient function is insensitive to the ODF. This result is valid if the crystal orientations are uncorrelated. Thus, the autocorrelation coefficient function appears to depend only on the geometry of the problem. On the other hand, the mean and standard deviation are strongly affected by texture.

6.3.4.2 Grain Size Dependence

Using a uniform ODF, U(0,π), but with different grain sized beams (varying λ and keeping d constant), insight is gained into the effects of relative grain size on the defining characteristics of the random field representation. These results are summarized in Table 6.1 for the cases $\zeta = 1, \sqrt{3}$, and 3.

Beams with increasing λ, have an increasing average number of crystal grains per cross-section. The standard deviation, σ, of the random field is reduced with increasing λ, since the effective modulus is now averaged over a larger number of crystals. The mean, μ, is dependent on the mean of the ODF.

The scale of fluctuation, θ, is seen to reduce with increasing ζ. It seems appropriate to associate θ with the average width of individual crystals measured along the beam, i.e using the inverse of $\sqrt{\lambda}$. Fig. 6.13 shows a clear trend for the U(0,π) results taken from Table 6.1. Typical realizations $E_{eff}(x)$ for $\zeta = 1, \sqrt{3}$, and 3 are shown in Fig. 6.14.

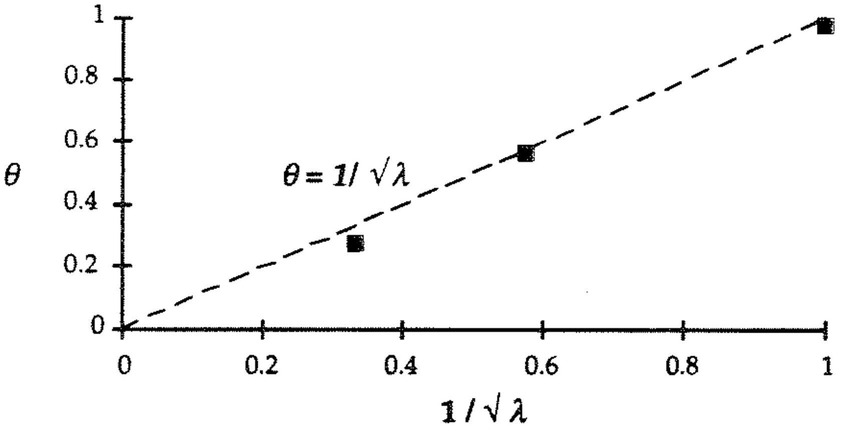

Fig. 6.13 Scale of Fluctuation, θ, vs. $1/\sqrt{\lambda}$

6.4 MODELING OF I(x)

The micro-fabrication process can result in an irregularly shaped beam cross section [6.20], as illustrated in the scanning electron micrograph (SEM) in Fig.

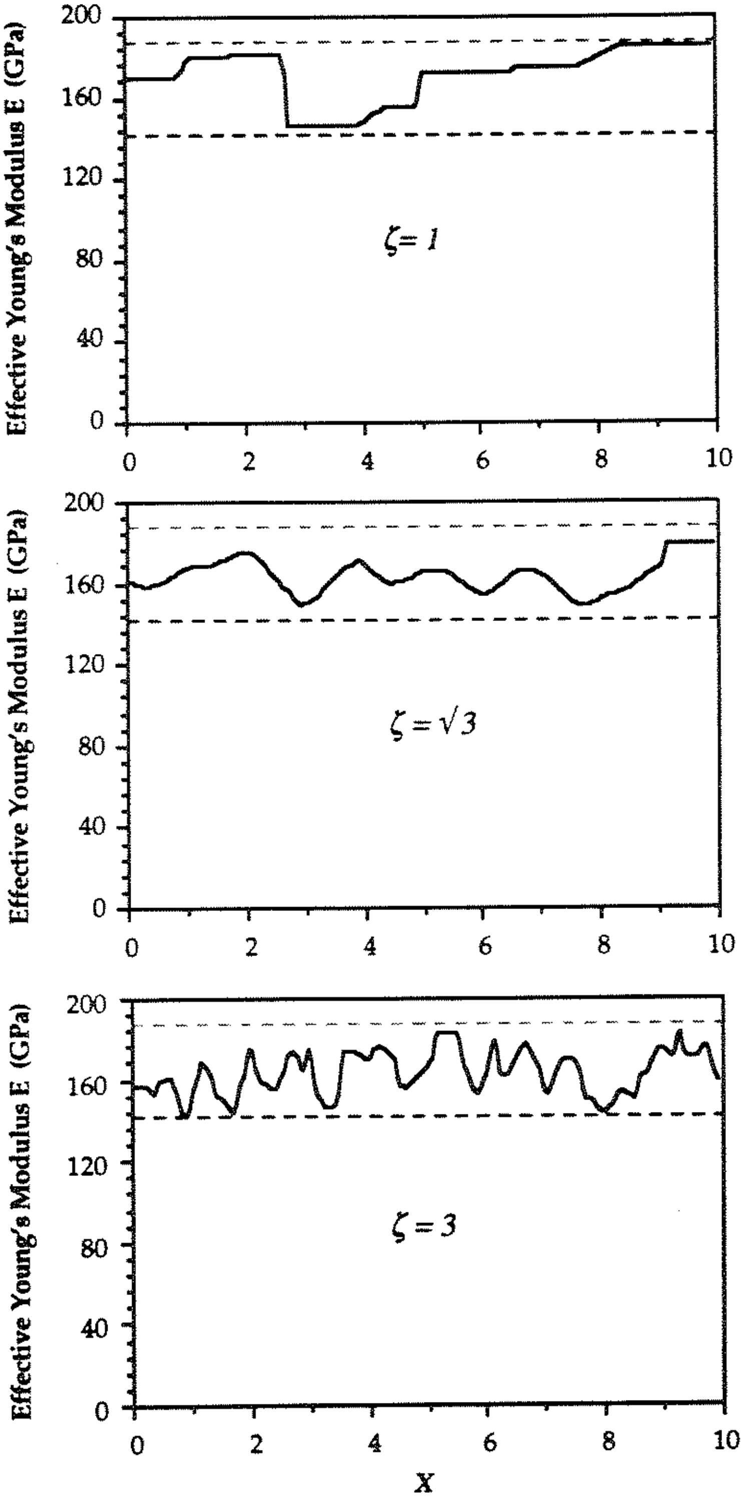

Fig. 6.14 Typical Realizations of the point-to-point $E_{eff}(x)$ for $\zeta = 1, \sqrt{3}$, and 3

6.15. These cross-sectional variations are idealized schematically in Figs. 6.16 and 6.17. Additionally, as shown in Fig. 6.18, the cross section can be non-rectangular [6.15]. The thickness variabilities are small and are assumed to be negligible when compared with the width variations. This results from the fabrication process (see §2.1) where the deposition stage (establishing film thickness) is more controlled than the plasma etch that "cuts" beam edges. The unevenness of the etch, however, can change from laboratory to laboratory and needs to be assessed before any detailed modeling considerations are made.

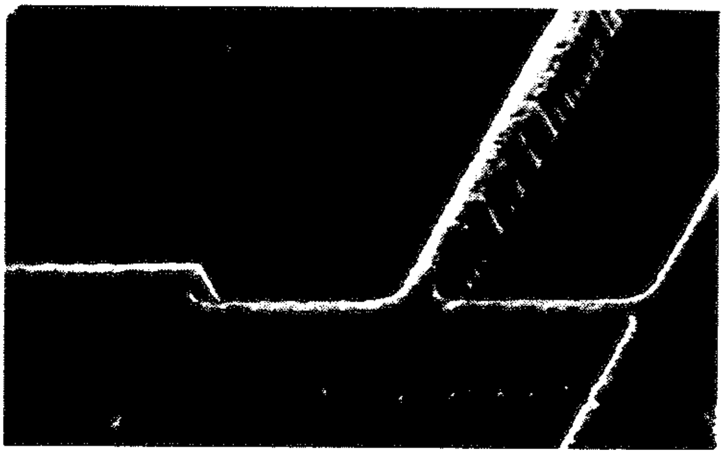

Fig. 6.15 SEM Showing Unevenness of the Etch

The irregularities in the beam cross-section result in the second moment of inertia being a random function of distance along the beam. Denoted by *I(x)*, it can be expressed as

$$I(x) = \frac{t}{24} w_c(x) \left[2 w_c^2(x) + \frac{1}{2} w_\Delta^2 \right] \tag{6.31}$$

where t is the film thickness, w_Δ is the difference in the top and bottom beam widths (taken to be constant since the variations in etch angle are negligible along the beam), and $w_c(x)$ is given by

$$w_c(x) = \mu_{wc} + w_{uc}(x) + w_{lc}(x) \tag{6.32}$$

where μ_{wc} is the mean value of beam width in the central 'slice,' and $w_{uc}(x)$ and $w_{lc}(x)$ are zero-mean functions shown schematically in Fig. 6.17.

A nominal beam width is assigned for the value of μ_{wc} and the random fields represented by $w_{uc}(x)$ and $w_{lc}(x)$ are taken to be identical but independently distributed zero-mean functions with the same standard deviation and autocorrelation function. The following autocorrelation function is assigned for w_{uc} and w_{lc}

$$\rho_{ww}(\Delta x) = \exp\left[-\left(\frac{\Delta x}{a}\right)^2\right] \tag{6.33}$$

where, Δx is the distance between any two points along the beam axis and a is the correlation length.

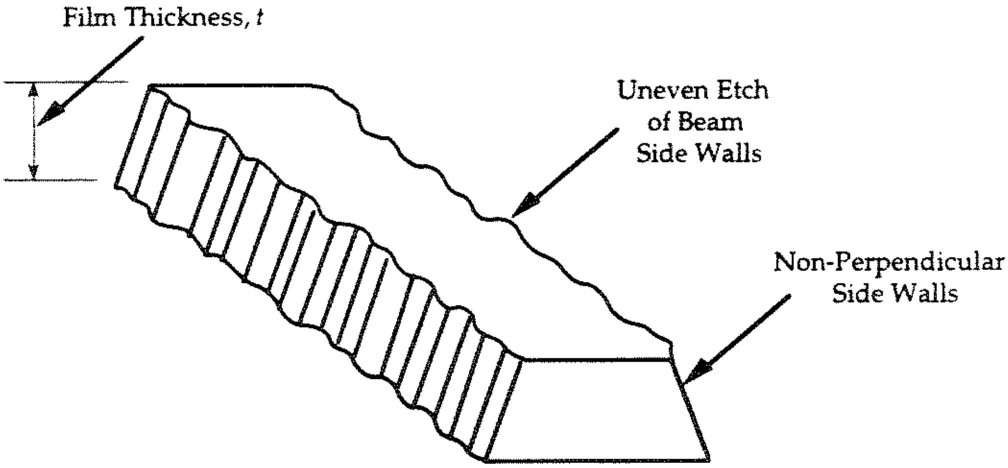

Fig. 6.16 Irregularities in Beam Cross-Section

The parameters in the above model, μ_{wc} and the mean, standard deviation, and correlation length, a, of the unevnness can be estimated from SEM observations of typical beams.

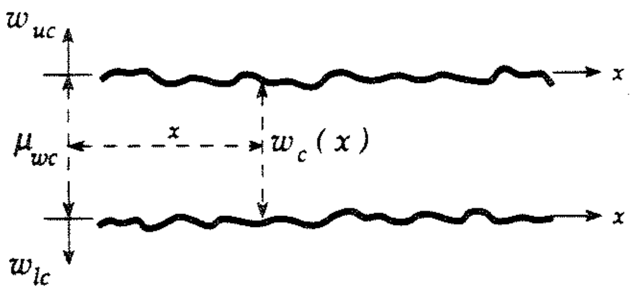

Fig. 6.17 Horizontal 'Slice' Through Length of Beam

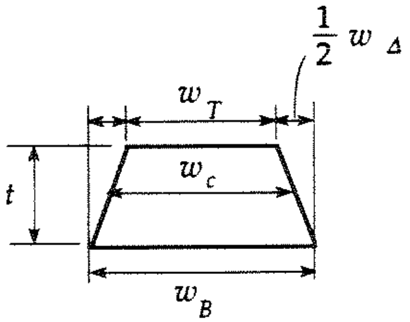

Fig. 6.18 Non-Rectangular Beam Cross-Section

6.5 RANDOM FIELD MODELING OF THE STIFFNESS TENSOR

In this section, we model the multicrystalline material stiffness properties as a 2D or 3D random field. First, the transformed generalized Hooke's Law from §4.1 is reintroduced. The discrete multicrystalline arrangements introduced in Chapter 5 are used to represent the structure of large-grained polycrystalline silicon samples. The elastic properties of each crystal are differentiated from others based on their distinct crystallographic orientation with respect to some global coordinate axes. The orientation variations in space are modeled as a vector random field $\boldsymbol{\psi}(\mathbf{x})$, where $\boldsymbol{\psi} = (\psi, \theta, \Phi)^T$ denotes the vector of Euler angles at each location $\mathbf{x}$ [6.1]. The elastic stiffness random field matrix is then found by defining the stiffness matrix, $\mathbf{C}$, as $\mathbf{C} = \mathbf{C}\ [C_{11}, C_{12},$

C_{44}, $\psi(x)$], where C_{11}, C_{12}, and C_{44} are the known elastic constants defined in the crystal-fixed frame. Finally, the model is related to the developments in §6.3, where the random field, $E_{eff}(x)$, was found for beam structures.

6.5.1 Rotationally Transformed Elastic Stiffness Matrix

The transformed generalized Hooke's Law, relating the elastic stresses and strains in a co-ordinate system different from the crystal-fixed frame has previously been defined in §3.35 as

$$\sigma_{ij} = C^*_{ijkl}\,\varepsilon_{kl} \tag{6.34}$$

where C^*_{ijkl} is the transformed stiffness tensor. The more convenient matrix representation was also defined, relating the stress and strain vectors σ^T = (σ_{11}, σ_{22}, σ_{33}, σ_{23}, σ_{13}, σ_{12}) and ε^T = (ε_{11}, ε_{22}, ε_{33}, $2\varepsilon_{23}$, $2\varepsilon_{13}$, $2\varepsilon_{12}$) respectively:

$$\sigma = \mathbf{C}^* \varepsilon \tag{6.35}$$

where the superscript 'T' stands for the transpose and $\mathbf{C}^*$ is the transformed 6x6 stiffness matrix. $\mathbf{C}^*$ is found using the transformation relation [6.16]:

$$\mathbf{C}^* = \mathbf{Q}\,\mathbf{C}^*\mathbf{Q}^T \tag{6.36}$$

where Q is the rotation matrix defined in terms of the direction cosines of angles between the global and crystal-fixed coordinate axes.

In the crystal-fixed coordinate axes, the stiffness matrix, **C**, for crystals with cubic symmetry reduces to a simple form shown in Eq. 6.37 [6.8]. Elements of $\mathbf{C}^*$ are thus fully defined, using the transformation relation, Eq. 6.36, in terms of the constants C_{11}, C_{12}, C_{44}, and the crystal orientation relative to the global coordinate axes. These angles are derived from the three Euler angles [6.1] (see §4.5).

$$\mathbf{C} = \begin{bmatrix} C_{11} & C_{12} & C_{12} & 0 & 0 & 0 \\ C_{12} & C_{11} & C_{12} & 0 & 0 & 0 \\ C_{12} & C_{12} & C_{11} & 0 & 0 & 0 \\ 0 & 0 & 0 & C_{44} & 0 & 0 \\ 0 & 0 & 0 & 0 & C_{44} & 0 \\ 0 & 0 & 0 & 0 & 0 & C_{44} \end{bmatrix} \tag{6.37}$$

Restricting our discussion to plane problems, the Euler angles reduce to just one angle ψ in the plane. The elasticity matrix random field $\mathbf{C}^*(\mathbf{x})$ for silicon is then fully defined by C_{11}, C_{12}, C_{44} and $\psi(x)$, through Eq. 6.36.

For example, as was shown in §4.4, the transformed stiffness matrix, $\mathbf{C}^*$, for {100} texture is defined as

$$C^* = \frac{1}{4}\begin{bmatrix} [1-\cos(4\psi)]U+4C_{11} & -[1-\cos(4\psi)]U+4C_{12} & 4C_{12} & 0 & 0 & U\sin(4\psi) \\ -[1-\cos(4\psi)]U+4C_{12} & [1-\cos(4\psi)]U+4C_{11} & 4C_{12} & 0 & 0 & -U\sin(4\psi) \\ 4C_{12} & 4C_{12} & 4C_{11} & 0 & 0 & 0 \\ 0 & 0 & 0 & 4C_{44} & 0 & 0 \\ 0 & 0 & 0 & 0 & 4C_{44} & 0 \\ U\sin(4\psi) & -U\sin(4\psi) & 0 & 0 & 0 & [1+\cos(4\psi)]U+2V \end{bmatrix} \tag{6.38}$$

where

$$U = -C_{11} + C_{12} + 2C_{44} \tag{6.39}$$

and

$$V = C_{11} - C_{12} \tag{6.40}$$

6.5.2 Random Field of Multicrystalline Orientations

To characterize the variations in ψ, the mean, μ_ψ, standard deviation, σ_ψ, and the autocorrelation function, $\rho_{\psi\psi}(x_1,x_2)$, need to be established for the material under consideration. The problem can be divided into two parts: (i) geometrical—where the multicrystalline geometry has influence on the results; and (ii) ODF related—where the orientation distribution function affects the characteristics of the random field. For uncorrelated crystal orientations, (i) alone defines $\rho_{\psi\psi}(x_1,x_2)$, while (ii) defines μ_ψ and σ_ψ. As in §6.3, the discussion will be restricted to these cases.

Consider a linear probe intersecting a multicrystalline structure (Fig. 6.19). Each intersected crystal is identified by the bounding intersection points along the linear probe and by its associated orientation angle, ψ. Plotting this orientation angle variation as a function of distance along the probe produces a square-wave function (see Fig. 6.20).

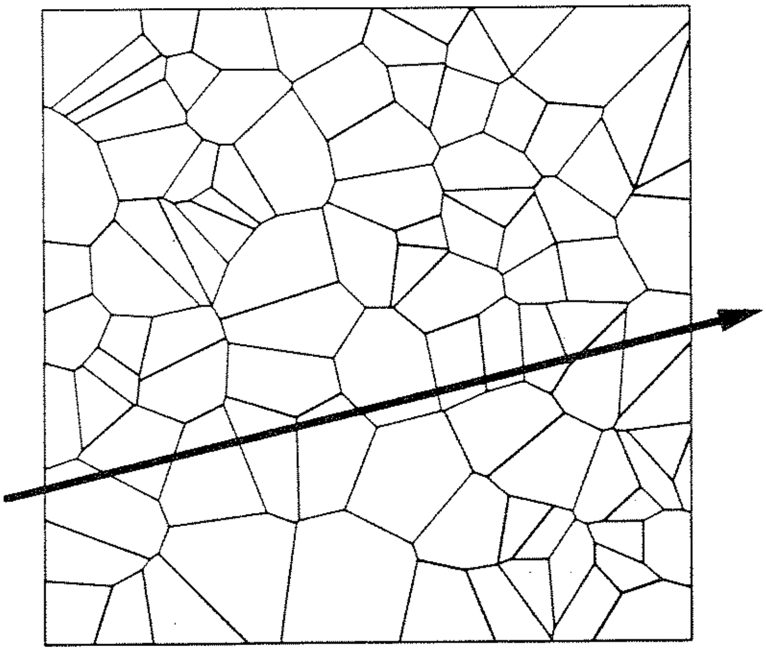

Fig. 6.19 Linear Probe in a Planar Multicrystalline Micro-structure

Generally, geometric studies of the multicrystalline structure are needed to define $\rho_{\psi\psi}(x_1,x_2)$. Here, studies are made of a previously defined model representing a random multicrystalline arrangement in the plane—the Poisson Voronoï diagram (PVD). The ensuing discussion is cast in general form so that it can be easily extended to any spatial multicrystalline arrangements.

An m-dimensional PVD may be intersected by an s-dimensional hyper plane H_s ($1 \leq s < m$) producing a structure called a sectional PVD denoted by $V_P(s,m)$. With $s = 1$ one obtains linear probes. An example of the intersection points obtained for $V_P(1,2)$ is shown in Fig. 6.20 (a).

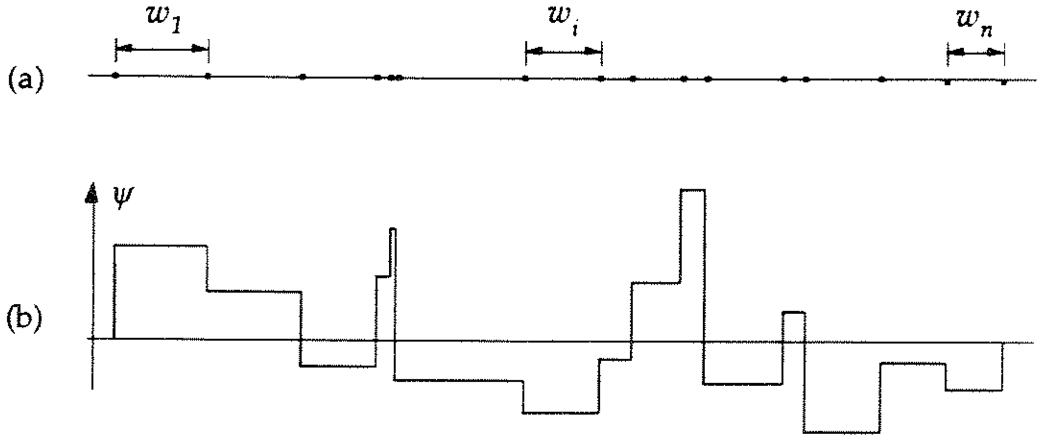

Fig. 6.20 (a) Example Realization of Intercept Point Process $V_P(1,2)$; (b) Associated Square-Wave Function for Orientation Angles

For $V_P(1,2)$, the mean and mean square of the chord lengths, w, have been established as $\pi/(4\sqrt{\lambda})$ and $0.804/\lambda$ respectively by Gilbert [6.6], where λ is the intensity of the Poisson point process. The PDF of w has been obtained by Muche and Stoyan [6.10] through simulations and is shown in Fig. 6.21 together with an approximate fitted analytical model defined by:

$$f_W(w) = \frac{1}{\sqrt{2\pi}\sigma}\left\{\exp\left[-\frac{1}{2}\left(\frac{w-\mu}{\sigma}\right)^2\right] + \exp\left[-\frac{1}{2}\left(\frac{w+\mu}{\sigma}\right)^2\right]\right\}, \quad 0 < w \qquad (6.41)$$

with parameter values $\mu = 0.75\mu_w$ and $\sigma = 0.464\mu_w$, where μ_w is the mean of w. A similar model can be fitted for $V_P(1,3)$, i.e. a linear probe in a 3-D PVD. Again, the values for the mean and mean square of the widths, w, have been established [6.6]. For non-Voronoï multicrystalline geometries, the PDF can be empirically derived through observations of the microstructural geometry, e.g. through image analysis and stereological studies (see §5.1).

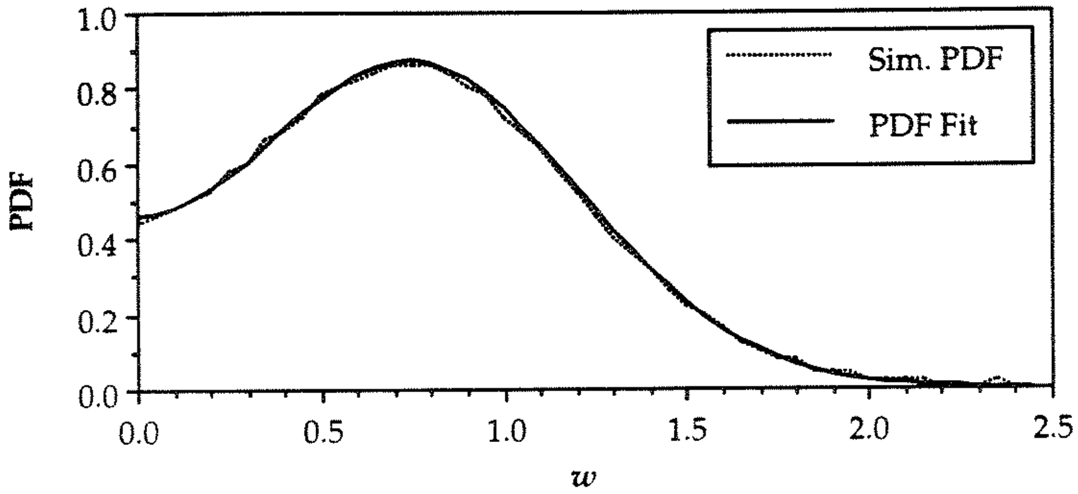

Fig. 6.21 Simulated & Fitted PDF of Normalized Intercept Widths, w

$V_P(1,2)$ is stationary and isotropic, therefore $\rho_{\psi\psi}(x_1,x_2)$ reduces to $\rho_{\psi\psi}(\chi)$, where $\chi = | x_2 - x_1 |$. For uncorrelated crystal orientations, the case considered here, the autocorrelation function $\rho_{\psi\psi}(\chi)$ can be derived from the PDF of intercept widths, $f_W(w)$. This derivation is described below.

Assuming independence between angle orientations when points lie in different intervals of the intercept process (see Fig. 6.22), one can define the following relationship

$$\begin{aligned} \mathrm{E}[\psi(x_1)\psi(x_2)] &= \mathrm{E}[\psi^2]p + \mathrm{E}^2[\psi](1-p) \\ &= \mathrm{E}^2[\psi] + p\{\mathrm{E}[\psi^2] - \mathrm{E}^2[\psi]\} \\ &= \mu_\psi^2 + p\sigma_\psi^2 \end{aligned} \tag{6.42}$$

where p is the probability that points x_1 and x_2 are in the same interval (i.e. same crystal), $(1 - p)$ is the probability that they are in different intervals, and

μ_ψ and σ_ψ are the mean and standard deviation of the distribution of angles ψ. The latter are directly obtained from the ODF.

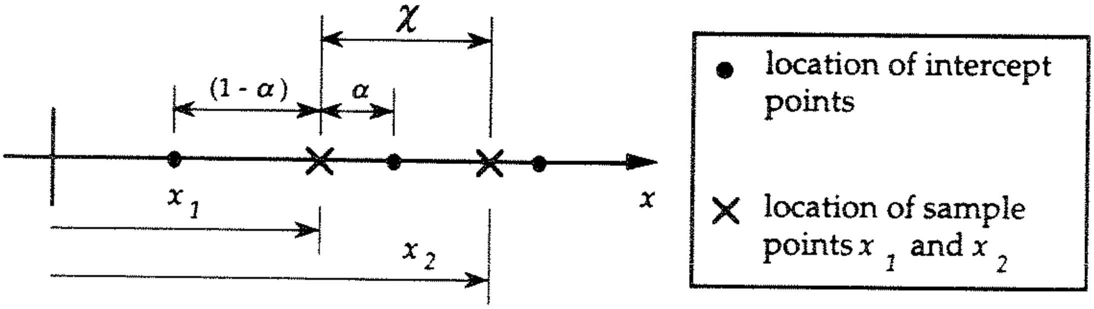

Fig. 6.22 Schematic Diagram of Two Points in Relation to the Crystal Intervals

The autocorrelation coefficient function, $\rho_{\psi\psi}(\chi)$, can now be defined in terms of $E[\psi(x_1)\psi(x_2)]$, and simplified using Eq. 6.42 to yield the following expression:

$$\rho_{\psi\psi} = \frac{E[\psi(x_1)\psi(x_2)] - \mu_\psi^2}{\sigma_\psi^2} = p \tag{6.43}$$

An expression defining p can be derived for fixed α based on the schematic diagram in Fig. 6.22

$$\begin{aligned} p &= \mathrm{P}(\alpha w > \tau) \\ &= \mathrm{P}\left(w > \frac{\tau}{\alpha}\right) \\ &= \int_{\tau/\alpha}^{\infty} f_W(w)dw = 1 - F_W\left(\frac{\chi}{\alpha}\right) \end{aligned} \tag{6.44}$$

where $\chi = | x_2 - x_1 |$ and α is the parameter defined in Fig. 6.22. Since the point could be anywhere within the interval with equal likelihood, a uniformly distributed α between 0 and 1 is assumed. Eq. 6.44 is then integrated with respect to α, resulting in the following expression for p

$$p = 1 - \int_0^1 F_W\left(\frac{\tau}{\alpha}\right) d\alpha \tag{6.45}$$

Integrating Eq. 6.45 by parts and substituting in Eq. 6.43, we obtain

$$p = \rho_{\psi\psi}(\chi) = \int_{\chi}^{\infty} \left(1 - \frac{\chi}{u}\right) f_W(u)\,du \tag{6.46}$$

Thus we have an analytic expression for the autocorrelation coefficient function, $\rho_{\psi\psi}(\chi)$. This expression can be evaluated by substituting the analytical PDF into Eq. 6.46 (or the analytical CDF into Eq. 6.45). We are in no way restricted to 2-D problems here. The PDF in Eq. 6.46 can be derived from any model (2-D or 3-D), either theoretical or empirical, the latter based on observations obtained through image analysis (see §5.1).

Since point-to-point characteristics of ψ are determined, there is no spatial averaging involved in the derivations and therefore μ_ψ and σ_ψ simply correspond to the mean and standard deviation of ψ defined by the ODF.

Thus, μ_ψ and σ_ψ are obtained from the ODF and $\rho_{\psi\psi}(x)$ is evaluated using the PDF of w and Eq. 6.46. For planar PVDs, the analytical PDF defined in Eq. 6.41 can be used. Thus, knowing λ and the ODF, the ψ random field is identified in a second-moment context. This also defines the full elasticity matrix random field in terms of C_{ij} and employing the appropriate transformations, e.g. through Eq. 6.38.

$E[\psi(x)]$ is easy to find once the $\psi(x)$ random field is modeled, e.g. using Eq. 6.15. In $E(x)$ modeling for a beam structure (§6.3), spatial averaging is performed in the y direction, thus changing the standard deviation (reduced) and correlation structure (increased correlation).

6.6 FINITE ELEMENT IMPLEMENTATION

6.6.1 Beam Elements for EI(x) Random Field Model

The structural model needs to employ appropriate beam elements to model the irregular variation in $E_{eff}(x)$ shown in Fig. 6.8 or of $I(x)$.

Nonuniform beam elements are used here which allow a linear variation of *EI(x)* within each element [6.5]. The beam element degrees of freedom 1,2,3, and 4 are the vertical displacements and end rotations for the left and right nodes respectively. To solve for the elements of the stiffness matrix, the following three basic integrals need to be evaluated:

$$J_i = \int_0^L \frac{x^i}{E(x)I(x)}\,dx\,, \quad i = 0,1,2 \tag{6.47}$$

Eq. 6.45, for i = 0, 1, 2, is solved analytically for linear variations in *EI(x)*. The element stiffness matrix is given by:

$$\mathbf{K} = \frac{1}{D}\begin{bmatrix} J_0 & J_1 & -J_0 & J_0L - J_1 \\ J_1 & J_2 & -J_1 & J_1L - J_2 \\ -J_0 & -J_1 & J_0 & -J_0L + J_1 \\ J_0L - J_1 & J_1L - J_2 & -J_0L + J_1 & J_0L^2 - 2J_1L + J_2 \end{bmatrix} \tag{6.48}$$

where L is the length of the beam element and D is defined by:

$$D = J_0J_2 - J_1^2 \tag{6.49}$$

The above formulation enables a continuous modeling of any irregular variation in *EI(x)* and, with sufficiently fine discretizations, produces close representations of the multicrystalline beam behavior. Fig. 6.23 compares results for the deflection of a cantilever beam obtained through the discrete model presented in Chapter 5 (Fig. 5.9) and the beam model developed above using 200 elements. This example represents a deterministic case with known geometry.

A probabilistic problem is presented in §7.2.2 and solved using the above formulation and the random field model. The results compare well with the simulated multicrystalline model.

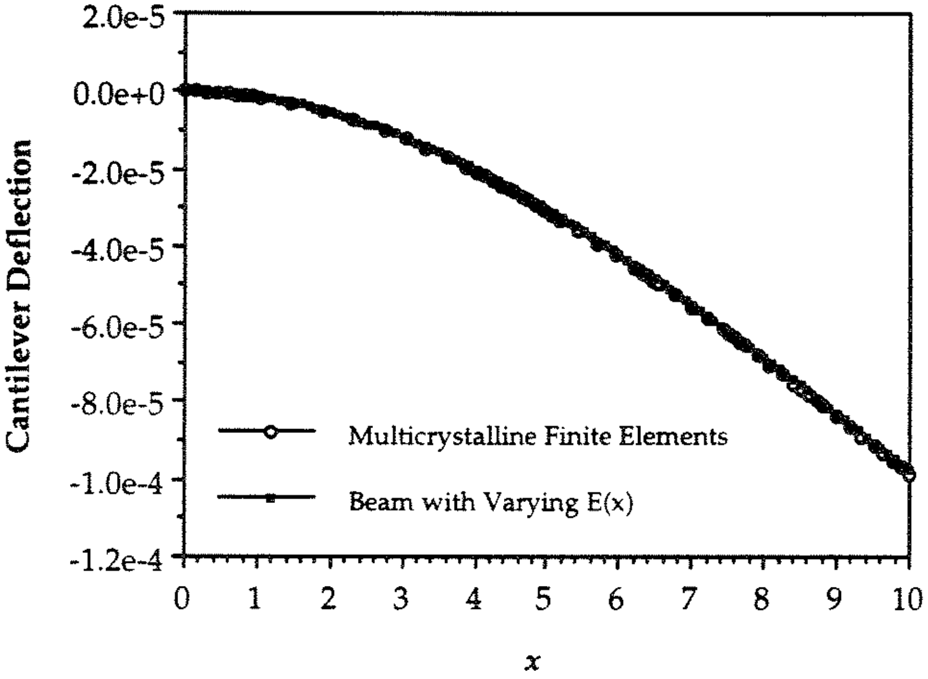

Fig. 6.23 Deflected Shape for Cantilever Beam: Multicrystalline Finite Elements & Beam Model

6.6.2 2-D & 3-D Elements for C(x) Random Field Model

Since the elasticity stiffness matrix C(x) is fully modeled, any finite element approximation is possible in the linear elastic range. Depending on the assumptions regarding the structural behavior, membrane, plate, shell, or solid (brick) elements can be used with their constitutive properties based on the C(x) model. The random field discretization using the EOLE method would proceed in a similar fashion to 1-D models, except the ordering of the elements must be made such that the eigenvalue problem has as narrow a band width as possible.

An example is used to illustrate the above approach. MEMS polycrystalline beams are often assumed to have a fixed end boundary. In many applications, however, the fabrication results in a finite flexibility at the "fixed" ends. Fig. 6.24 (a) shows such a case for a beam of depth *d*, where the end-zone is fully restrained against movements only beyond a 3*d* by 3*d* region (variable *d* is used instead of *w* to avoid confusion with chord lengths *w*). This problem is now analyzed to assess the mean and standard deviation of the flexibility in the end-zone.

The finite element discretization and loading are shown in Fig. 6.24 (b), (c), and (d). The material is assumed to have {100} texture, with uniform in-plane distribution for the orientation angle $\psi(x)$. Using the random field discretization methodology of §6.2.3 for $\psi(x)$, taking the mean orientation angle to equal zero, Eq. 6.9 and 6.10 are rewritten as

$$\Sigma_{\psi\psi}\phi_i = \theta_i\,\phi_i \tag{6.50}$$

and

$$\hat{\psi}(x) = \sum_{i=1}^{r} \frac{\zeta_i}{\sqrt{\theta_i}}\,\phi_i^{T}\Sigma_{\psi(x)\psi} \tag{6.51}$$

The covariance matrix $\Sigma_{\psi\psi}$ of orientations for the 36 elements shown in Fig. 6.24 (b) is established based on the autocorrelation function of the form defined in Eq. 6.46. This equation is solved numerically, with parameters $d = 1$ µm and $\lambda = 3\ /\ (\mu m)^2$ to yield the autocorrelation function, $\rho_{\psi\psi}(\chi)$, plotted in Fig. 6.25.

Solution of the eigenvalue problem in Eq. 6.50 yields the eigenvalues, θ_i, and eigenvectors, ϕ_i. Sufficient accuracy is obtained in characterizing the random field using $r = 12$, i.e. only 12 independent random variables are needed to characterize the uncertainty in the problem. All 36 eigenvalues are listed in Table 6.2.

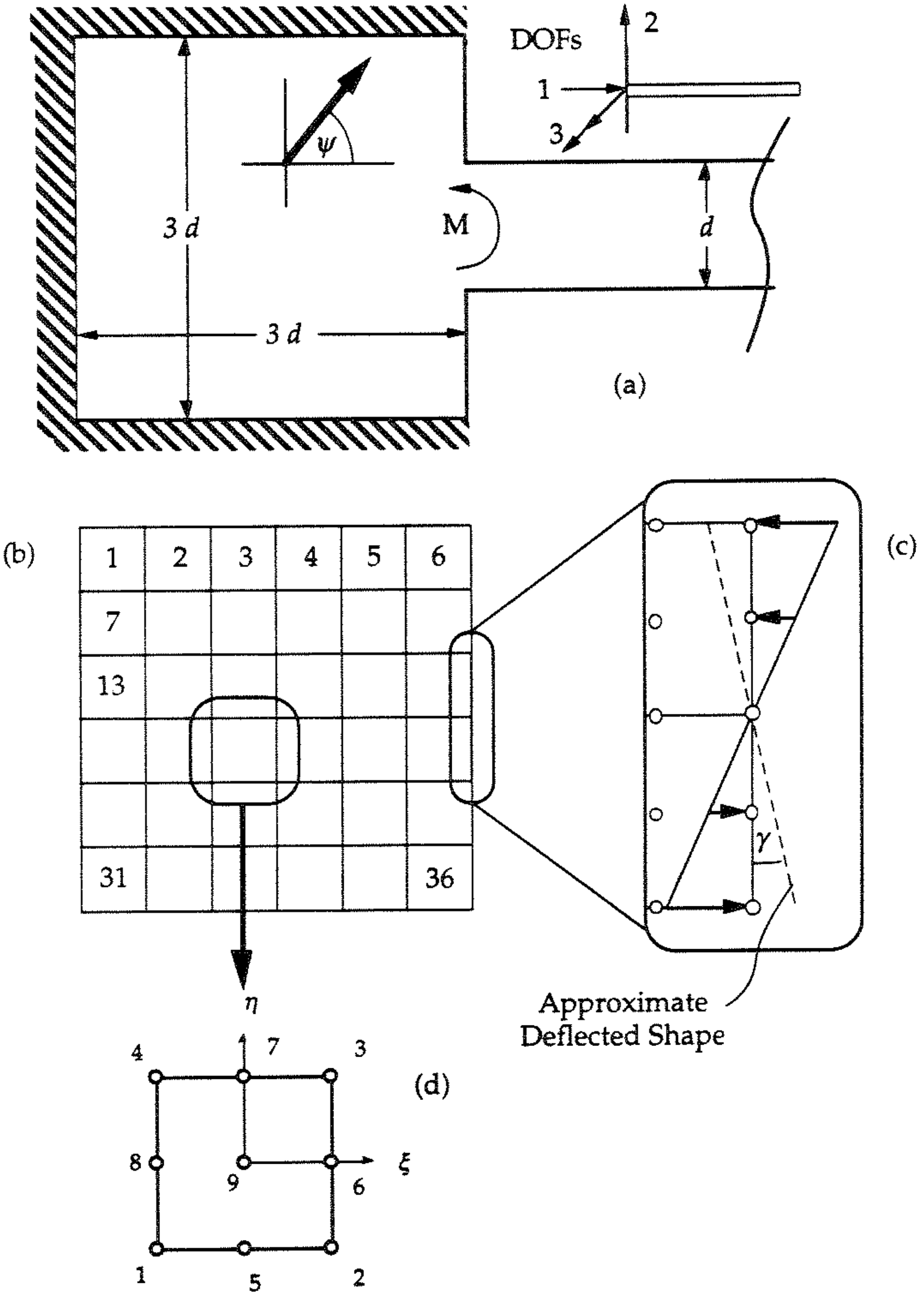

Fig 6.24 End-Zone Model—(a) Dimensions and Displacement Boundary Conditions; (b) Finite Element Mesh; (c) Force Boundary Conditions; (d) 9-node Isoparametric Element

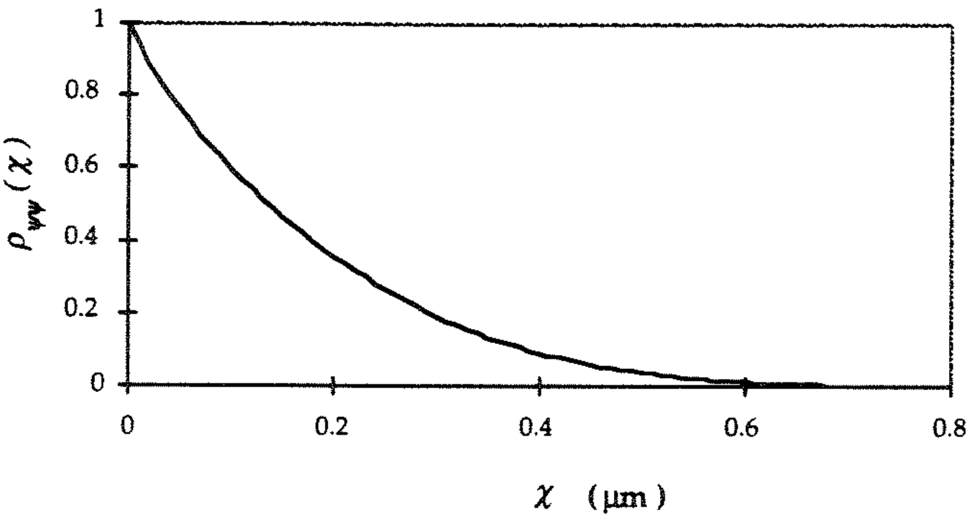

Fig. 6.25 Autocorrelation Function of Orientation Angles $\rho_{\psi\psi}(\chi)$

Table 6.2 Eigenvalues for Covariance Matrix

1.155339	1.129395	1.129395	1.104698
1.091905	1.091905	1.069009	1.069009
1.050295	1.050295	1.035922	1.029397
1.029397	1.012805	1.012805	0.999199
0.999199	0.993708	0.993708	0.986861
0.986861	0.969010	0.969010	0.966112
0.966112	0.965681	0.943215	0.943215
0.935483	0.935483	0.914585	0.914585
0.907887	0.888790	0.888790	0.870939

Given the values of ζ_i, discrete orientations are assigned to each element based on Eq. 6.51. These orientations are sufficient to define the element stiffness matrices (Eq. 4.16) and the finite element solution is found for the approximate rotated beam angle, γ. For $d = 1$ μm, $t = 0.25$ μm, $\lambda = 3$ / μm^2, and M = 10^{-12} Nm, the rotational stiffness is computed to be 7310 x 10^{-12} Nm, with a C.O.V. of 1.2 %.

The beam endzone problem is re-solved using tensile and shear loading in order to evaluate the stiffness characteristics in DOFs 1 and 2, respectively (see Fig. 6.24). The mean and C.O.V.s are found to be 211 x 10^{-3} Nm^{-1} and 5.9 % for DOF 1, and 103 x 10^{-3} Nm^{-1} and 4.2 % for DOF 2. If these flexibilities are applied to the beam shown in Fig. 5.9, the average end deflection would increase by approximately 11%. The relative inflexibility in all DOFs, and the small C.O.V.s therefore indicate that the modelling of fixed-end beams as fully fixed is a good approximation.

6.7 SUMMARY

The simulation model of Chapter 5 is computationally intensive and cannot be readily applied using conventional finite element models. A random field model was proposed here which captures the essential features of the behavior of multicrystalline beams. This model was first developed for the effective stiffness of flexural multicrystalline beams by establishing the mean, standard deviation, and autocorrelation function. This model then allows a regular finite element mesh to be used to model the multicrystalline problems. Comparisons with the multicrystalline model show close agreement in global response such as end deflection.

The random field approach is generalized to 2- and 3-D problems by characterizing the random field of orientations in space. The stiffness matrix at each point is fully determined by the crystalline orientation. Empirically based chord length distributions are employed to derive closed form expressions for the autocorrelation function. An example problem was used to illustrate the use of this approach in modelling the end-zone flexibility of "fixed" beam connections.

CHAPTER 6 REFERENCES

[6.1] Bunge, H. J., *Texture Analysis in Materials Science*, Butterworths Publ., London, 1982.

[6.2] Chatfield, C., *The Analysis of Time Series—An Introduction*, [4th Ed.], Chapman & Hall, London, 1989.

[6.3] Der Kiureghian, A. and Ke, B. -J., "The Stochastic Finite Element Method in Structural Reliability," *Probabilistic Engineering Mechanics*, Vol. 3, p. 83, 1988.

[6.4] Eisenberger, M., "Exact Static and Dynamic Stiffness Matrices for General Variable Cross Section Members," *AIAA Journal*, Vol. 28, No. 6, pp. 1105–1109, 1990.

[6.5] Friedman, Z. and Kosmatka, J.B., "Exact Stiffness Matrix of a Nonuniform Beam—I. Extension, Torsion, and Bending of a Bernoulli-Euler Beam," *Computers and Structures*, Vol. 42, No. 5, pp. 671–682, 1992.

[6.6] Gilbert, E. N., "Random Subdivision of Space into Crystals," *Annals of Mathematical Statistics*, Vol. 33, pp. 958–972, 1962.

[6.7] Ivanov, A. V. and N. N. Leonenko, *Statistical Analysis of Random Fields*, [Translated from the Russian by A. I. Kochubinsky] Kluwer Academic Publishers, Dordrecht, The Netherlands, 1989.

[6.8] Lekhnitskii, S. G., *Theory of Elasticity of an Anisotropic Elastic Body*, [Edited by J. J. Brandstatter, Translated by P. Fern] Holden-Day, San Francisco, 1963.

[6.9] Li, C.-C. and Der Kiureghian, A., "Optimal Discretization of Random Fields," *Journal of Engineering Mechanics, ASCE*, Vol. 119, No. 6, pp. 1136–1154, 1993.

[6.10] Muche, L. and D. Stoyan, "Contact and Chord Length Distributions of the Poisson Voronoï Tessellation," *Paper presented at the Upsala Conference*, 1990.

[6.11] Näther, W., *Effective Observation of Random Fields*, Aufl. Leipzig, Teubner, 1985.

[6.12] Popov, E. P., *Introduction to Mechanics of Solids*, Prentice-Hall, Englewood Cliffs, N.J., Art. 6–10, 1968.

[6.13] Ramm, A. G, *Random Fields Estimation Theory*, Pitman Monographs and Surverys in Pure and Applied Mathematics Vol. 48, Longman Scientific and Technical, England, 1990.

[6.14] Romano, F. and Zingone, G., "Deflections of Beams with Varying Rectangular Cross Section," *Journal of Engineering Mechanics*, Vol. 118, No. 10, pp. 2128–2134, 1992.

[6.15] Tang, W. C., M. G. Lim, and R. T. Howe, "Electrostatically Balanced Comb Drive for Controlled Levitation," *IEEE Solid-State Sensor and Actuator Workshop*, June 1990, pp. 23-27.

[6.16] Ting, T. C. T., "Invariants of Anisotropic Elastic Constants," *Quarterly Jounal of Mechanics and Appliced Mathematics*, Vol. 40, Pt. 3, pp. 431–448, 1987.

[6.17] Vanmarcke, E., *Random Fields: Analysis and Synthesis*, The MIT Press, Cambridge, Massachusetts, 1983.

[6.18] Wang, Y. T., "Random Field Stiffness Properties and Reliability of Laminated Wood Beams," *Structural Safety*, Vol. 11, pp. 191–202, 1992.

[6.19] Zienkiewicz, O. C. and Taylor, R. L., *The Finite Element Method, Vol. 1*, McGraw-Hill, London, U.K., 1989.

[6.20] Lin, L.-W., Personal communication, April 1993.

Chapter 7

MEMS STRUCTURAL APPLICATIONS

7.1 INTRODUCTION

Estimation of the mechanical response of MEMS is a necessary component of any design process. This estimation is acheived through the modelling of the material properties and subsequent structural analysis of MEMS devices. Experimental, or *in-situ*, procedures have also been developed which predict quantities characterizing the mechanical properties of thin films, e.g. residual stresses [7.4 , 7.13], or Young's modulus [7.3, 7.13, 7.17]. These quantities are often impossible to measure through direct means and their indirect experimental estimation relies on mechanical models of the measuring devices. Material modelling is the basis for all mechanical models and this chapter is devoted to the application of these models to the analysis of MEMS' structural responses.

The material processing of MEMS results in a wide range of material properties depending on the specific process conditions (§2.4). A uniform material model applicable to all these cases, even for the polysilicon sub-class of MEMS, is therefore impossible to define. Thus, separate material models are required. Here, the importance of *appropriate* choices of material models is illustrated through the application of models developed in earlier chapters (homogenization, simulation, and random field models) to a number of example problems. These examples highlight common misleading interpretations of response observations and, through the analysis of the results, a guideline is proposed for choosing the appropriate material model for various classes of problems.

Design applications are presented at both the structural component and device levels. Contributing parameters to structural component performance uncertainty are examined. Ways of reducing this uncertaintainty to an acceptable level at the structural component level or for a complete device are then identified. The former can be achieved through varying structural dimensions and/or control of grain size and texture, while the latter can be achieved through variations in structural configurations or designs. These topics are explored using the folded-beam lateral micro resonator (FBLMR) as the example device.

Finally, experimental results for an example MEMS device—a "passive *in-situ* micro strain gauge" [7.6]—are compared with theoretical predictions.

7.2 CHOICE OF MATERIAL MODELS

7.2.1 Basic Concepts

Design of MEMS structures and devices often requires prior structural analyses to predict the mechanical response of the device. Structural analyses of appropriate sophistication are performed employing derived or measured material properties. Direct experimental methods are often used for the *in-situ* determination of elastic moduli, e.g. the "Young's modulus," for polysilicon [7.3, 7.13, 7.17]. This is achieved through measurement of an observable response, R (such as a displacement, rotation, or the natural frequency of vibration), of an elastic structure or device, followed by a mechanical transformation to obtain the elastic modulus of interest.

Both structural analyses for device designs and *in-situ* measurement techniques are based on mechanical transformations of the form:

$$R = f(\mathbf{E}) \tag{7.1}$$

where E represents a set of one or more elastic moduli. These relations are established either using an appropriate closed-form theoretical approach, such as the theory of elasticity and structural mechanics theories (Euler-Bernoulli beam theory, non-linear beam theories, plate theories, etc.), or through algorithmic approaches, e.g. using finite element analysis [7.18]. The values for E are then deduced using one or more observed responses and the inverse of the mechanical transformation.

Advanced approaches to establishing mechanical transformations (Eq. 7.1) have been employed in MEMS applications, e.g. through the use of higher-order structural theories [7.18], or through more precise modelling of the boundary conditions [7.19]. Implicit in all such approaches as applied to polycrystalline materials, however, has been the adoption of a simplified material model—namely that of a homogeneous isotropic medium. This assumption, however, is not generally valid, only applying under certain limiting conditions. When these assumptions are not valid, the increased accuracy obtained by the use of more advanced structural thories is, essentially, increasing the precision of an innaccurate approach.

The elastic properties of isotropic, homogeneous materials can be characterized using only two independent parameters, e.g. Young's modulus, E and Poisson's ratio, ν. A unique value of E, for example, is meaningful only when describing isotropic, homogeneous materials. For MEMS structural components composed of fine-grained polysilicon, a homogeneity assumption is valid only if a representative volume element (RVE) exists (§4.2.1). In such cases, sufficient numbers of crystal grains exist for statistical averaging to be valid in determining homogenized material properties. Furthermore, for untextured fine-grained samples, the material *can* be treated as being isotropic since the single-crystal anisotropies are uniformly averaged out in all directions.

Textured polysilicon, however, is anisotropic. For some textures, e.g. {100} or {110} perpendicular to the thin-film surface (§3.2 and §4.3), a plane of symmetry exists and the material is transversely-isotropic [7.18]. For those cases, a "Young's modulus" for the material usually refers to the planar Young's modulus. Since many MEMS structures and devices are planar, their behavior *can* be described using isotropic material models. For out-of-plane behavior of textured samples, however, isotropy assumptions are incorrect.

For all other textured homogeneous cases together with non-homogeneous cases the notion of a unique value for the Young's modulus of the polycrystalline material samples is both imprecise and incomplete.

Figure 7.1 illustrates a flow chart defining different material-structure classifications as Class I, II, III, and IV for given structural dimensions. Each material-structure classification requires a different material modelling approach. Failure to apply the appropriate material model invalidates the mechanical transformation of Eq. 7.1 and can produce at best misleading, and sometimes meaningless results regardless of the level of sophistication of the structural analysis method. For example, the irreproduceability of certain experimental results in different microfabrication laboratories or the widely differring reported values for elastic moduli, say, E [7.15] can be partly attributed to such innapropriate uses of material models in the various methods of analysis. The example problem which now follows illustrates some of these inconsistencies.

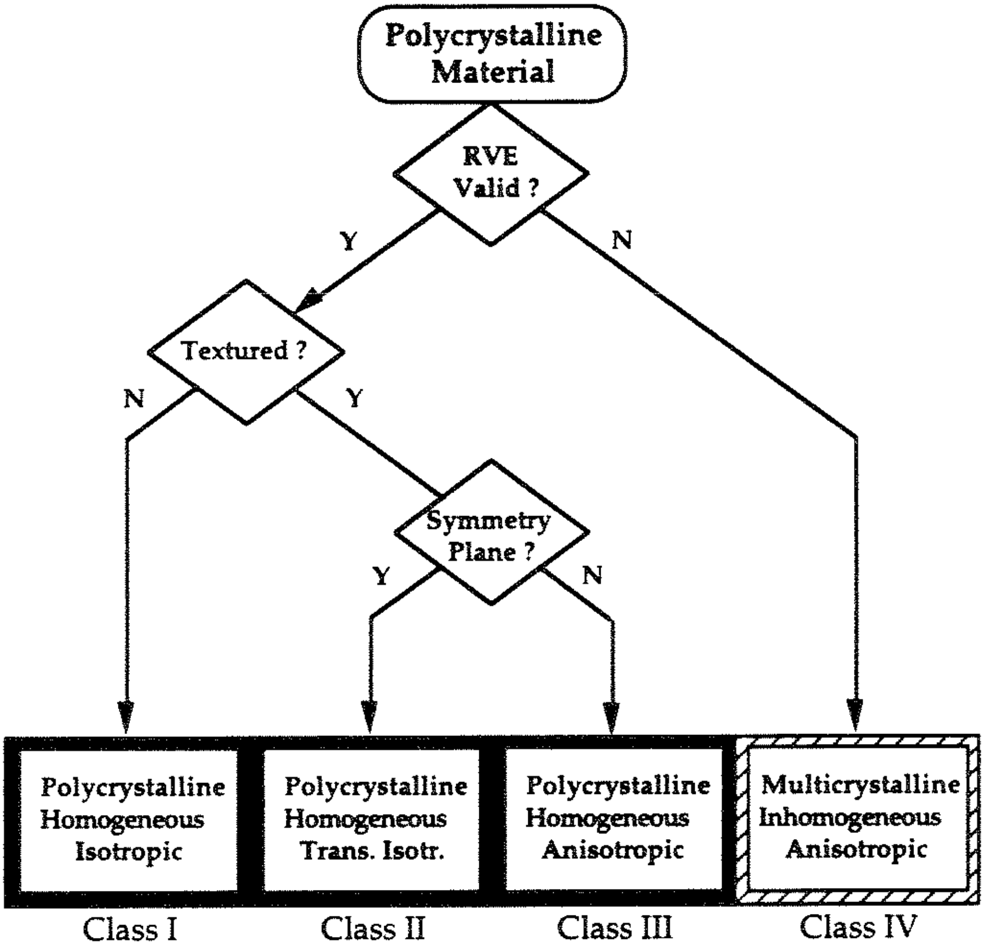

Fig. 7.1 Identification of Material-Structure Classifications I through IV

7.2.2 Example Problem

Three of the four material-structure classifications of Fig. 7.1 are examined in the context of an example problem. For these problems, all crystalline imperfections such as dislocations, effects of dopants, etc. (see §3.2.1) are ignored. Thus, the results only illustrate the response variations related to differring material microstructures. The inclusion of the effects of imperfections in the analysis would introduce *additional* variations and therefore should not invalidate any of the following results and inferences.

First, a fine-grained sample with perfect disorder (i.e. untextured) is chosen. To a good approximation, this is a homogeneous and isotropic medium (Class I) and an exact solution for the value of E exists (see §4.2.3, where using Eqs. 4.10–13, an iterative solution is found). Using the following values for the elastic constants for silicon (crystaline state) [7.12]

$$\begin{aligned} C_{11} &= 165.6 \text{ GPa} \\ C_{12} &= 63.8 \text{ GPa} \\ C_{44} &= 79.5 \text{ GPa} \end{aligned} \tag{7.2}$$

the n-th order bounds on E for an untextured sample are found to converge to 162.8 GPa as $n \to \infty$ (see §4.23 and Fig. 4.2).

Polycrystalline, homogeneous, but anisotropic samples (Class III), e.g. fine-grained material with {110} texture, would exhibit anisotropy. For the case of {110} texture, there would be in-plane orthotropy and analysis of problems would need to use orthotropic beam behavior models.

Next, the material is assumed to be fine-grained, but with {100} texture perpendicular to the thin-film plane (Class II). This configuration results in transversely-isotropic properties. The material is still homogeneous and the problem can be treated deterministically. However, with incomplete statistical information regarding the grain shapes, only bounds on the elastic properties can be established. With only volume fraction information, i.e. the orientation distribution function (ODF), the bounds on E are the 1st-order Voigt and Reuss bounds (see §4.2.3). The derived Voigt, and Reuss bounds for

{100} texture, $E^V_{\{100\}}$, $E^R_{\{100\}}$, and the Hill (arithmetic) average, $E^H_{\{100\}}$, are given below (VRH values):

$$\begin{aligned} E^V_{\{100\}} &= 166.3 \text{ GPa} \\ E^R_{\{100\}} &= 161.1 \text{ GPa} \\ E^H_{\{100\}} &= 163.7 \text{ GPa} \end{aligned} \tag{7.3}$$

A simple end-loaded cantilever beam problem shown in Fig. 7.1(a) is chosen to illustrate the outcomes of the analysis using the different material assumptions.

Employing Euler-Bernoulli beam theory for a homogeneous and isotropic material, the inverse of Eq. 7.1 is

$$E = \frac{PL^3}{3I}\left(\frac{1}{\Delta}\right) \tag{7.4}$$

where $R = \Delta$ is the tip displacement and I is the moment of inertia of the cross section. Taking $L = 10$ μm, beam thickness $t = 0.25$ μm, $d = 1$ μm, and $P = 1$ μN, the beam deflection, $\Delta = 9.828 \times 10^{-2}$ μm $= \Delta_{isotropic}$ for the untextured case. For {100} texture, the VRH values for Δ are found to be:

$$\begin{aligned} \Delta^V_{\{100\}} &= 0.979\Delta_{isotropic} \\ \Delta^R_{\{100\}} &= 1.011\Delta_{isotropic} \\ \Delta^H_{\{100\}} &= 0.995\Delta_{isotropic} \end{aligned} \tag{7.5}$$

The end-loaded cantilevered beam, shown in Fig. 7.2(b), is made up of a relatively small number of crystals arranged randomly, corresponding to a Voronoï tesselation of Poisson points in two-dimensional space with $\lambda = 3$ μm^{-2} (see §5.4). With $\alpha = 1.562$, i.e. representing silicon, {100} texture, $d = 1$ μm, $P = 1$ μN, and a beam thickness of 0.25 μm, the average size of the crystal grains relative to the dimensions of the beam is such that a RVE does *not* exist (Class IV). For this problem basic assumptions such as plane sections remaining plane are invalid and the Euler-Bernoulli beam theory does not apply. Furthermore the uncertainty associated with the shapes, sizes, and orientations of the individual grains that make up the beam means that the problem cannot be solved by deterministic means. Hence, a probabilistic finite element solution is sought. The results are obtained in the form of mean and C.O.V. using the simulation model (Chapter 5) and in the form of a probability density function (PDF) using the random field model (Chapter 6).

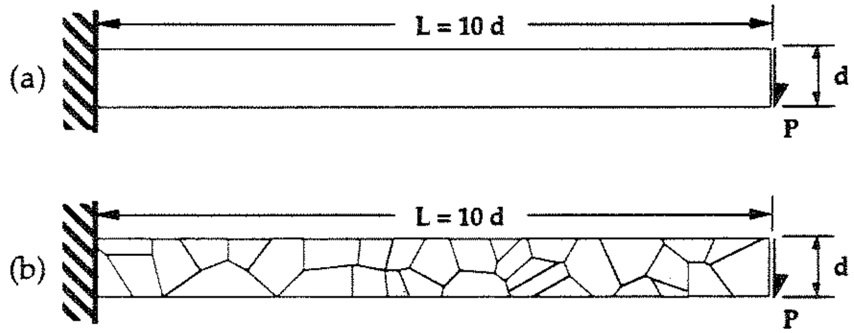

Fig. 7.2 End-Loaded Cantilevers: (a) Homogenizable (Class I, II, or III); (b) Inhomogeneous—Multicrystalline Structure (Class IV)

Using the simulation model, the mean of the response, Δ, is found to be $0.990\,\Delta_{isotropic}$, with a coefficient of variation (C.O.V.) of approximately 3%. This involved simulation of 100 beams and their repeated finite element modelling and analysis. The finite element discretization is as formulated in Chapter 5.

The random field solution for the problem is based on the correlation model developed in §6.3.3, discretized using the "EOLE" method [7.5] and using variable stiffness beam elements [7.14] in conjunction with the first-order reliability method (FORM) and associated sensitivity results [7.9] to evaluate the PDF of structural response. For the cantilever problem shown in Fig. 7.2(b), 20 random variables are used in discretizing the random field, together with 100 beam elements, consistent with the correlation length requirements of the random field. The PDF of the cantilever tip displacement, Δ, is derived and the coefficient of variation (C.O.V.) of response is found to equal 3.14%. The results for the above are summarized in Table 7.1 and are shown graphically in Fig. 7.3.

Table 7.1 Cantilever Tip Displacement Results

Class I	Class II	Class IV
$\Delta_{isotropic} = 9.828 \times 10^{-2} \mu\text{m}$	$\Delta^{V}_{\{100\}} = 0.979 \Delta_{isotropic}$	$\mu_\Delta - \sigma_\Delta = 0.959\, \Delta_{isotropic}$
	$\Delta^{H}_{\{100\}} = 0.995 \Delta_{isotropic}$	$\mu_\Delta = 0.990\, \Delta_{isotropic}$
	$\Delta^{R}_{\{100\}} = 1.011 \Delta_{isotropic}$	$\mu_\Delta + \sigma_\Delta = 1.021\, \Delta_{isotropic}$

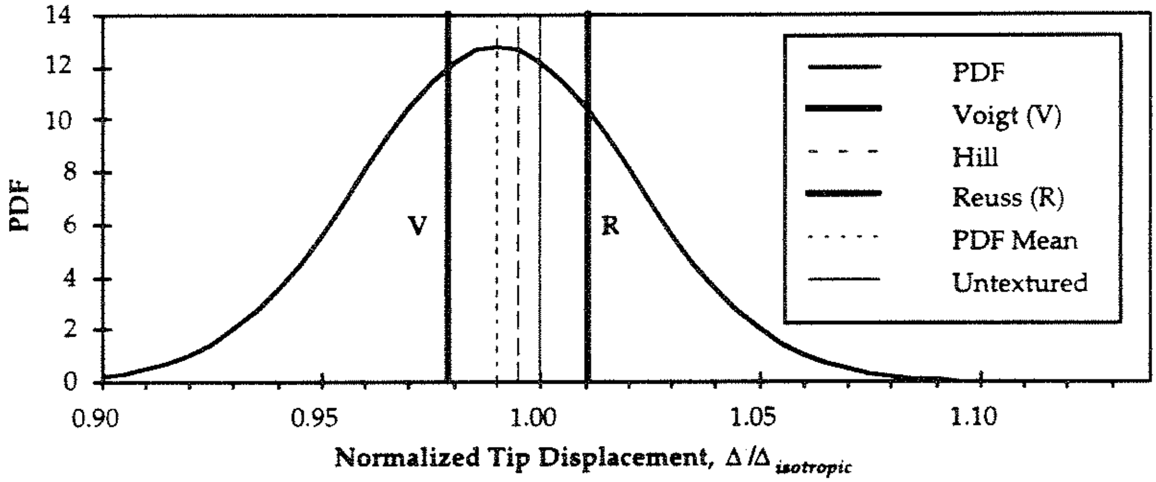

Fig. 7.3 Tip Displacement Results for Class I, II, and IV Problems

Results for Class IV quantify the uncertainty in the structural response. This uncertainty arises from the random grain sizes and shapes, and the variation in individual grain orientations. It is clear from Fig. 7.3 that the Voigt and Reuss bounds are apparently "violated" by a significant proportion of the outcomes. Note, however, that the assumption for the validity of the Voigt Reuss bounds do not apply for Class IV materials (see §4.2.1). The uncertainty in structural response will diminish as crystal grain sizes become smaller relative to the beam dimensions.

For a sufficiently large number of grains such that a RVE exists, the C.O.V. of response will be negligible, such that a deterministic approximation would be appropriate. This would reclassify the problem as Class II. Hence, for the crystal geometry defined by the Voronoï diagram, the "exact" homogenized result—i.e. convergent bounds when full statistical information is available—coincides with the mean response. This result, as expected, is within the Voigt and Reuss bounds. The Hill estimate (the arithmetic mean of the Voigt and Reuss bounds), however, does not coincide with this value. Nevertheless, the Hill estimate, although ad hoc, is the best approximation based on first-order textural information such as the ODF.

In the design of structures, incorrect material models would result in incorrect response predictions. Furthermore, deriving material properties such as Young's modulus from experimental observations would also result in similar errors in the predicted values. The incorporation of appropriate material models in the design/analysis/testing process is therefore necessary for more reliable results. For example, consider a Class IV material with {100} texture in the cantilever beam problem outlined above. An incorrect homogeneous isotropic material assumption would result in an error of 1% in the estimate for the average end deflection, while incorporation of {100} textural information and use of the Hill estimate (i.e. assuming material homogeneity) would reduce this error down to 0.5%. In both cases, the inherent uncertainty in the results, namely a C.O.V. of 3.14%, has not been accounted for. The above discrepancies, while small in the context of mainstream structural engineering, can be significant in the context of MEMS, where a high degree of precision in predicting structural response is often required. Furthermore, materials exhibiting higher degrees of anisotropy than polysilicon, will further accentuate the above discrepancies.

For many applications, oversights on material modelling accuracy have gone unnoticed due to their relative unimportance. Residual stress effects, for example, have often dominated structural behavior. Certain self-calibrating devices have also been designed which overcome the unpredictable structural response [7.2]. Nevertheless, with the increasing push to the frontiers of miniaturization, the knowledge and use of material modelling techniques that take into account the deviations from isotropy and homogeneity becomes increasingly important. Hence, methods that can capture these material behaviors will have increasing demand.

7.3 STRUCTURAL COMPONENTS—BEAMS IN FLEXURE

There will always be a finite coefficient of variation associated with a property of interest, i.e. one can never assign an absolute deterministic value to, say, the Young's modulus of a material. Practically speaking, however, when the C.O.V. is lower than a certain level, the problem effectively becomes deterministic.

A quantifiable method of determining whether the problem is effectively deterministic is to define finite bounds for the response of interest within which a "sufficient" proportion of random outcomes can be expected to fall, e.g. 95%. In Chapter 4, the Voigt-Reuss bounds on E for polysilicon were shown to be relatively narrow due to the relatively small anisotropy of silicon

($\alpha = 1.56$). These bounds are therefore used as an example for determining whether the lateral stiffness of a multicrystalline beam can be considered as being deterministic.

The beam analyzed in §7.2.1 is re-analyzed with different displacement and force boundary conditions such that the lateral stiffness of a beam of length L and width w can be found. The desired boundary conditions are as follows:

$$\left.\begin{array}{r} u=0 \\ u'=0 \end{array}\right\} \text{at } x=0 \qquad \left.\begin{array}{r} u=1 \\ u'=0 \end{array}\right\} \text{at } x=L \tag{7.6}$$

where u and u' denote the transverse displacement and slope of the beam, respectively. In this example, results are generated for the vertical reaction at $u = L$, i.e. the equivalent lateral stiffness of the beam given the displacement boundary conditions in Eq. 7.6.

Fig. 7.5 illustrates the above concepts. The unshaded area represents the probability that the Voigt and Reuss bounds are not "violated". This is mathematically defined as

$$P(k^R \le k < k^V) = F_K(k^V) - F_K(k^R) \tag{7.7}$$

where $F_K(k)$ is the cumulative distribution function. For a normally distributed k[†], i.e. N(μ_k, σ_k), Eq. 7.7 can be rewritten as

$$P(k^R \le k < k^V) = \Phi\left(\frac{k^V - \mu_k}{\sigma_k}\right) - \Phi\left(\frac{k^R - \mu_k}{\sigma_k}\right) \tag{7.8}$$

where $\Phi(.)$ is the standard normal probability.

[†] Values for k are bounded by the 0-th order bounds, $k^{(-0)}$ and $k^{(+0)}$, however, the normal distribution is an acceptable approximation since these bounds are relatively wide.

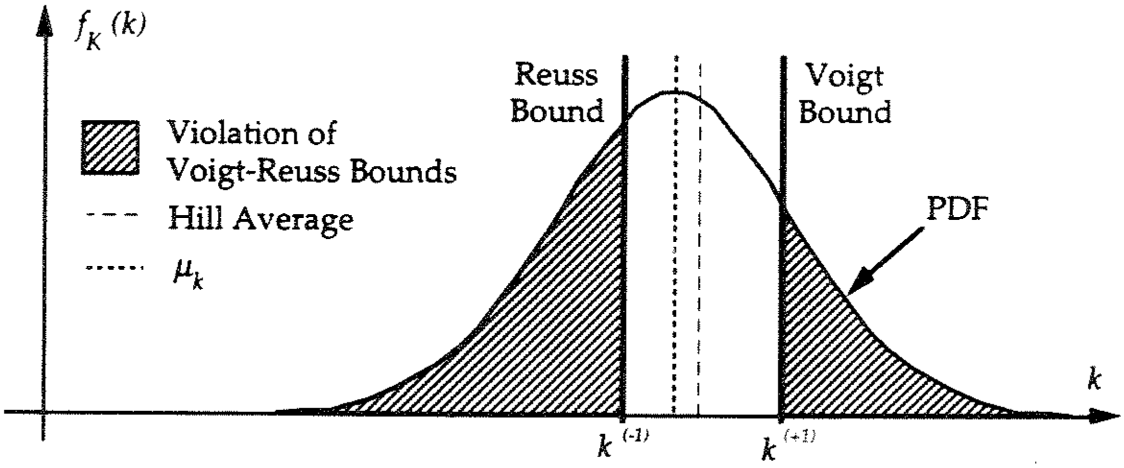

Fig. 7.5 Proportion of Outcomes Outside the Voigt-Reuss Bounds

The non-dimensional plot in Fig. 7.6 shows this equation graphically against the (C.O.V. of k)$/\,\Omega^{(1)}_{E\{100\}}$, where

$$\Omega^{(1)}_{E\{100\}} = \left(\frac{E^V_{\{100\}} - E^R_{\{100\}}}{E^H_{\{100\}}} \right) \approx 0.03177 \tag{7.9}$$

for polysilicon and where the varying values of δ represent normalized deviations of μ_k from k^H defined by

$$\delta = \frac{\left[\mu_k - \left(k^V + k^R\right)/2\right]}{\left(k^V - k^R\right)/2} = \begin{cases} +1 \text{ when } \mu_k = k^V \\ \;\;0 \text{ when } \mu_k = k^H \\ -1 \text{ when } \mu_k = k^R \end{cases} \tag{7.10}$$

An acceptable proportion is chosen from the y-axis and the corresponding upper bound on the C.O.V. of k is found.

The C.O.V. of k is determined using stochastic finite elements and the random field models of Chapter 6. Coefficients of variation for beams with different grain sizes and lengths are evaluated and shown in Table 7.2. The mean number of crystal grains within each beam (L,λ) is given by the product $\lambda L w$.

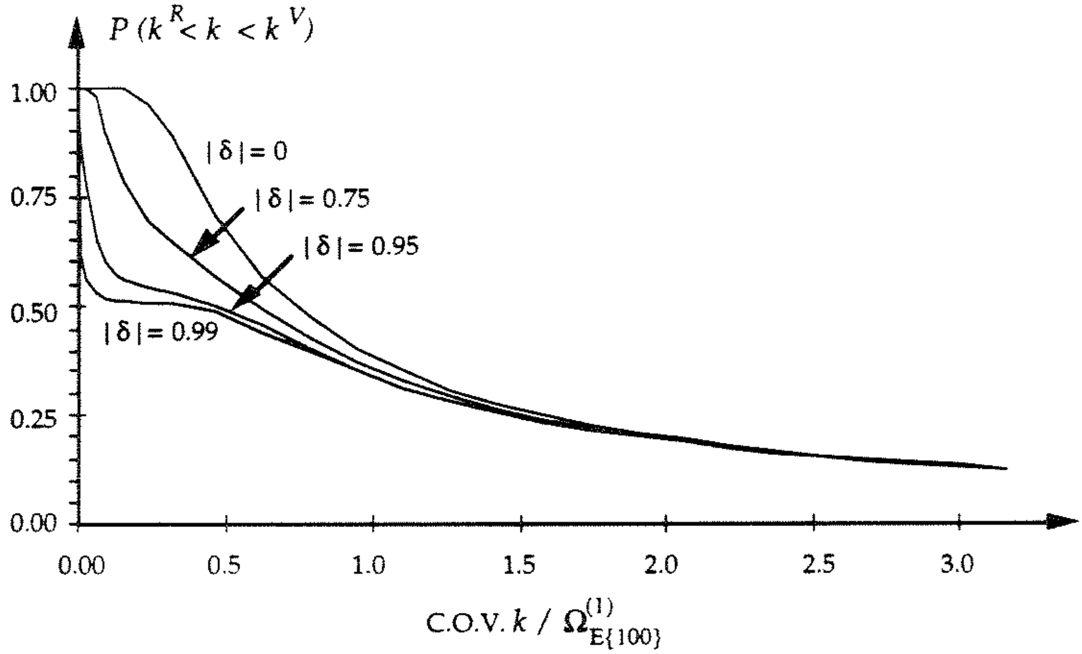

Fig. 7.6 Probability of not violating Voigt-Reuss Bounds vs. C.O.V. of Lateral Stiffness, *k* (valid for all λ, w, L)—{100} Texture

Table 7.2 Effect of Beam Length on the C.O.V. of Lateral Stiffness, *k* for "Multicrystalline" Silicon Beams of Width, $w = 1$ µm, and {100} Texture

	L = 10 µm	L = 20 µm	L = 40 µm
$\lambda = 1 /(\mu m)^2$	3.20%	4.42%	6.11%
$\lambda = 3 /(\mu m)^2$	2.29%	*	*
$\lambda = 9 /(\mu m)^2$	1.38%	*	*

* Not analyzed

From Fig. 7.6, the proportion of outcomes within the VR bounds are determined and are compared with a suitable pass rate for the application of interest, e.g. 95%. This procedure may serve as a preliminary test for evaluating the need for more costly probabilistic analysis.

7.4 DEVICE ANALYSIS AND DESIGN

7.4.1 Beam Super-Element

Numerous designs of MEMS use beams as the main structural element, e.g. folded beam lateral micro resonators (FBLMR) [7.16], *in-situ* micro strain gauges [7.6], etc. These structures can be modeled in detail using a simulation of the detailed crystal grain microstructures (Chapter 5) or using random fields (Chapter 6). The shear scale of such a model may be impractical for routine computer implementation. Additionally, the designer is not usually interested in the detailed within-beam quantities such as stresses, displacements, etc, but rather in the global beam responses and how these affect the device behavior.

For example, the natural frequency of vibration of a FBLMR is governed by the effective stiffnesses of the folded beams and the associated uncertainties. The geometry of the beams are nominally identical and with their close proximity within the die, it is reasonable to expect that their stiffnesses will have identical probability distributions.

The random field approach provides an efficient means for a probabilistic study of micro-electro-mechanical systems consisting of multicrystalline micro-beam elements with arbitrary geometry and boundary conditions. By developing beam super-elements, the response of devices with complex structural configurations can be readily estimated using existing finite-element models. For these cases, the response of interest is the device global response, e.g. the natural frequency of vibration of a resonator, and not the within-beam variations of displacement, rotations, etc.

For the typical sizes of these beams, the spatial randomness in the material micro-structure is dictated by the fabrication process conditions such as

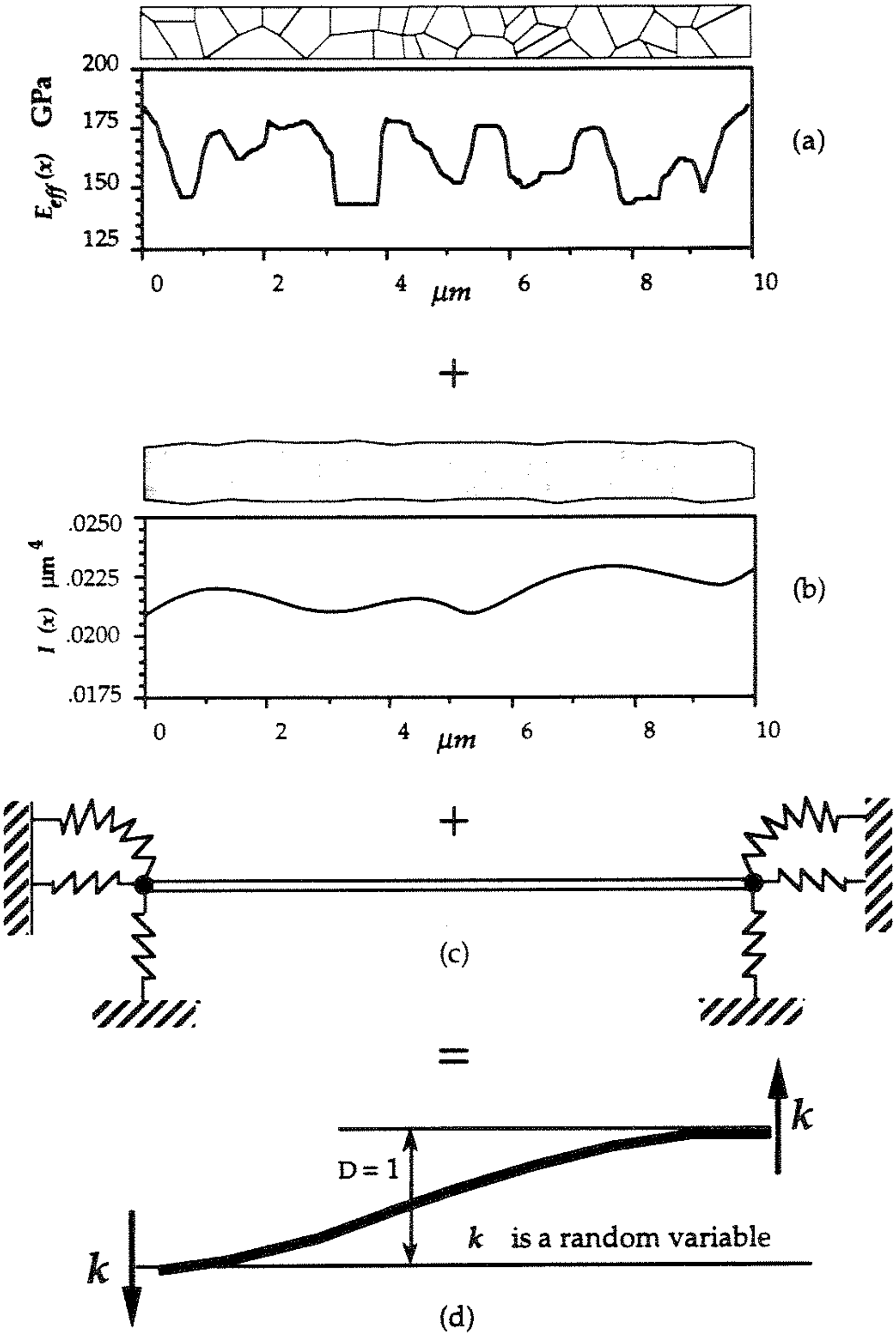

Fig. 7.7 Random Beam Lateral Stiffness

deposition temperature, gas flow rate, anneal time and dopant concentration. These process conditions can produce random grain sizes and orientations of the type shown in Fig. 7.7 (a). This results in uncertainties in the effective axial Young's modulus as shown in Fig. 7.7 (a). Additionally, there are dimensional uncertainties, such as variations in beam length, width—Fig. 7.7 (b)—and thickness that can contribute to the uncertain response of the micro beam in various MEMS applications, e.g. folded-beam resonators and passive micro strain gauges [7.6]. Boundary condition uncertainties may also be present and need to be modelled accurately for a satisfactory estimation of the effective beam stiffness uncertainty (e.g. see example problem in §6.6.2).

The lateral stiffness of micro-beams used in MEMS, e.g. folded-beam microresonators, Fig. 2.4 [7.16], are probabilistically characterized using the methodology described above, e.g. the lateral stiffness k, is characterized using its mean, μ_k, and standard deviation, σ_k using the same methodology shown in §6.3.4 and §7.3. These are then used to model the structural response of the device, for example, the natural frequency, ω: μ_ω , σ_ω as shown in the following section. The complete beam in the device of interest is therefore treated as one element—the beam super-element—with lateral stiffness k characterized using μ_k and σ_k .

7.4.2 Analysis and Design of Lateral Micro Resonators

The basic features of the folded-beam micro lateral resonator (FBMLR) have already been described in §2.3 (also see Fig. 2.4). This device can serve as both a sensor and an actuator and its versatility has been used in numerous applications of MEMS [7.13, 7.16].

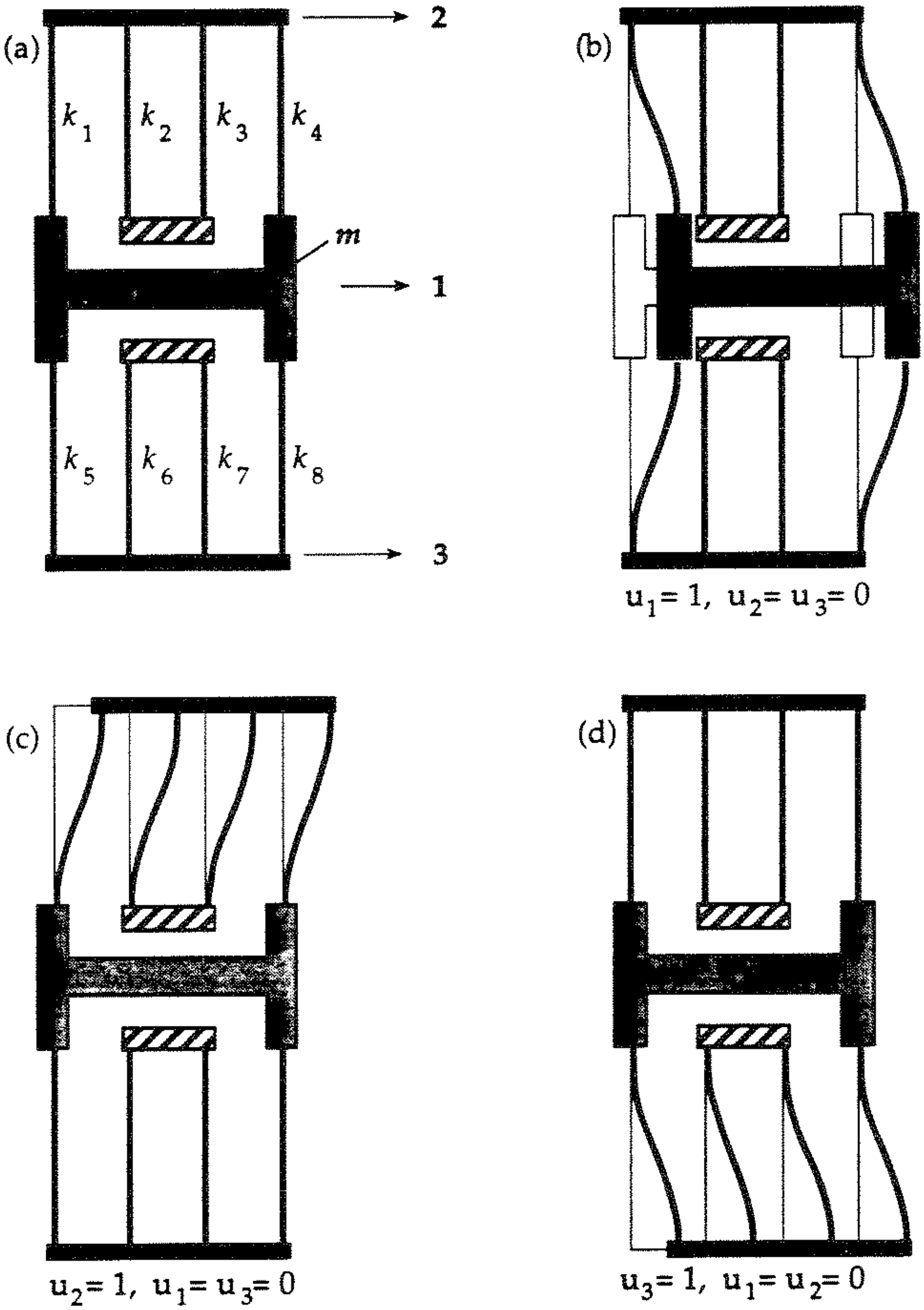

$u_1 = 1,\ u_2 = u_3 = 0$

$u_2 = 1,\ u_1 = u_3 = 0$

$u_3 = 1,\ u_1 = u_2 = 0$

Fig. 7.8 Structure, DOFs, and Deformed Configurations of the Folded-Beam Lateral Micro-Resonator

The response of this device is modelled using beam super-elements of the type discussed in §7.4.1. Fig. 7.8 (a) shows a structural model with the three degrees of freedom. The four beams, 1, 4, 5, and 8 are rigidly connected at one end to the shuttle mass and at the other end to a connecting bar (assumed to behave rigidly). Beams 2, 3, 6, and 7 are rigidly connected at one end to the connecting bar and at the other end to anchor points that are the supports for the structure. The comb-drive mechanism is designed such that the shuttle mass is only free to move in the lateral direction denoted as degree of freedom (DOF) 1 in Fig. 7.8 (a). DOFS 2 and 3 correspond to the lateral movement of the rigid beams. Figs. 7.8 (b), (c), and (d) show the deformed shape of the structure when each of the DOFs takes on the value of unity, while the others are kept equal to zero. The stiffness coefficients for the 3x3 structural stiffness matrix can be deduced from these deformed shapes.

The equations of motion for free vibrations of the FBLMR can be written in matrix form as

$$\mathbf{M}\ddot{\mathbf{u}} + \mathbf{K}\mathbf{u} = \mathbf{0} \tag{7.11}$$

where **M** and **K** are the 3x3 mass and stiffness matrices, respectively. **K** is defined in terms of k_i, $i = 1,8$, the individual beam lateral stiffnesses, as

$$\mathbf{K} = \begin{bmatrix} k_1 + k_4 + k_5 + k_8 & -k_1 - k_4 & -k_5 - k_8 \\ -k_1 - k_4 & k_1 + k_2 + k_3 + k_4 & 0 \\ -k_5 - k_8 & 0 & k_5 + k_6 + k_7 + k_8 \end{bmatrix} \tag{7.12}$$

The equivalent system represented by the three-bay shear frame with massless first floors shown in Fig. 7.9 may be more familiar to structural engineers. Ignoring axial effects, the equations of motion for the two systems are identical.

The entire comb-drive structure is part of the shuttle mass (see §2.3), therefore, the beam and connector masses are relatively negligible and can be ignored†. The resultant mass matrix **M** therefore has only one non-zero term, namely $M_{11} = m$.

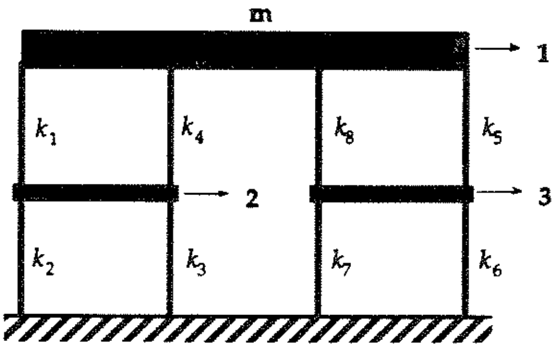

Fig. 7.9 Equivalent 3-Bay Shear Frame with Mass, m, Stiffnesses, k_i, and Degrees of Freedom 1, 2, and 3

The eigenvalue problem for free vibrations of the FBLMR is now solved:

$$\det\left(\mathbf{K} - \omega^2\mathbf{M}\right) = 0 \tag{7.13}$$

with solutions, ω_i, i = 1,2,3, as the modal natural frequencies. The square of the natural frequency in the fundamental mode is given by the smallest of the narural frequencies, $\omega_{fund} = \omega_1$, where the eigenvalue solution is given by

$$\begin{aligned}\omega_{fund}^2 = (&k_4k_7k_8 + k_3k_7k_8 + k_2k_7k_8 + k_1k_7k_8 + k_4k_6k_8 + k_3k_6k_8 + k_2k_6k_8 + k_1k_6k_8 + \\ &k_3k_4k_8 + k_2k_4k_8 + k_1k_3k_8 + k_1k_2k_8 + k_4k_5k_7 + k_3k_5k_7 + k_2k_5k_7 + k_1k_5k_7 + \\ &k_3k_4k_7 + k_2k_4k_7 + k_1k_3k_7 + k_1k_2k_7 + k_4k_5k_6 + k_3k_5k_6 + k_2k_5k_6 + k_1k_5k_7 + \\ &k_3k_4k_6 + k_2k_4k_6 + k_1k_3k_6 + k_1k_2k_6 + k_3k_4k_5 + k_2k_4k_5 + k_1k_3k_5 + k_1k_2k_5) \\ &\div \left[m\left(k_1 + k_2 + k_3 + k_4\right)\left(k_5 + k_6 + k_7 + k_8\right)\right]\end{aligned} \tag{7.14}$$

For k_i = deterministic constant, i = 1, 8, the fundamental mode shape is $[1, 0.5, 0.5]^T$ which is shown schematically in Fig. 7.10. This is equivalent to the mode shape of the mean system.

---

† Pratt et al. [10] have incorporated the masses of the stiffener and the beams for a more precise derivation of the mass matrix **M**. This adjustment, however, will only alter the mean value of the natural frequency, ω, and does not have a significant impact on the uncertainties in ω.

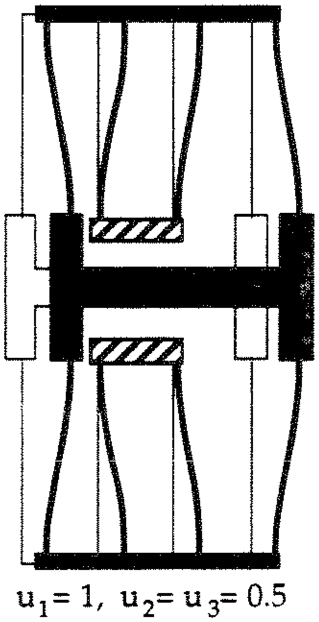

Fig. 7.10 Fundamental Mode Shape for mean FBLMR

For identically distributed, independent random variables k_i, with mean μ_k, the first order approximate mean value for the natural frequency of the FBLMR, μ_ω, is derived from Eq. 7.14 by substituting μ_k for k_i:

$$\mu_\omega = \sqrt{\frac{2\mu_k}{m}} \tag{7.15}$$

Two different resonator designs are now considered that have the same mean value for the natural frequency of free vibrations. These are shown schematically in Fig. 7.11 (a) and (b).

The single-degree-of-freedom (SDOF) systems' stiffnesses are established in a similar manner to the above, and the fundamental natural frequencies are derived to be:

$$\omega_{fund}^2 = \frac{k_1 + k_2 + k_3 + k_4}{2m} \tag{7.16}$$

$$\omega_{fund}^2 = \frac{k_1 + k_2}{m} \tag{7.17}$$

Both systems have the mean natural frequency as in Eq. 7.15.

Note that the masses of the two designs have been adjusted such that the mean value of the natural frequency is the same for all three designs. Using this arrangement, the effect of resonant structure design on μ_ω & σ_ω can be assessed.

Structural reliability concepts [7.9] are used to efficiently determine the response statistics. By defining the limit-state function as

$$g = \omega_{fund} - \omega_o \tag{7.18}$$

the cumulative distribution function of ω_{fund} is computed as

$$F_{\omega_{fund}}(\omega_0) = \int_{g<0} f_X(x)dx \tag{7.19}$$

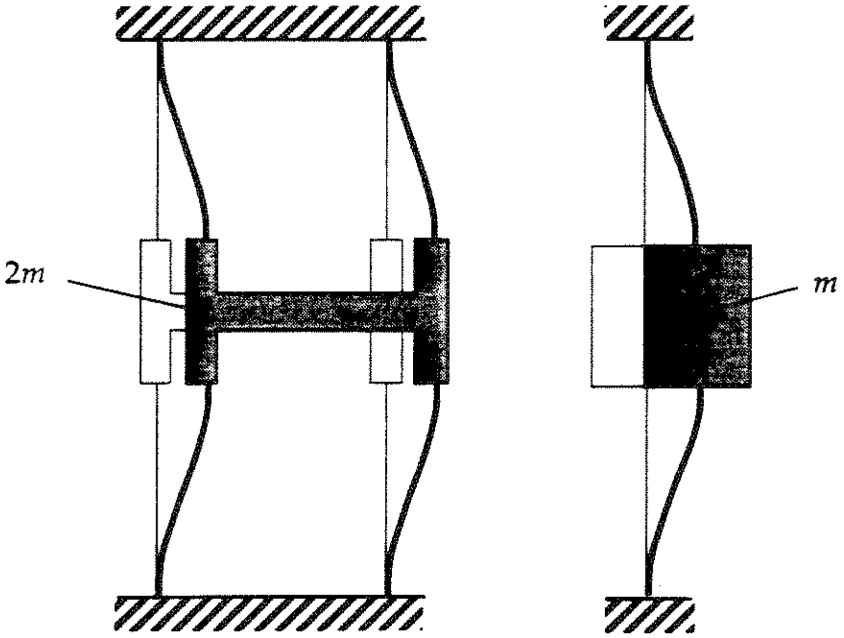

Fig. 7.11 (a) Four-Beam and (b) Two-Beam Fixed-Fixed Lateral Resonators

where x denotes the set of random variables with joint PDF $f_X(x)$. By substituting the appropriate expression for ω_{fund} in Eq. 7.18, i.e. from Eqs. 7.14, 7.16, or 7.17, each limit-state function is defined. The integral is then computed using the first-order reliability method [7.9]. The PDF of ω_{fund} is computed as the sensitivity of the above integral with respect to ω_o, i.e.

$$f_{\omega_{fund}}(\omega_o) = \frac{\partial F_{\omega_{fund}}(\omega_o)}{\partial \omega_{fund}} \tag{7.20}$$

The spread in the results using a coefficient of variation (C.O.V.) of 1% for *k* is shown in Fig. 7.12 for the resonators in Fig. 7.8, and Fig. 7.11. Clearly, using more beams reduces the uncertainty in the resonant frequency. Figs. 7.13 and 7.14 show the variations in resonant frequency when using beams of different lengths. The structure studied is from Fig. 2.4, i.e. the folded-beam microresonator. The absolute value of the spread in the results reduces with increased length, however, the effect is the opposite in relative terms (i.e. the C.O.V.s).

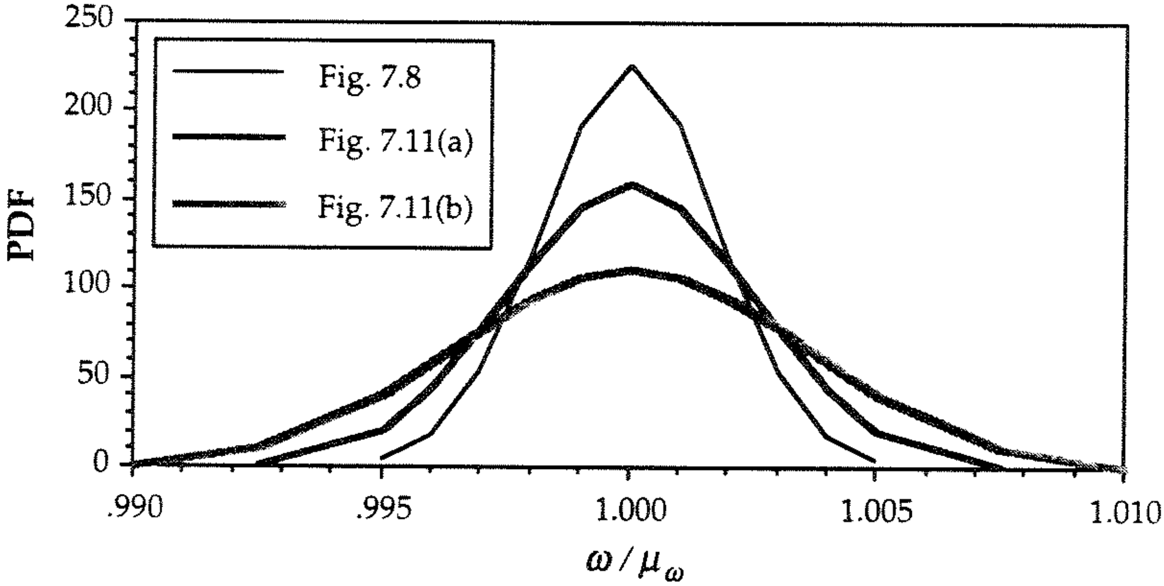

Fig. 7.12 Spreads in the Random Natural Frequencies About the Mean Value

As there are more crystals to average over, beams with smaller grain sizes have lower response standard deviations. Similarly, when a device is employing more beams, and/or longer beams there will be a reduction in the standard deviation of response. This can be used advantageously in designs of lateral micro-resonators when the grain size cannot be made smaller due to other constraints. For a fixed grain size, FBLMRs with longer beams and with appropriate adjustments in the shuttle mass and beam widths (such that the desired mean value for the natural frequency is maintained) will have reduced uncertainty in their natural frequencies.

The uncertainties in the micro-beam stiffnesses reduce with increased length, L, thus resulting in reduced standard deviation for the resonant frequency (Fig. 7.13). Note, however, that the C.O.V.s tend to increase (Fig. 7.14).

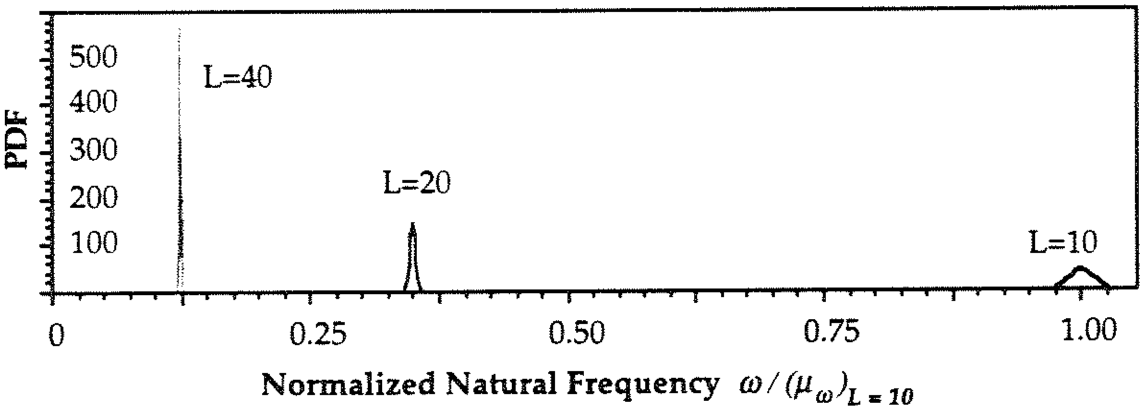

Fig. 7.13 Normalized Natural Frequency PDFs—I

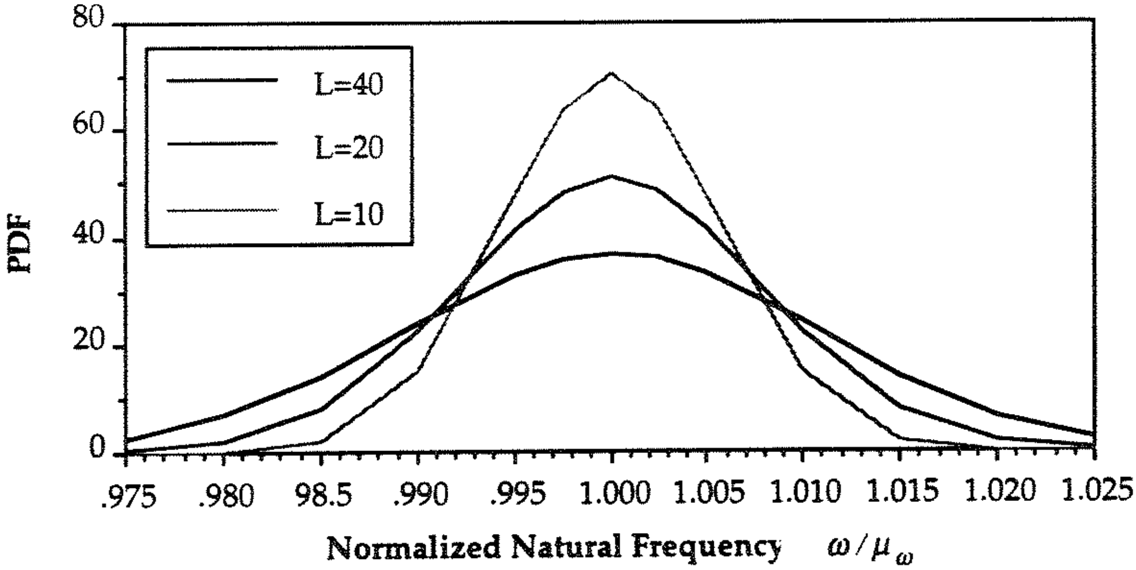

Fig. 7.14 Normalized Natural Frequency PDFs—II

7.4.3 Probabilistic vs. Deterministic Analysis

Depending on the level of uncertainty in the response of interest, probabilistic analysis may be necessary for a MEMS device. It should be clear from the previous sections, however, that problems where a RVE does not exist and where the component responses, e.g. beam lateral stiffnesses, are unacceptably uncertain can still be treated as deterministic if the device design has resulted in an acceptably low C.O.V. for the response of interest. Indeed, many of the current designs of MEMS devices result in significant reductions in the uncertainty of the device response as compared to the structural component response. The FBMLR with eight relatively long beams is a very good example of such a design. The design features for this device have been dictated by requirements such as stability, levitation control, and stress relief features (e.g. the folded beam design allows free outward extension of the beams during annealing). The resulting design satisfies these requirements and fortuitously reduces the uncertainty in the device response.

For MEMS devices, the required level of precision in performance is often much higher than, say, civil engineering structural applications. Therefore, for adequate performance of many MEMS devices, although C.O.V.s of approximately 1% considered in previous sections may appear to be very small, they may still have to be accounted for or reduced. An example device where such precision is of paramount importance is the microelectromechanical filter where a pair of FBLMRs are used either in series or in parallel [7.8]. The device performance relies on a precise small *difference* between the natural frequencies of the two resonators.

By recognizing the parameters contributing to the reduction of the device response uncertainty, the MEMS designer can directly address the issue of device response uncertainty. For many cases, devices can be designed that will have an essentially deterministic response in spite of uncertain component characteristics.

7.5 ANALYSIS OF A MICRO STRAIN GAUGE

7.5.1 Device Description

Fig. 7.15 shows the conceptual diagram of a passive micro strain gauge [7.6]. The response of the slope beam is the subject of the probabilistic analysis here. The wafer is first deposited with a 2.5 μm thick layer of phosphorus-doped glass (PSG) and the anchors are opened to the substrate (mask #1). The

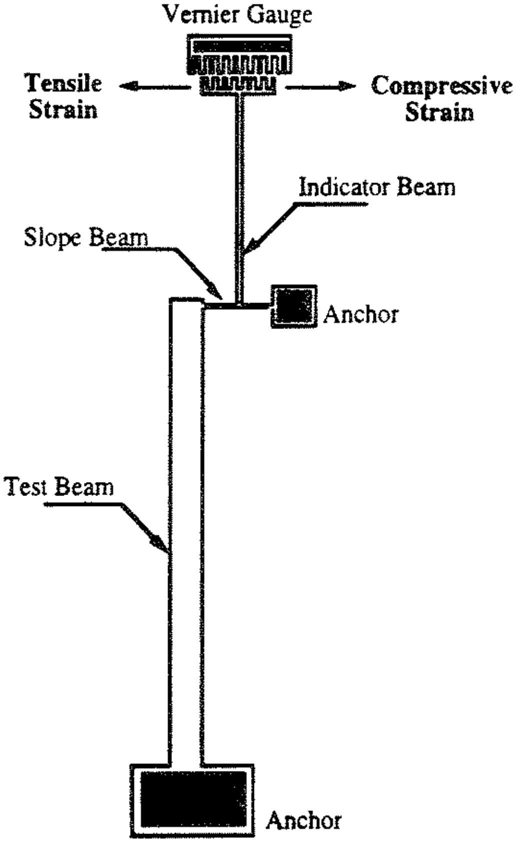

Fig. 7.15 Schematic Diagram of a Passive *in-situ* Micro Strain Gauge

structure layer, polysilicon with thickness of 2 μm, is then deposited at 605 °C and is followed by a 0.5 μm thick PSG deposition. A high temperature (900 °C, two hours) drive-in/annealing step is then executed to dope the structure with phosphorus. The wafer is then patterned and etched to form the strain gauge (mask #2). The residual strain can be calculated by observing the displacement of the vernier gauge after removing the PSG layers in 5:1 BHF (buffered hydro-fluoric acid).

7.5.2 Structural Model

The structural model for the *in-situ* micro strain gauge assumes the test beam to be infinitely rigid relative to the slope beam. With this assumption, the slope beam can be modeled with both ends fixed. The rotation at mid-span is estimated when one end of the slope beam is subjected to a lateral deflection (equivalent to the extension or contraction of the test beam). This is shown schematically in Fig. 7.16.

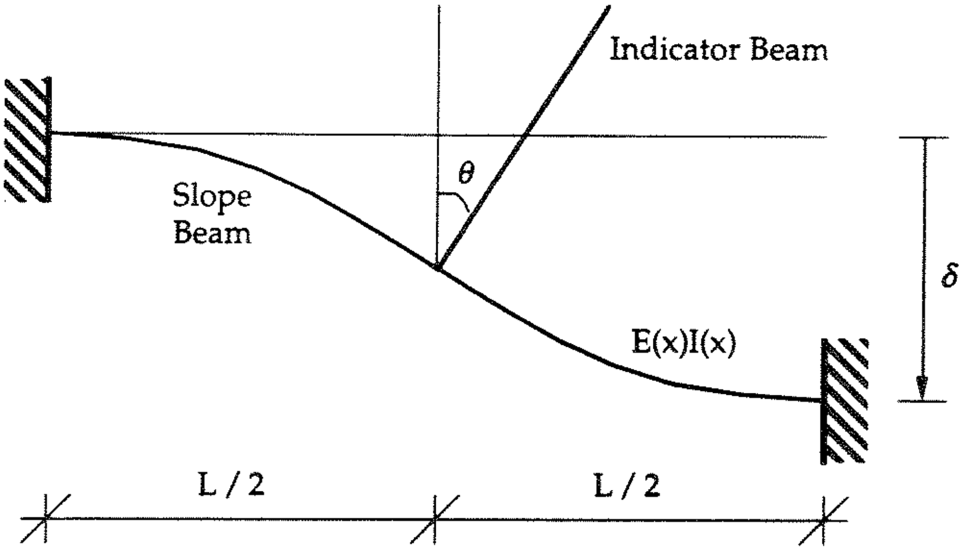

Fig. 7.16 Slope Beam Structural Model

Assuming Euler-Bernoulli beam theory to be valid, the slope beam mid-span rotation, θ, is expressed as:

$$\theta = \frac{\int_0^{L/2}\left[\frac{L}{2}\left(1-\frac{2}{L}x\right)/E(x)I(x)\right]}{\int_0^{L/2}\left[\frac{L^2}{4}\left(1-\frac{2}{L}x\right)^2/E(x)I(x)\right]}\frac{\delta}{2} \qquad (7.21)$$

If $E(x)$ and $I(x)$ are constant along the slope beam, the mid-span rotation would be independent of the lateral stiffness of the slope beam. Due to microstructural uncertainties and unevenness of etch, however, there are small variations in both $E(x)$ and $I(x)$ which result in variations in the mid-span rotation.

7.5.3 Experimental Results

Tensile strain is found in the above process and the histogram of the vernier gauge measurements for 54 different structures is shown in Fig. 7.17, indicating a coefficient of variation (C.O.V.) of approximately 10% [7.6]. Each individual strain gauge, however, was located on a different die of the same wafer. Variations in strain are to be expected over the area of a wafer.

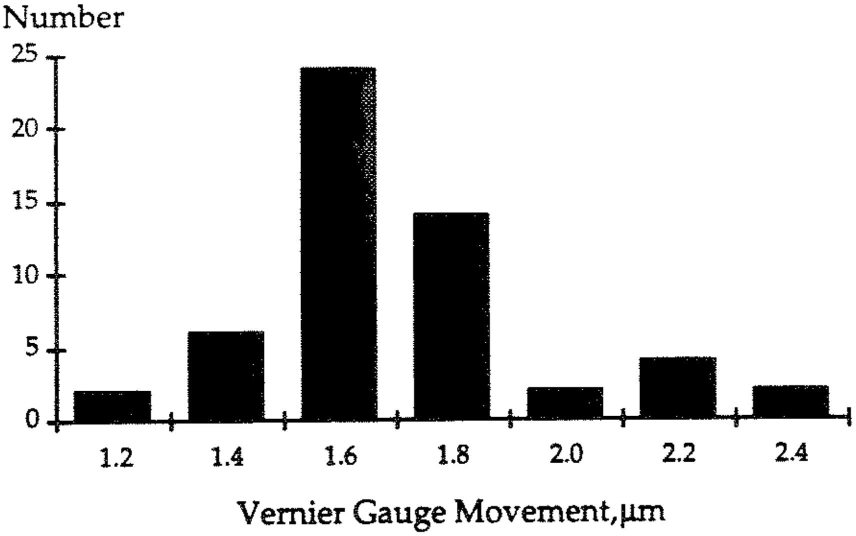

Fig. 7.17 Histogram of the Vernier Gauge Readings for 54 Cases

7.5.4 Theoretical Predictions

The measured response of the strain gauge is the slope beam rotation at mid-span, which is proportional to the vernier gauge readings. Table 7.3 summarizes the coefficients of variation (C.O.V.) of the response for various slope beam lengths, L_s, and for various grain sizes which result in Young's modulus variations. Three different slope beam lengths: 20 μm, 40 μm, and 80 μm, and three grain sizes: $\lambda = 1$, $\lambda = 3$, $\lambda = 9$ (λ being the mean number of grains per unit area) are simulated. It is found that longer beams and larger grain sizes give higher C.O.V.s for the response. Table 7.4 summarizes simulation results for different beam width variations. Two cases—3% and 6% C.O.V. for *w*—corresponding to different levels of uncertainty, are simulated, 6% approximating the real test structure. The larger width variations result in higher C.O.V.s for the response.

Table 7.3 Coefficient of Variation of Slope Beam Rotation Due to Young's Modulus Variations

	$L_S = 20$	$L_S = 40$	$L_S = 80$
$\lambda = 1$	1.14%	1.58%	2.01%
$\lambda = 3$	0.91%	1.32%	1.66%
$\lambda = 9$	0.66%	1.04%	1.34%

Table 7.4 Coefficient of Variation of Slope Beam Rotation Due to Beam Width Uncertainties

	$L_S = 20$	$L_S = 40$	$L_S = 80$
C.O.V. of *w* = 3%	0.80%	1.12%	1.54%
C.O.V. of *w* = 6%	1.56%	2.21%	3.12%

The probabilistic analysis predicts a maximum C.O.V. of approximately 1.14% for the response due to the random grain structure and a C.O.V. of approximately 1.56% due to the beam width variations. Assuming these two events to be independent, the total C.O.V. would be 1.93%. This would correspond to a set of nominally identical structures, measuring the same residual strain. This estimate does not compare well with the experimental results referred to above (C.O.V. of 10%). Those results, however, are based on residual strain measurements made throughout one wafer and, therefore, may not be measuring identical strains. Measuring residual strains within one die using up to 100 nominally identical strain gauges should show much smaller C.O.V.s. Experimental measurement errors, angle variations of the beam cross section, variations in the film thickness, and boundary condition uncertainties could be additional sources of uncertainty that are not accounted for in this example. These effects, however, should be small compared to those that have already been modeled.

Additional experimental results for four sets of 100 nominally identical strain gauges on a single die have also been generated by Lin [7.20]. While not refuting the theoretical predictions noted above, the gauge readings lacked the necessary resolution to allow the calculation of the small variation in the slope beam mid-span rotation. A redesign of the vernier scale would be necessary to capture a more precice set of readings.

7.6 SUMMARY

Four classifications are defined for polysilicon MEMS. Classes I, II and III are homogenizable since a representative volume element (RVE) exists. Class I is composed of untextured material and is therefore isotropic. Class II is textured, but with a plane of symmetry coincident with the structural geometry of the device and is therefore transversely isotropic in that plane.

Class III is textured, but without a plane of symmetry coincident with structural geometry of the device, and is therefore anisotropic. Class IV is not homogenizable since an RVE does not exist. Examples are presented for Class I, II and IV problems. The Chapter concentrates mainly on Class IV polysilicon MEMS example devices and structural components since existing models and analysis approaches are most inadequate for this Class.

Section §7.2 highlights the importance of choosing material models appropriate for the dimensions, excitations, and controlling responses of MEMS devices. For homogenizable cases (Classes I, II, and III), the first-order Voigt and Reuss bounds are adequate in describing the elastic response of MEMS devices composed of polysilicon. For cases where a RVE does not exist (Class IV), an uncertainty in the material properties is introduced due to the geometric and textural variations of the material microstructure. This translates into elastic moduli best described by random fields, e.g. Young's modulus, $E(x)$ (§6.3).

For "multicrystalline" beams (Class IV), uncertainty in $E(x)$ leads to uncertainty in the lateral stiffness of the beam, k, which then translates into uncertainty in the response of the device (composed of one or more beams). Although uncertainties at the component level may be too large, the performance at the device level is usually the gauge as to whether it is necessary to undertake probabilistic analysis.

Examples showed how design changes can result in lower Class IV device response uncertainty. The models developed here can be used to estimate the response of different designs, thus avoiding costly trial and error in actual fabrication and testing of prototype designs.

A shear beam super-element is derived and employed in the analysis of an example device—the folded-beam lateral micro-resonator (FBLMR). This model captures the global behavior of multicrystalline beams. The element can be conveniently incorporated into existing MEMS analysis tools, either through direct definition of the element, or by substituting an equivalent effective Young's modulus (as a random variable) for a standard shear beam element.

An example was presented to make a practical comparison. A passive in-situ micro strain gauge was modelled and the response uncertainties were predicted. The experimental results, although not disproving the theoretical predictions, could not verify the exact uncertainties due to resolution problems with the device design.

The models and approaches presented here are a first attempt to incorporate uncertainties in the modelling and response prediction of MEMS. Improvements are possible at all levels—for the material microstucture models, structural element models, or device models—and recommendations for future work in this area are discussed in §8.2.

CHAPTER 7 REFERENCES

[7.1] Friedman, Z. and Kosmatka, J.B. (1992). "Exact Stiffness Matrix of a Nonuniform Beam—I. Extension, Torsion, and Bending of a Bernoulli-Euler Beam," *Computers and Structures*, Vol. 42, No. 5, pp. 671–682.

[7.2] Jacobsen, S.C., M.G. Mladejovsky, C.C. Davis, J.E. Wood, and others, "Advanced Intelligent Mechanical Sensors (AIMS) *TRANSDUCERS '91. 1991 International Conference on Solid-State Sensors and Actuators, San Francisco, CA, USA, 24-27 June 1991*, New York, NY, USA: IEEE, pp. 969–973, 1991.

[7.3] Koskinen, J., J.E. Steinwall, R. Soave, and H.H. Johnson, "Microtensile Testing of Free-Standing Polysilicon Fibers of Various Grain Sizes," *Journal of Micromechanics and Microengineering*, Vol. 3, No.1, pp. 13–17, 1993.

[7.4] Krulevitch, P., G.C. Johnson, and R.T. Howe, "Stress and Microstructure in Phosphorus Doped Polycrystalline Silicon," *Smart Materials Fabrication and Materials for Micro-Electro-Mechanical Systems*, Edited by: Jardine, A.P., G.C. Johnson, A. Crowson, and M. Allen, Pittsburgh, PA, USA: Mater. Res. Soc., pp. 79–84, 1992.

[7.5] Li, C.-C. and Der Kiureghian, A., "Optimal Discretization of Random Fields," *Journal of Engineering Mechanics, ASCE*, Vol. 119, No. 6, pp. 1136–1154, 1993.

[7.6] Lin, L.-L., R.T. Howe, and A.P. Pisano, "A Passive, In Situ Micro Strain Gauge," Proceedings IEEE. Micro Electro Mechanical Systems, Fort Lauderdale, FL, USA, 7-10 Feb., pp. 201–206, 1993.

[7.7] L. Lin, R. T. Howe and A. P. Pisano, "A Passive, *in situ* Micro Strain Gauge", *IEEE Micro Electro Mechanical Systems (MEMS93)*, pp. 200-206, Ft. Lauderdale, Florida, Feb. 1993.

[7.8] Lin, L., C.T.-C. Nguyen, R.T. Howe, and A.P. Pisano, "Microelectromechanical Filters for Signal Processing," *Proceedings, IEEE Micro Electro Mechanical Systems: An Investigation of Micro Structures, Sensors, Actuators, Machines and Robots*, Travemunde, Germany, 4-7

Feb. 1992, Edited by: Benecke, W. and H.-C. Petzold, New York, NY, USA: IEEE, p. 226–231, 1992.

[7.9] H. O. Madsen, S. Krenk, and N. C. Lind (1986). *Methods of Structural Safety*, Prentice-Hall, Englewood Cliffs, NJ.

[7.10] D. Mirfendereski and A. Der Kiureghian (1992). "Random Response of Multicrystalline Structures," *Proc. 9th Engineering Mechanics Conference, ASCE*, College Station, Texas.

[7.11] D. Mirfendereski and A. Der Kiureghian, "Reliability Analysis of Micro-Fabricated Multicrystalline Beams," *International Conference on Structural Safety and Reliability (ICOSSAR'93)*, Austria, Aug. 1993.

[7.12] Pampuch, R., *Constitution and Properties of Ceramic Materials*, Materials Science Monographs, 58, Elsevier Science Pub. Co., Inc., New York, 1991.

[7.13] Pratt, R.I., G.C. Johnson, R.T. Howe, and J.C. Chang, "Micromechanical Structures for Thin Film Characterization," *TRANSDUCERS '91. 1991 International Conference on Solid-State Sensors and Actuators, San Francisco, CA, USA, 24-27 June 1991*, New York, NY, USA: IEEE, pp. 205–208, 1991.

[7.14] Romano, F. and Zingone, G., "Deflections of Beams with Varying Rectangular Cross Section," *Journal of Engineering Mechanics*, Vol. 118, No. 10, pp. 2128–2134, 1992.

[7.15] Shuwen Guo, Daowen Zou, and Weiyuan Wang, "Theoretical Calculation for the Young's Modulus of Poly-Si and a-Si Films," *Smart Materials Fabrication and Materials for Micro-Electro-Mechanical Systems*, Edited by: Jardine, A.P., G.C. Johnson, A. Crowson, and M. Allen, Pittsburgh, PA, USA: Mater. Res. Soc., pp. 233–238, 1992.

[7.16] W. C.-K. Tang (1990). *Electrostatic Comb Drive for Resonant and Actuator Applications*, Dissertation, University of California at Berkeley.

[7.17] Walker, J.A., K.J. Gabriel, and M. Mehregany, "Mechanical Integrity of Polysilicon Films Exposed to Hydrofluoric Acid Solutions," *Journal of Electronic Materials*, Vol. 20, No.9, pp. 665–670, 1991.

[7.18] Zienkiewicz, O. C. and Taylor, R. L., *The Finite Element Method, Vol. 1*, McGraw-Hill, London, U.K., 1989.

[7.19] Qingyuan Meng, M. Mehregany, and R.L. Mullen, "Theoretical Modeling of Microfabricated Beams with Elastically Restrained Supports," *Journal of Microelectromechanical Systems*, Vol. 2, No. 3, pp. 128–37, 1993.

[7.20] Lin, Liwei, Personal Communication, April, 1993.

Chapter 8

CONCLUSIONS & RECOMMENDATIONS

8.1 CONCLUSIONS

The mechanical response of Micro-Electro-Mechanical Systems (MEMS) is governed by the properties of the constituent materials. For IC-process based micromachined MEMS, the process conditions and device dimensions often result in structural components for which assumptions of material isotropy or homogeneity may be invalid. These effects pose challenges for analyzing and designing such devices, especially as MEMS technology pushes the frontiers of miniaturization.

Homogenization techniques are shown to be readily applicable to polycrystalline silicon—the chief constituent material in IC-process based MEMS. For many applications, the inhomogeneities of a polycrystalline aggregate can be homogenized, or averaged out, when the scale of the microstructure is far smaller than the structural dimensions of MEMS devices. For such cases, a representative volume element (RVE) is said to exist, a basic requirement for homogenization. The low degree of anisotropy of silicon is shown to result in relatively narrow first order bounds on the elastic properties of polycrystalline samples. The first-order Voigt and Reuss bounds are relatively easy to compute as they only require first-order statistical information regarding the material microstructure, i.e. the orientation distribution function (ODF). The ODF is easily obtained using well-established laboratory techniques. The deterministic analysis employing homogenized material properties is a generally more consistent approach than assuming transverse isotropy for a particular microstructure and measuring the "Young's modulus" by experimental techniques. The texture measurements will first confirm whether transverse isotropy can be assumed, and the homogenization would allow the prediction of out of plane responses.

Polycrystalline inhomogeneities, however, cannot be averaged out when a structural member consists of a relatively small number of grains, i.e. when a RVE does not exist. Length scales associated with MEMS and the process conditions which may require high degrees of annealing result in relatively large grains that are of the same order of magnitude as the smallest dimensions of the structural components. This results in the material behaving as an inhomogeneous continuum. Moreover, the material's microstructural characteristics, e.g shapes, sizes, orientations, or arrangements of the crystal grains, are generally uncertain. This uncertian inhomogeneity translates into a material with uncertain mechanical properties. In such cases, for example, the concept of a deterministic "Young's Modulus" is no longer applicable.

When a RVE does not exist, structural responses may lie outside the range predicted by the Voigt and Reuss bounds. This is normally the case for large grained samples. An example problem has been presented which demonstrates the probabilistic nature of the structural response (§7.2.2). The tip deflection of an end-loaded cantilever polysilicon beam was analyzed for a beam width of 1 μm and an average grain area of 0.33 μm^2. For this configuration, the structural response had a C.O.V. of approximately 3%.

With this level of uncertainty, a large proportion of outcomes would fall outside the range predicted by the Voigt and Reuss bounds on the effective Young's modulus.

A finite element simulation model has been developed herein which captures the geometric and orientational uncertainties of the material and which predicts the mean and standard deviation of response for structural members composed of such materials. The model methodology is applicable to any geometric arrangement of crystal grains which can be approximated using straight-edged polygons. A mathematical construct—the Voronoï diagram—is used in this dissertation as an analytically-derived substitute for an observed dataset of the microstructural geometry of polycrystalline silicon. Owing to the degree of detail to which the material is described, the model can predict both local and global effects.

This simulation method, however, involves computationally demanding re-meshing for each simulation and is specific to the boundary conditions and to the structural geometry of a particular problem. A large number of simulated analyses are normally required before convergence is achieved in the mean and standard deviations of the response. A computationally more efficient random field model is developed which addresses this problem. This model is developed for application to beam problems and is calibrated using the simulation model. Structural response analysis involves either several FORM/SORM analyses in order to obtain the probability distribution function of the response of interest or a more simple second-moment approach yielding the mean and standard deviation of response. Moreover, the random field model need only be defined once for a particular beam depth and grain size.

All combinations of beam length and force and displacement boundary conditions can then be analyzed using the same model.

An example problem is used to illustrate the use of the more efficient random field model.

For structural elements other than beams, a similar approach using effective properties can be established. However, a more general approach applicable to a wide variety of elements is developed herein, whereby the stochastic material stiffness matrix is modelled as a random field. The random field autocorrelation is established based on the chord-length distribution of the constituent aggregates. This random field can then be discretized for implementation with a finite element code in modelling any desired continuum structure.

For modelling MEMS devices comprised of several structural members, e.g. a lateral micro-resonator [8.9], the development of super-elements is shown to be an efficient way of determining the device response characteristics. For general devices comprising of many different structural elements, this super-element approach is found to be a practical and effective method of analysis.

The importance of appropriate material modeling in the analysis of MEMS structural components is established through the use of the developed models in several examples. Through these examples, the "hidden" problems of using inappropriate material models and the inconsistencies and misinterpretations that would otherwise ensue are highlighted.

A simplified methodology is presented whereby the level of uncertainty of a given problem is efficiently established, thus determining whether costly probabilistic analysis is necessary at all.

Finally, the material and structural component models are used to show how the MEMS designer can be aided in selecting a combination of structural dimensions and material grain sizes which minimize the uncertainty of the structural response of interest. Often, the material microstructure is predefined due to the electrical property requirements or due to the necessary annealing which reduces detrimental residual stresses. The most fruitful dimensional modifications can be gleaned from analyzing prototype designs using the models developed in this dissertation. This would significantly reduce the high cost of numerous prototype designs constructed in an ad hoc manner through which a suitable solution is finally found by trial and error.

For example, the standard deviation of the lateral stiffness of large-grained beams is shown to reduce with increased beam lengths—longer beams have more grains, resulting in more averaging of properties. However, as beam lengths are increased, the mean lateral stiffness of the beams is shown to reduce at a faster rate than their standard deviation. This results in increasing C.O.V.s for the lateral stiffness of long beams. For example, C.O.V.s of approximately 3.2%, 4.4%, and 6.1% are predicted for 1 μm wide beams of length 10, 20, and 40 μm, respectively (§7.3). These component C.O.V.s translate into a corresponding C.O.V. for the natural frequency of a FBMLR. The device C.O.V.s are generally lower than the component C.O.V.s (by approximately 1/6th), however, the device design plays an important role in determining this uncertainty: devices with more beams have reduced uncertainty, while longer beams reduce the standard deviation of response but increase the C.O.V.

The models and analysis procedures developed in this dissertation are the first to address the inherent uncertainties in the response of MEMS components and devices. The application of the models shows the extent to which the material uncertainties can affect MEMS structural response. The existence of these response uncertainties has been established, while the issue of appropriate analysis models is highlighted. Many of the concepts developed herein can be directly applied to the analysis and design of practical MEMS devices. Several of the models developed in this dissertation can be further developed and applied to a broader range of structures and enable the inclusion of additional features. These further developments together with other areas that are deemed appropriate for further research are discussed in the following section.

8.2 RECOMMENDATIONS FOR FUTURE DEVELOPMENT

8.2.1 Material Level

A necessary element for the use of the simulation model developed in Chapter 5 is a detailed geometric description of the polycrystalline structure. In this dissertation, for lack of sufficient data, the Voronoï diagram has been chosen to generate fictitious "grain" geometries that are then used in the simulations. A more realistic geometric modeling of the polycrystalline state would be to calibrate the Voronoï model to match an observed ensemble of microstructural geometries. In addition to matching the average grain size, this may entail a non-uniform scaling of the Voronoï diagram to match the shapes of the observed crystal grains. This calibration requires a large number of transmission electron micrographs (TEMs) and development of a theoretically sound methodology for studying the TEMs and performing the calibration. Such calibrations would then be made for material microstructures arising from differing process conditions. The paper by Stoyan et al. [8.8] develops some methods for performing such calibrations.

Another approach for modeling the microstructural geometric features would be to develop analytic process simulation models, similar to work underway in metallurgy [8.7]. These models generally use an analytic-numerical approach in simulating the physical processes involved—deposition, nucleation, grain growth, texture development, etc. These analytic models can be calibrated using experimental observation to produce a very efficient "active" database which will predict the detailed microstructure for any desired fabrication process. The effects of dopant concentration, process temperature and pressure, and varying anneal times can be modeled and the resulting material microstructure be known in advance. Aside from allowing an efficient and more reliable means of accessing microstructural information for the purpose of simulating uncertain geometric features, this tool would allow the prediction of different material properties and could, for example, be used in developing processes to achieve improved electrical performance, and aid in mechanical/electrical behavior prediction.

The generalized random field model (§6.6.2) can be applied to a variety of 2-and 3-D problems. The implementation of this model for the solution of MEMS problems would entail the development of suitable finite elements. The most suitable course of development would be to pose the problem in a variational setting. The variation of elastic properties introduced by the uncertain grain geometries and orientations is captured by the generalized random field model of Chpater 6. Damaged states [8.10], crystal defects, and residual stresses can be included in developing stochastic finite elements. By